UNIVERSITY OF CALIFORNIA
RIVERSIDE

Compton Recoil Electron Tracking With the TIGRE Gamma-Ray Balloon Experiment

A Dissertation submitted in partial satisfaction
of the requirements of the degree of

Doctor of Philosophy

in

Physics

by

Kaoru Kamiya

June 2011

Dissertation Committee:
Dr. Allen D. Zych, Chairperson
Dr. Gabriela Canalizo
Dr. Debardarshi D. Bhattacharya

The Dissertation of Kaoru Kamiya is approved:

_____

_____

_____

Committee Chairperson

University of California, Riverside

Acknowledgement

First and foremost, I thank my chair advisor Dr. Allen D. Zych. I am honored to be his Ph.D. student. He kindly took me under his supervision during a most difficult time, and I could not have continued with my PhD work otherwise. I appreciate his time, guidance, and patience as I formed my research skills. He was always supportive, made me at ease, never made me feel inadequate, and I owe my accomplishments to him.

I thank the TIGRE group members, Dr. Terry O'Neill, Dr. Dipen Bhattacharya, and Eric Harris for sharing their long, hard work on the telescope with me. Terry patiently and thoroughly explained TIGRE's design and circuitry and his visualization program was essential to my research. Dipen spent countless hours with me setting the correct simulation of MEGAlib and helped me understand it. Eric's program was the basis of the filtering process that I applied on the flight data and he helped me customize it for my needs. Their support and enthusiastic help were vital to my completion. Many thanks to my fellow graduate students in the group, Charity H. Trojanowski and Vincent Kong. They welcomed me into the group with open arms and generously shared their work.

I thank my committee members Dr. Gabriela Canalizo and Dr. Dipen Bhattacharya for their time and interest. Aside from my research, Dipen spent extra time reviewing my thesis and gave me numerous useful critiques. He made sure that my analysis and understanding was complete, and resolved that I write the best thesis possible.

I thank all my friends and family relatives. Though I do not have the space to thank everyone, their contributions and supports were no less meaningful to me. I thank my friends in the department: Charity, Jojit, Ken, Tim, and Peter. I could not have advanced past the first two years, nor would I have remembered how to laugh without you. Our weekly "dinners", Vegas, Superbowl, and movie nights, to name a few, kept me sane. I am privileged to have witnessed your marriage, growing families, and graduation. Your amazing performances as researchers were my inspiration. We struggled and helped each other through our classes, late night homework, and exams. I strived to keep up with your results and I can only hope I earned my place as fellow classmate.

My mother, Fong Yau Lor Kamiya, and sister, Nozomi Kamiya, gave me the same love and support they gave my father during his doctorate studies. They were very patient with my complaints and never judged me. Their positive characters during difficult times shaped my own reaction, through which I was able to maintain a relatively healthy and positive outlook. They are always excited to hear about my life, even though I must have bored them with my complaints. I thank my mother in law, Lisa Lee. Her weekly provision of home-cooked meals saved me enormous amount of time and stress. My father, John Akimoto Kamiya, is the reason I chose this field, the reason I entered this program, and my inspiration. His bedtime story of black holes ignited my love for science and astrophysics. He earned his doctorate degree whilst raising two teenage daughters and being the breadwinner of the family. His determination and self-discipline

showed me the true meaning of hard work. At the same time, he showed me good balance in life with canoeing, hiking, camping, and traveling.

Finally, I thank my loving husband Joseph T. Lee. I could not have completed my research without your programming expertise. I would not have had any platform to program with without your help. With your remote access setup, I was able to pursue more results from my research than required, and finish in a shorter time than I would have alone. Most of all, you never wavered from my side during my emotionally unstable times. Your support and faith in me carried me through. Your love and patience, especially during the final stages, were ceaseless and are so appreciated. Thank you.

ABSTRACT OF THE DISSERTATION

Compton Recoil Electron Tracking
With the TIGRE Gamma-Ray Balloon Experiment

by

Kaoru Kamiya

Doctor of Philosophy, Graduate Program in Physics
University of California, Riverside, June 2011
Dr. Allen D. Zych, Chairperson

Conventional Compton telescopes use a single converter and a calorimeter that results in azimuthal uncertainty in the imaging analysis. The University of California, Riverside's (UCR) Tracking and Imaging Gamma Ray Experiment (TIGRE) was designed to minimize the directional uncertainty of the incident photons by using the silicon converter simultaneously as a photon scatterer and an electron tracker to determine the recoil electron path. TIGRE's initial flight was conducted in June, 2007 from Ft. Sumner in New Mexico. This thesis discusses the instrument's design, calibration, flight, and data analysis for Compton events. The time interval of the flight data selected for this analysis was 18,436 seconds. The expected efficiencies of the TIGRE instrument in a balloon-borne stratospheric environment, obtained from MEGAlib, a version of the GEANT 4 high energy simulator, ranged from 0.09% to 0.87% in the (0.3 – 50) MeV energy range. However, the New Mexico flight yielded

only 6.5% of the predicted number of Compton candidates which was attributed primarily to the lower number of functional detectors available during the flight. A repeat simulation with realistic telescope conditions provided the expected number of Compton events that matched the flight results within errors.

To take advantage of the tracking feature, one of the necessary procedures is to determine the Direction of Motion (DOM) of the electron track. The Pearson Correlation was used to determine the DOM. This method was successfully tested and verified by using a ^{90}Sr calibration data-set. Using this method, the flight data had 698 downward electron tracks and 862 upward electron tracks, but this result was not successful in reconstructing the Compton events. The Compton angle, determined with the electron tracks, and the Compton angles, determined by the classic Compton formula, did not correlate. The discrepancy came from the low quality NaI calorimeters, its timing window with the silicon and the anti-coincident detectors, and an accidental inclusion of a module clear code within the flight software. The analysis work undertaken for this thesis allowed us to correct and update the telescope circuitry and software for the Australia balloon flight that was carried out in the spring of 2010 (the Australian flight results are not a part of this thesis).

Table of Contents

List of Figures

List of Tables

Chapter 1 Introduction

Gamma-rays are the most energetic form of electromagnetic radiation. Gamma-ray emissions occur in phenomena such as supernova explosions, accretion in active galactic nuclei (AGNs), pulsars, gamma-ray bursts, cosmic ray interactions with interstellar gas, and solar flares. Gamma-ray astronomy gives opportunities to study exotic objects such as black holes, neutron stars and active galaxies. Since high energy photons are mostly absorbed by the Earth's atmosphere, their detection is carried out by high altitude balloon experiments or by detectors on-board satellites.

One of the most basic interactions in this energy regime is the Compton scattering process; the scattering of high energy photons by electrons. In 1927, Dr. Arthur Holly Compton won a Nobel Prize for his work in this field, and it is one of the most common detection method used today. Traditionally, this scattering was detected using two Gamma-ray detector elements in coincidence. The first detector is a converter to initiate Compton scattering, and the second detector (calorimeter) is designed to absorb the scattered photon via photoelectric absorption. However, detectors of this design are limited in sensitivity and angular resolution.

To improve upon these limitations, the Tracking and Imaging Gamma Ray Experiment (TIGRE) was developed. In place of the liquid scintillator used for converting photons in traditional telescopes, TIGRE has a multi-layered thin silicon converter/tracker. This acts not only as the traditional converter, but also as a tracker of the recoiled electron. In this way the incident photon can be reconstructed to a higher

degree of accuracy. TIGRE is a concept for future long duration balloon flight opportunities. The prototype TIGRE consists of 16 layers of 300 micron thick double-sided silicon strip detectors. On June 2, 2007, the prototype detector was launched from Ft. Sumner, New Mexico, and it was at float for 27 hours.

Compton events were selected by looking for signature characteristics such as coincidence with the calorimeter and Si converter. The energy and direction of the incident photon are reconstructed using the Compton equations and simple vector geometry. These results were compared with Monte Carlo simulation results using MEGAlib (Zoglauer, 2006).

Chapter 2 Gamma-ray Astronomy

The Electromagnetic Spectrum is divided in the regions of radio, microwave, infrared, optical, ultraviolet, X-ray and gamma-ray, from lowest to high energy. Gamma-ray astronomy is the study of the highest energy in the electromagnetic spectrum. Gamma-rays are emitted by the most energetic phenomenon in the universe. Studies in this area give insight to some of the uncommon yet most exciting spectacles; such as AGNs and blazars, accretion disks surrounding black holes and supernovae. This chapter will discuss the physics involved in high energy process, various gamma-ray detection methods, various gamma-ray projects carried by other institutions, and finally Compton telescopes.

A. High Energy Astrophysics

Gamma-ray photons are observed by looking for effects arising from gamma-rays interacting with subatomic particles. This section will discuss several such effects involving high energy astrophysics, which includes X-ray and extreme ultraviolet region.

i. Photoelectric Effect

Photoelectric absorption dominates for energies below ~60 keV. When a photon with an energy $h\nu$ is incident upon an electron bound to an atom, it can eject the electron if the binding energy of the electron is less than $h\nu$. The remaining energy of the photon is transferred as kinetic energy of the electron. It has been found experimentally and

theoretically that 80% of ejected electrons by the photoelectric effect are in the K-shell of the atom. The absorption cross section for a photon with an energy at this 1s level is

$$\sigma_k = \frac{e^{12} m_e^{\frac{3}{2}} Z^5}{192\sqrt{2\pi^5 \varepsilon_0^6 \hbar^4 c}} \left(\frac{1}{\hbar\omega}\right)^{\frac{7}{2}} \text{ (Longair, 1992)}$$

where e is the elementary charge, m_e is the rest mass of the electron, Z is the atomic number, ε_0 is the electric constant, ħ is Plank's constant, c is the speed of light, and ħω is the energy of the photon. Looking at the dependence on Z^5 and $\omega^{-7/2}$, it can be seen that for high energies, a material with high density and atomic number is necessary to make a significant contribution to the photoelectric effect.

ii. Compton Effect

In 1923, Arthur Holly Compton observed that an increase of the wavelength occurred with the incident X-ray radiation when it was scattered from an electron. This was the final convincing proof of the particle nature of light according to Einstein's theory. The phenomenon occurs when a photon with energy comparable to the rest mass energy of an electron ($E_0 \sim m_e c^2$) transfers some of its energy and momentum to a stationary electron when it collides with it. The transferred energy gives the electron enough momentum to recoil at an angle, and the incident photon is scattered to another direction. As a result, the scattered photon has less energy and a longer wavelength compared with the incident photon (Longair, 1992). The process can be described in a simple kinematic sketch in Figure 1.

The momenta of the photons and the recoiled electron are described as

$$\overrightarrow{p_0} = \overrightarrow{p_e} + \overrightarrow{p_{ph}}$$

where $\overrightarrow{p_0}$ is the momentum of the incident photon, $\overrightarrow{p_e}$ is the momentum of the recoiled electron, and $\overrightarrow{p_{ph}}$ is the momentum of the scattered photon. Their x components are described as follows

$$p_{phx} = p_{ph}\cos\theta$$
$$p_{ex} = p_e\cos\phi$$

$$p_{0x} = p_{phx} + p_{ex} = p_{ph}\cos\theta + p_e\cos\phi$$

Equation 1

Their y components are as follows

$$p_{phy} = p_{ph}\sin\theta$$
$$p_{ey} = -p_e\sin\phi$$
$$p_{0y} = p_{phy} + p_{ey} = p_{ph}\sin\theta - p_e\sin\phi = 0$$

Therefore,

$$p_{ph}\sin\theta = p_e\sin\phi$$

Equation 2

Squaring and combining Equation 1 and Equation 2,

$$\begin{bmatrix} p_e^2\cos^2\phi = \left(p_{0x} - p_{ph}\cos\theta\right)^2 \\ p_e^2\sin^2\phi = p_{ph}^2\sin^2\theta \end{bmatrix}$$
$$p_e^2\left(\cos^2\phi + \sin^2\phi\right) = p_{0x}^2 - 2p_{0x}p_{ph}\cos\theta + p_{ph}^2\left(\cos^2\theta + \sin^2\theta\right)$$

$$p_e^2 = p_{0x}^2 - 2p_{0x}p_{ph}\cos\theta + p_{ph}^2$$

Equation 3

Also conserving the energies before and after the collision will be as follows

$$E_0 + m_e c^2 = E' + \left(K + m_e c^2\right)$$
$$E_0 - E' = K$$

Equation 4

where E_0 is the energy of the incident photon, E' is the energy of the scattered photon and K is the kinetic energy of the recoiled electron. Using the relativistic energy $E^2 = c^2 p^2 + \left(mc^2\right)^2$, for photons, $E = cp$, and Equation 4 becomes

$$c\left(p_0 - p_{ph}\right) = K$$

Equation 5

Applying the relativistic energy for the recoiled electron,

$$E_e^2 = \left(K + m_e c^2\right)^2 = c^2 p_e^2 + \left(m_e c^2\right)^2$$

$$K^2 + 2Km_e c^2 = c^2 p_e^2$$

Equation 6

Combining Equation 6 with Equation 3 and Equation 5

$$\left(p_0 - p_{ph}\right)^2 + 2\left(p_0 - p_{ph}\right)m_e c = p_0^2 - 2p_0 p_{ph}\cos\theta + p_{ph}^2$$
$$\left(p_0 - p_{ph}\right)^2 + 2\left(p_0 - p_{ph}\right)m_e c = \left(p_0 - p_{ph}\right)^2 + 2p_0 p_{ph} - 2p_0 p_{ph}\cos\theta$$
$$2\left(p_0 - p_{ph}\right)m_e c = 2p_0 p_{ph}\left(1 - \cos\theta\right)$$

$$\frac{1}{p_{ph}} - \frac{1}{p_0} = \frac{1}{m_e c}\left(1 - \cos\theta\right)$$

Equation 7

Since $p = \frac{E}{c}$, Equation 7 leads to the well-known Compton formula,

$$\frac{1}{E'} - \frac{1}{E_0} = \frac{1}{m_e c^2}\left(1 - \cos\theta\right)$$

Equation 8

From Equation 8, the energy of the scattered photon can be written as

$$E' = \frac{m_e c^2}{1 - \cos\theta + m_e c^2 / E_0}$$

Equation 9

And from $E = h\nu$ the ratio of the photon frequencies are

$$\frac{\nu'}{\nu_0} = \frac{1}{1 + \frac{E_0}{m_e c^2}\left(1 - \cos\theta\right)}$$

Equation 10

From Equation 4 and Equation 9, the kinetic energy of the recoiled electron is

$$K = E_0 - \frac{m_e c^2}{1 - \cos\theta + m_e c^2 / E_0} = E_0 \frac{\frac{E_0}{m_e c^2}\left(1 - \cos\theta\right)}{1 + \frac{E_0}{m_e c^2}\left(1 - \cos\theta\right)}$$

Equation 11

From Equation 9 and Equation 11, using the maximum value of $\theta = \pi$, the minimum scattered photon energy and the maximum electron kinetic energy can be found.

The minimum energy for the scattered photon is

$$E'_{\min} = \frac{m_e c^2}{2 + m_e c^2 / E_0}$$

which corresponds to the maximum kinetic energy of the electron

$$K_{\max} = \frac{2E_0}{2 + m_e c^2 / E_0}$$

where much of the incident energy is transferred to the electron. Rearranging Equation 11 for E_0 and solving the quadratic equation, the energy of the incident photon corresponding to this is

$$E_0 = \frac{1}{2} K_{\max} \left(1 + \sqrt{1 + \frac{2 m_e c^2}{K_{\max}}} \right)$$

The maximum scattered photon energy and the minimum recoiled electron energy are when the incident gamma-ray is forward scattered as $\theta = 0$ and no energy is transferred to the electron. Then,

$$E'_{\max} = E_0 \text{ and } K_{\min} = 0$$

For incident photons with large energies ($E_0 \gg m_e c^2$), the minimum energy of the scattered photon will reach $\frac{m_e c^2}{2}$ = 0.25 MeV when the incident photon is backscattered, and will be equal to $m_e c^2$ = 0.51 MeV when $\theta = \frac{\pi}{2}$, independent of the energy of the incident photon.

Combining Equation 1, Equation 2 and Equation 10, the relationship between the scattered photon angle and the recoiled electron angle is

$$\cot \phi = \frac{p_0 - p_{ph} \cos \theta}{p_{ph} \sin \theta} = \frac{\nu_0 / \nu' - \cos \theta}{\sin \theta} = \left(1 + \frac{E_0}{m_e c^2} \right) \tan \frac{\theta}{2} \text{ (Evans, 1955)}$$

Equation 12

In 1929, Oskar Klein and Yoshino Nishina derived the Klein-Nishina formula; the cross section for unpolarized radiation upon an unbound electron.

$$\left(\frac{d\sigma}{d\Omega}\right)_{KN} = \frac{r_e^2}{2}\left(\frac{\nu'}{\nu_0}\right)^2\left(\frac{\nu_0}{\nu'} + \frac{\nu'}{\nu_0} - \sin^2\theta\right)$$ (Zoglauer, 2006)

Figure 2 shows a plot of this formula. Each curve shows the distribution of the scattering angle from different energy of the incident photon. As the incident photon energy increases, the scattering angle becomes more limited to the forward direction. Photons with higher incident energies have higher probabilities of being scattered forward, in the direction it was originally traversing at.

iii. Electron Positron Pair Creation

An electron-positron pair can be produced if the incident photon has energy greater than $2m_ec^2$. This cannot happen in free space because energy and momentum cannot be conserved simultaneously, and a third body, usually a heavy nucleus, is required to absorb some of the momentum. This mainly occurs in a nuclear field, but if the photon's energy is $E_0 \geq 4m_ec^2$, it can be observed in a field of electrons (Figure 3). The process is described in the following equations.

$$E_0 = E_e + E_p + E_n + 2m_ec^2$$
$$\overrightarrow{p_0} = \overrightarrow{p_e} + \overrightarrow{p_p} + \overrightarrow{p_n}$$

E_e and E_p are excess energy after the creation of the electron and positron. The excess energy is split between the two particles as kinetic energy of their motion. The cross section for pair production is

$$\sigma_P = \frac{1}{137}\frac{e^4}{m_e^2c^4}Z^2\overline{P}$$ (Evans, 1955)

where P is a dimensionless function of hν and the kinetic energy of the produced electron. Its value varies from 0 when $h\nu = 2m_e c^2$ to ~20 when $h\nu \to \infty$. For very high energy photons, $\overline{P}$ can be shown to be

$$\overline{P} \sim \frac{28}{9}\ln\left(183Z^{-1/3}\right) - \frac{2}{27} \text{ (Evans, 1955).}$$

Putting the three main interaction processes for high energy photons together, the total mass attenuation coefficient is shown in Figure 4. Linear attenuation coefficient describes the fraction of the incident light that is absorbed or scattered per unit thickness of the absorber. The mass attenuation coefficient is the linear coefficient divided by the density. In this way, the mass attenuation coefficient is independent of the density of the absorber. The total linear attenuation coefficient is $\sigma = \sigma_a + \sigma_s + \sigma_K + \sigma_p$, where $\sigma_a + \sigma_s$ is the total linear attenuation coefficient of the Compton process where the absorption coefficient of the electron and the scattering coefficient of the photon is combined, σ_K is the attenuation coefficient of the photoelectric process, and σ_p is the attenuation coefficient of the pair production (Evans, 1955). For the Compton Effect, σ_a is the attenuation coefficient of the recoiled electron and σ_s is the attenuation coefficient of the scattered photon. This shows significant contribution from all three processes in the energy range of 500 keV and 5 MeV, which makes experimental study of this energy range difficult.

However, it also shows that the Compton process dominates in this energy range, and the pair production process dominates at higher energies.

B Gamma-Ray Telescopes

This section will discuss various methods for detecting gamma-rays.

i. Collimators

As gamma-rays cannot be focused, collimators are used to restrict background gamma-rays to enter the field of view. As a source moves through an aperture, the counting rate increases. It is made of material that is opaque to the incident radiation. The opaque material has numerous tiny apertures in it so that the incident beam only parallel to the aperture will be allowed through. This detector is suitable for high energy photons since it is unnecessary to consider diffraction as it would be for the optical spectrum. It is necessary to obtain background data from a source-free section of the sky and subtract is from the region where sources are expected to be present.

The modulation collimator is a collimator with another layer of absorber within the aperture in line with the first (Figure 5). This allows off axis sources to project a modulated pattern on the detector. In this manner any number of sources may be studied at the same time by using the appropriate response function and the motion of the modulators. A type of modulation mask with superior imaging system is the coded-mask. The opaque layer for this collimator has a random aperture pattern on it, which is placed at a distance from a position-sensitive detector. A source in any position in the sky will cast a unique shadow on the detector, and a sky map can be created by matching the aperture function of the collimator with the signal distribution recorded. The

disadvantage of this technique is that the noise or background from the entire detector contributes to the source background.

ii. Scintillation counter

A scintillation detector is a detector which scintillates when excited by ionizing radiation. The scintillation material may be either an inorganic crystal, such as sodium iodide and cesium iodide, or plastics with organic scintillation compounds. Sodium iodide and cesium iodide are favored for their high atomic numbers which leads to high cross sections for the photoelectric effect. The downside to this is the cost and difficulty of growing large crystals, compared with the low cost of readily available plastic scintillator. The incident photon liberates an energetic electron from the crystal, whose ionization energy loss produces optical photons via the scintillation process. These photons hit the semitransparent photocathode of a photomultiplier tube, which liberates photoelectrons via photoelectric effect. These electrons are accelerated, multiplied, and a large pulse arrives at the anode. The size of the pulse is proportional to the dE, the total energy liberated in the scintillating crystal. A sketch of this is shown in Figure 6.

iii. Phoswitch detector

A phoswitch detector is used to study hard X-rays and soft gamma-rays, and has two materials acting as scintillation detectors. One material is one that is sensitive to incident photons, such as NaI, and the other surrounds the first detector, and is made of

material less sensitive to photons such as plastic scintillators. When a high energy photon enters the detector, it triggers a signal from the first material but not the second. When cosmic charged particles enter the detector, it sends signals from both scintillators. Therefore, with the response time arranged in the readout system, unwanted signals from charged particles may be rejected. The readout system uses the "pulse shape" discrimination technique, where the X-ray photon gives a single pulse whereas a cosmic ray will produce two pulses with different shapes. Being able to discriminate between the different pulse shapes, the phoswitch detector has the advantage of collecting light signals with a single photomultiplier tube.

iv. Spark Chamber

A Spark Chamber is designed to detect pair production. It consists of a chamber with parallel metal plates. The chamber is filled with gas, usually a mixture of neon and argon. Alternate plates are connected to ground and a high voltage pulse is applied immediately after a selected gamma-ray interacts in the chamber. The resulting charged particles will ionize the gas in the chamber leaving behind an ionized pair trail. The high voltage is supplied on the plates so that the sparks can be seen where the ionized pair interacts with the produced electric field. This will allow the trail of the particles to be seen visually. The voltage cannot be supplied continuously because of breakdown betwen the plates will occur even without the charge. Therefore, triggering detectors are present underneath the plates. Only when the secondary pair particle triggers the

detectors will the voltage be supplied to the plates. An example of this is shown in (Figure 7), which is a schematic diagram of EGRET, a spark chamber detector (page 15).

C Past and Current Gamma-Ray Missions

There have been many gamma-ray missions launched in the last two decades. Their results provided more understanding and discoveries of the universe. Here, only a handful of these missions will be mentioned.

i. CGRO

On April 5, 1991, NASA launched the Compton Gamma Ray Observatory (CGRO). It was the largest payload flown at the time at 17 tons, and it carried four instruments to cover an unprecedented broad range of spectrum from 30 keV to 30 GeV (Kaluzienski & Shrader, 1999). The four instruments were the Burst And Transient Source Experiment (BATSE), the Oriented Scintillation Spectrometer Experiment (OSSE), the Imaging Compton Telescope (COMPTEL), and the Energetic Gamma Ray Experiment Telescope (EGRET). CGRO ended its 9 year operation on June 4, 2000, and was terminated via controlled re-entry.

a. BATSE, OSSE, and EGRET

BATSE is an all sky monitor sensitive to cosmic gamma-ray bursts in the energy range of 20 to 600 keV. It carries eight identically configured detector modules where each detector module contains two NaI (T1) scintillation detectors (Kaluzienski & Shrader, 1999).

OSSE is designed for observing the spectrum in the range of 0.05-10 MeV. It carries four NaI(T1)-CsI(Na) crystal phoswich detector systems that work independently of each other. OSSE makes 2-minute target source observations, followed by 2 minute of off-set observations. This sequence is repeated ending with the off-set observation on the other side of the source. The off-set observations serve as background spectra, which can be used for source positioning or more background modeling (Kaluzienski & Shrader, 1999).

EGRET is a spark chamber detector which detects gamma-rays in the energy range of 20 MeV to 30 GeV. It is also equipped with the Total Absorption Shower Counter (TASC) for energy measurement. The spark chamber alternates between tantalum foils and tracking layers and is filled with a noble gas-hydrocarbon mixture (Kaluzienski & Shrader, 1999).

b. COMPTEL

COMPTEL was developed by the Max Planck Institute for Extraterrestrial Physics (MPE). It consists of two scintillation detector arrays separated by 1.5 m. The upper detector consists of seven cylindrical modules with liquid scintillator NE 213A. Each cylinder is 27.6 cm in diameter and 8.5 cm thick with eight photomultiplier tubes (Kaluzienski & Shrader, 1999). The lower detector consists of 14 cylindrical NaI (T1) crystals, 28 cm diameter and 7.5 cm thick with seven photomultiplier tubes (Kaluzienski & Shrader, 1999). The surface area of upper detector is 4188 cm^2 and the lower one is 8620 cm^2 (Kaluzienski & Shrader, 1999). Each is surrounded by plastic scintillators for

shielding against charged particles. Two crystals in the lower detector also act as burst detectors, and are equipped with the Burst Spectrum Analyzer (BSA). One of them covers low energy range of ~100 keV to ~1 MeV, and the other covers higher energy range of ~1 MeV to ~10 MeV (Kaluzienski & Shrader, 1999). BSA is usually in the background mode where it reads out events at a reduced rate. When it receives a trigger from BATSE, it accumulates spectrum at an increased rate. In the event of a solar flare, BSA also operates in the burst mode. COMPTEL is capable of acting as a neutron detector. The incident neutron scatters off the nucleus of the hydrogen in the liquid scintillator then deposits energy in the lower detector, triggering a signal for double scatter (Kaluzienski & Shrader, 1999).

ii. INTEGRAL

On October 17, 2002, the European Space Agency launched the International Gamma-Ray Astrophysics Laboratory (INTEGRAL) into orbit. As a successor to CGRO, it orbits Earth every three days with an orbit of 9,000 - 155,000 km (Jensen, et al., 2003). INTEGRAL monitors gamma-rays in the range of 15 keV to 10 MeV as well as X-rays (4-35 keV) and the optical band (V-band, 550 nm) (Jensen, et al., 2003). It focuses on fine spectroscopy and fine imaging. It carries the Optical Monitoring Camera (OMC), the Joint European X-ray Monitor (JEM-X), the Imager on Board the INTEGRAL Satellite (IBIS) and the Spectrometer on INTEGRAL (SPI) (Jensen, et al., 2003). IBIS and SPI are the two analysis tools for gamma-ray. IBIS consists of coded aperture mask and two detectors; One 2600 cm^2 layer of $4 \times 4 \times 2$ mm^3 CdTe pixels and one 3000 cm^2

layer of $9 \times 9 \times 30$ mm^3 CsI-Photo diode pixels (Barr, et al., 2011). They are separated by 90 mm, allowing for 3D tracking as the photon interact with more than one element. They are capable of imaging sources in an energy range of 15 keV to 10 MeV (Barr, et al., 2011). IBIS is equipped with an active shielding system with the combination of a lead shielding tube and Bismuth germanate (BGO) veto scintillator system (Barr, et al., 2011). SPI performs spectral analysis of gamma-rays in the energy range of 18 keV and 8 MeV (Sanchez-Fernandez, Roques, & Diehl, 2011). It consists of 19 hexagonal high purity Germanium detectors cooled to an operating temperature of 85 K (Sanchez-Fernandez, Roques, & Diehl, 2011). Seventeen are currently operational. A hexagonal coded aperture mask sits 1.7 m above the detectors (Sanchez-Fernandez, Roques, & Diehl, 2011).

iii. Fermi

Fermi, formerly known as Gamma-Ray Large Area Telescope (GLAST), is a large area telescope designed to observe gamma-rays in the energy range of 20 MeV to more than 300 GeV (Johnson & Mukherjee, 2009). It is an internationally collaborative mission lead by NASA, and was launched on June 11, 2008. It is designed for a 5 year mission life, with a goal of 10 years of operation (Johnson & Mukherjee, 2009). It is pair-conversion telescope without the need of gas, consisting of 16 modules. Each module has 16 interweaving thin layers of high Z tungsten and silicon strip detectors, each 400 μm thick (Johnson & Mukherjee, 2009). Below it is an 8-layer CsI calorimeter, and each module is surrounded by plastic scintillators to shield against charged particles

(Johnson & Mukherjee, 2009). The incident high energy photon will interact with the tungsten and generate an electron-positron pair. This will be tracked through the silicon layers and subsequently absorbed by the CsI calorimeter (Johnson & Mukherjee, 2009).

D. Gamma-ray Observations

Many exciting results have been made in high energy astrophysics. A handful of them will be discussed.

i. Galactic Center

Sagittarius A is a complex radio source at the center of the Milky Way which consists of several components. One of them is Sagittarius A*, a Black Hole candidate with a mass of $4.31\times10^{6} M_{\odot}$ (Gillessen, et al., 2009). It is a faint X-ray source compared to supermassive Black Holes in other galaxies. A giant molecular cloud, Sagittarius B2 is located 100 pc from the Galactic center (Revnivtsev, et al., 2004). Its 2 – 10 keV spectra show an absorbed continuum emission with a superimposed strong 6.4 keV diffuse emission line (Revnivtsev, et al., 2004). This spectra is assumed to be produced by Sgr B2 reradiating photons from Sgr A* via Comption scattering (Revnivtsev, et al., 2004).

In 1988, a high altitude balloon experiment carrying a germanium detector was launched. They observed the supernova 1987A at 844.1 keV and 1239.9 keV (Rester, et al., 1989). OSSE on CGRO made a contiguous 8 week observation on the Galactic Center. They created a sky map of the 511 keV positron annihilation line radiation which

showed a central bulge component and emission on the Galactic plane with an extended emission at positive latitudes above the Galactic center. They found that positrons from the currently observed ^{26}Al do not sufficiently account for the observed 511 keV flux along the Galactic plane. Postulation for the asymmetrical positron outflow include enhanced supernova activity, jet activities from Black Holes near the Galactic center, a single gamma-ray burst which occurred 10^6 years ago and local source emission (Purcell, et al., 1997).

INTEGRAL observed the Galactic Center region for 2.3 Ms using IBIS, and confirmed that Sgr B2 was echoing violent activities from Sgr A* which lasted 10 years 300 years ago (Revnivtsev, et al., 2004). Using IBIS, INTEGRAL was able to detect a hard X-ray source IGR J17456-2901 in the 20-100 keV range, which is located within one arc minute from Sgr A*. After observing for 4.7×10^6 seconds, they concluded that this emission is not explained by a hot plasma, transient X-ray source, nor by flares from Sgr A*, but possibly related to the Supernova Remnant Sgr A East. They also observed that IGR J17456-2901 is not pointlike, but a compact, diffuse emission region (Belanger, et al., 2005). INTEGRAL produced a cumulative report on observations of the Galactic bulge made by all detectors on board. It was able to see 15 neutron star low mass X-ray binaries, including 10 X-ray bursters. Some X-ray bursts were seen to be anti-correlated with the soft X-ray emissions. Along with these observations, they have discovered 6 new X-ray sources (Kuulkers, et al., 2007).

INTEGRAL, with the IBIS imager, observed an unexpected asymmetry in the 511 keV line emissions from the Galactic center. They detected a larger flux from the

negative longitudes than from positive longitudes. This distribution is consistent with their observation of the low mass X-ray binary (LMXB) in the hard X-ray range. The positrons for the electron-positron annihilation are suggested to come from the hot inner regions of the accretion disks of the LMXB (Weidenspointner, et al., 2008).

ii. ^{26}Al Emission

^{26}Al has a half-life of 7.16 x 10^5 years, and emits 1.8086 MeV gamma-rays as it decays to ^{26}Mg. The discovery of its diffuse emission lead to the conclusion that it is produced by massive stars throughout the Galaxy (Mahoney, Ling, Wheaton, & Jacobson, 1984). However, COMPTEL's 2.5 years observation generated a sky map with localized emission from the inner galactic region (Diehl, et al., 1995). SPI's observations suggest that ^{26}Al emissions may originate in localized star forming regions, and that its source co-rotates with the Galaxy (Diehl R. , et al., 2006) (Diehl R. , et al., 2006). Further studies showed that the ^{26}Al emission lines are significantly blue-shifted in the 4th quadrant of the Galaxy, but not significantly red-shifted in the 1st quadrant, implying an asymmetric rotation (Wang, et al., 2009). Further studies will contribute more to understanding the shape of the Galaxy.

iii. Pulsars

EGRET's 3rd catalog contained 170 unidentified sources including pulsar candidates (Hartman, et al., 1999). Other subsequent observations were able to associate

some of EGRET's unidentified point source as young pulsars (Kramer, et al., 2003). Harding and Muslimov proposed a new slot gap model for pulsar emission, combining two existing polar cap and outer gap models. With this model, they predicted an undiscovered excess of X-ray and gamma-ray loud, radio quiet pulsars (Harding & Muslimov, 2004). Fermi has discovered a host of pulsars that suggest many radio quiet, X-ray or gamma-ray loud pulsars may be expected to be discovered (Abdo, et al., 2008).

iv. Blazars

Active Galactic Nuclei (AGN) are galaxies with point-like cores which are more luminous than the other Galactic stars combined. The source at the core is believed to be a super massive black hole. Blazars are AGN with one of the accretion jets pointing directly to the line of sight to the Earth.

EGRET's first catalog included 25 AGN of high confidence (Fichtel, et al., 1994). OSSE detected 5 of these EGRET blazars in addition to 2 new blazars. The combined spectra show spectral softening in the 1-15 MeV energy range (McNaron-Brown, et al., 1995). EGRET's third catalog included 66 high confidence blazars and 27 possible AGN (Hartman, et al., 1999). COMPTEL detected 10 of EGRET's blazars (Collmar, et al., 1999).

INTEGRAL published a catalog of hard X-ray observations for the first time, using IBIS (Krivonos, Revnivtsev, Lutovinov, Sazonov, Churazov, & Sunyaev, 2007). Further studies by Swift on its unidentified object determined it to be a blazar (Bassiani, et al., 2007). The second INTEGRAL catalog included 187 sources, including 162

Seyfert AGN and 18 blazars (Beckmann, et al., 2009), and Fermi was able to detect 15 of them using its large area telescope. The combined observational analysis in the hard X-ray and gamma-ray band could lead to understanding more about AGNs (Beckmann, Ricci, & Soldi, 2009). VERITAS, a ground based gamma-ray telescope, observed a very high energy blazar (Acciari, et al., 2010).

E. Conventional Compton Telescope

An example of a conventional Compton telescope can be seen in Figure 8. It has two detector arrays separated by 150 cm. The upper array acts as the converter, surrounded by an anticoincidence shield. An incoming gamma-ray undergoes the Compton process with one of the cells and ejects an electron. The electron deposits energy in the scintillation liquid which is read by the photomultiplier tube. The scattered gamma-ray leaves the liquid scintillator, and is absorbed by the lower detector or calorimeter. This is also surrounded by an anticoincidence shield. An event is recorded when a signal from a lower detector cell is in coincidence with the signal from a liquid scintillator cell. The time-of-flight of the scattered gamma-ray is measured.

The trajectory of the scattered photon can be traced by the two cell locations of the interactions in the two detectors. The energy of the incident photon, E_0, is simply the energy of the liberated electron measured in the converter and the energy of the scattered photon, E', measured from the NaI calorimeter. From Equation 8, the Compton angle is

$$\cos\theta = 1 - \frac{m_e c^2}{h}\left(\frac{1}{E'} - \frac{1}{E_0}\right)$$

From this, the incident photon can be traced to a point in the sky somewhere on the circular projection ("event circles") of the outer surface of a "cone" with half-angle θ and axis defined by the trajectory of the scattered photon Figure 8. Plotting event circles for all events, the source direction can be found from the intersection of the circles.

i. Limitation of Conventional Compton Telescopes

Past Compton telescopes ((Schonfelder, Hirner, & Schneider, A Telescope for Soft Gamma Ray Astronomy, 1973) (Herzo, et al., 1975) (Zych, Dayton, Tumer, & White, 1983) (Schonfelder, et al., 1984)) and more recent concepts using germanium strip detectors ((Kroeger, et al., 1995) (Boggs, et al., 2003)), thick silicon detectors (Kurfess, Johnson, Kroeger, & Philips, 2000), and liquid Xenon time projection chambers (Aprile, Bolotnikov, Chen, & Mukherjee, 1993) can only determine the incident direction of each photon to an event circle defined by the angle θ, with uncertainty $\Delta\theta$. This forms an event annulus with width $\Delta\theta$. This annulus is shown in Figure 9. The angle θ and its uncertainty due to the energy resolutions are given below. $E_0 = E_{e^-} + E'$, where E_e^- and E' are the measured recoil electron and scattered photon energies, respectively. $m_e c^2$ is the electron rest mass energy.

$$\theta = \cos^{-1}\left[1 - m_e c^2\left[\frac{1}{E'} - \frac{1}{E_0}\right]\right]$$

Equation 13

$$\Delta\theta = \frac{m_e c^2}{\sin\theta}\left[\frac{\Delta E_{e^-}^2}{E_0^4} + \Delta E'^2\left[\frac{1}{E'^2} - \frac{1}{E_0^2}\right]^2\right]^{1/2}$$

Equation 14

The overall uncertainty in θ depends on both the uncertainties in the calculated scatter angle and the scattered photon direction. The latter is given by the interaction position resolutions and separation of interaction sites in the converter and calorimeter. The former includes the inherent detector energy resolutions and Doppler broadening that occurs in the Compton interaction due to the nonzero momentum of the bound atomic electrons of the target material. This shows up as an energy fluctuation in the Compton scattered gamma-ray.

Using standard image reconstruction techniques with event circles it is possible for determining source locations. The fundamental limitation of this approach is that gamma-ray events from any incident direction within each event annulus contribute to the source background. This allows gamma-rays incident at large angles with respect to the source direction to contribute to the source count background. With several sources within the telescope's field-of-view, events from one source can contribute to the image of the other(s). With conventional Compton telescopes, one usually restricts events to small θ-values to minimize the background contributions. This, in turn, significantly reduces the effective area of the telescope. It is also necessary to find a source-free region of the sky to subtract the background gamma-rays. If the direction of the recoil electron can also be determined, then the incident gamma-ray direction can be determined uniquely. Gamma-rays from a discrete source in the sky can then be

represented by a clustering of incident photon directions without background contributions from unrelated parts of the sky.

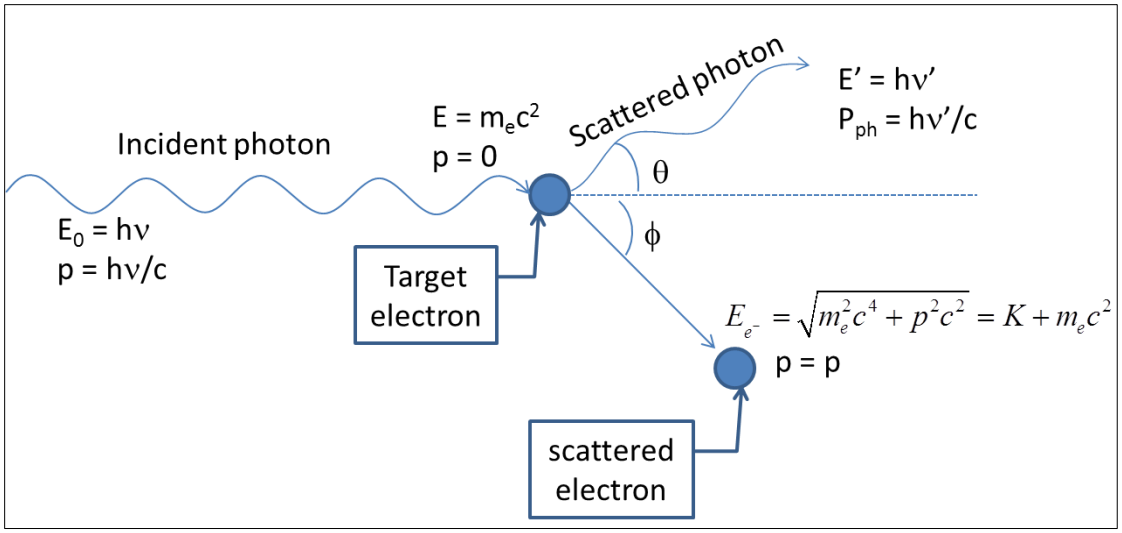

Figure 1 Mechanism of a Compton scatter

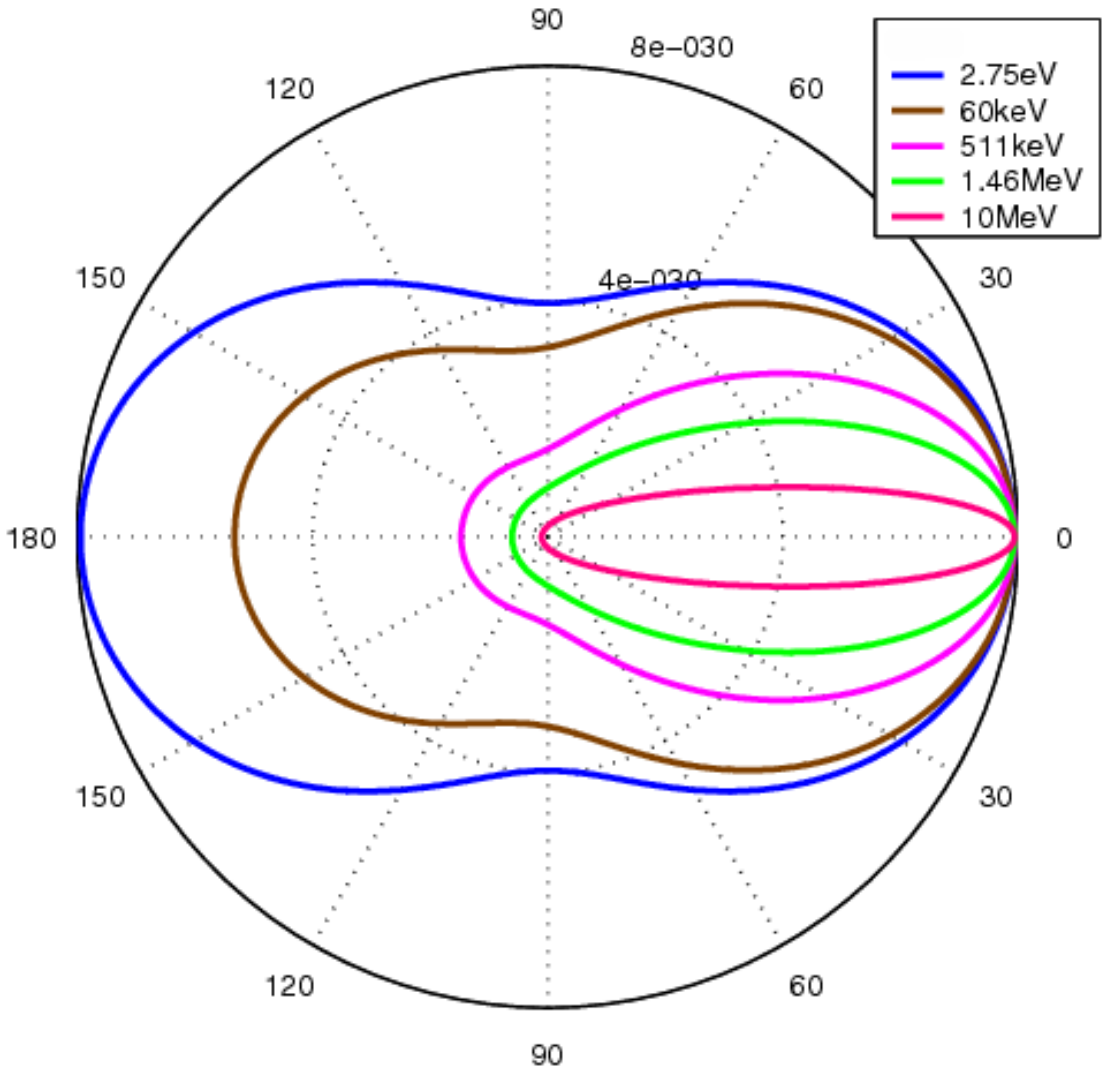

Figure 2 The Klein Nishina Formula. Each curve shows the distribution of the photon scattered angle, corresponding to different incident energies. As the incident energy increases, the distribution becomes more limited to the forward direction. [http://upload.wikimedia.org/wikipedia/commons/0/09/Klein-Nishina_distribution.png]

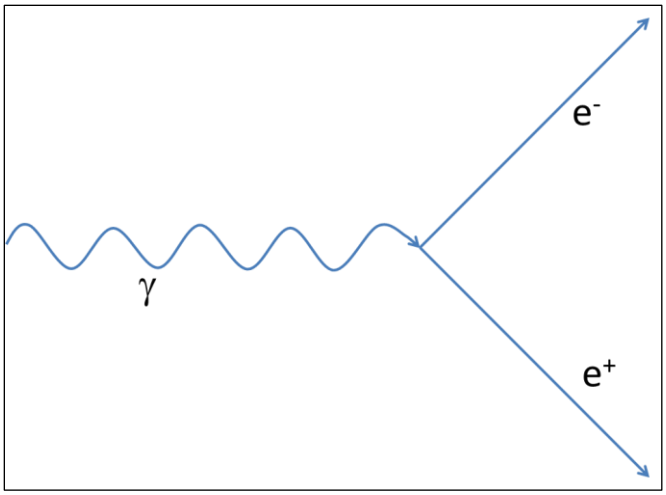

Figure 3 Positron Pair Creation

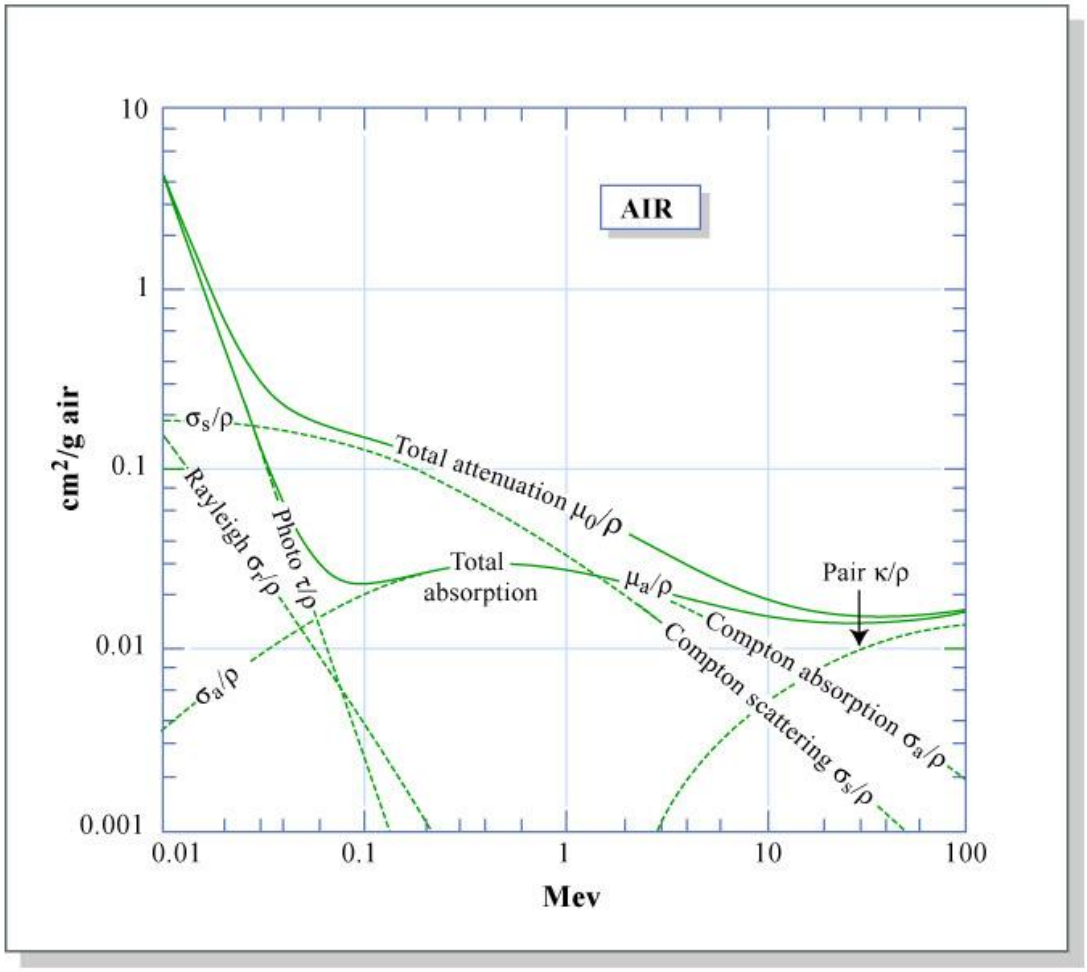

Figure 4 Total attenuation of gamma-ray in air. Between 0.5 MeV and 5 MeV, all three processes (photoelectric, Compton, and pair) have significant contribution, but Compton interactions dominate. [http://www.flickr.com/photos/mitopencourseware/3775266331/]

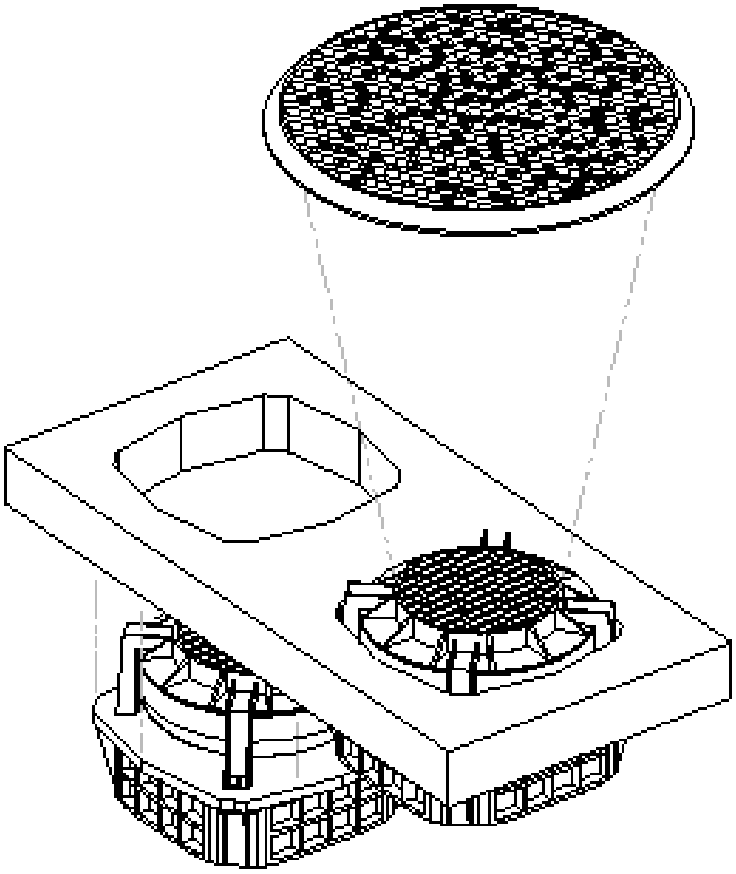

Figure 5 Schematic of JEM-X, a coded mask telescope aboard INTEGRAL. [http://integral.esa.int/integ_pictures.html#jem-x]

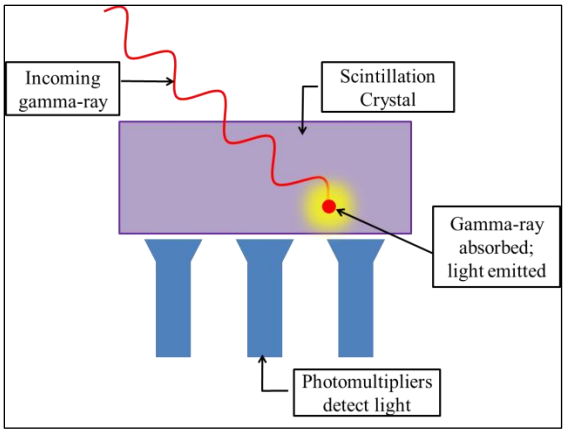

Figure 6 A sketch of a scintillator

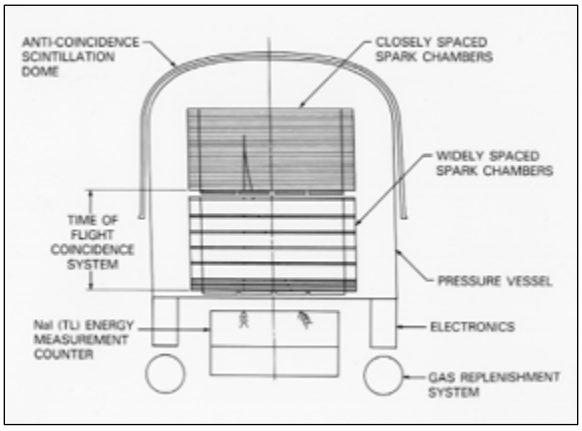

Figure 7 Sketch of Egret, a Spark Chamber (Johnson & Mukherjee, 2009)

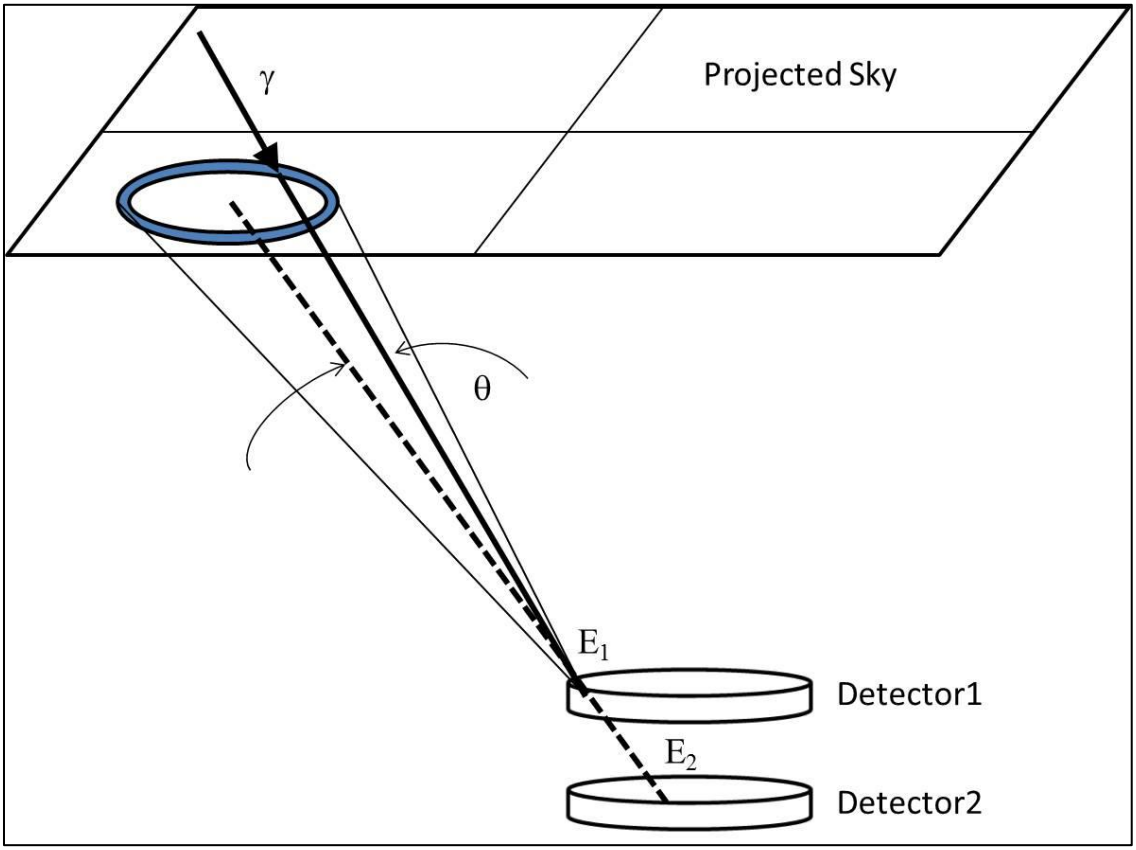

Figure 8 A traditional Compton telescope.

Incident gamma-ray will release an electron in Detector 1, and the scattered photon is absorbed by Detector 2. From the Compton formula, the Compton angle can be calculated, and the incident photon can be determined to originate from somewhere on the red ring.

Chapter 3 TIGRE Prototype Balloon Instrument

The UCR Tracking and Imaging Gamma Ray Experiment (TIGRE) consists of multi-layers of thin silicon strip detectors to convert and track gamma-ray events from 0.5-100MeV. In this energy range, Compton scatter events are reconstructed by measuring the directions and energies of both the scattered gamma-ray and recoil electron. The TIGRE Compton telescope concept is shown in Figure 9. TIGRE utilizes electron tracking between the thin silicon layers to provide the final information needed to completely reconstruct the incident photon and determine a unique incident direction for each photon event. This is achieved by tracking the recoil electron and determining its direction and energy and combining these with the scattered gamma-ray's energy and direction. In this way TIGRE removes the azmuthal uncertainty, described previously in page 24, in the incident direction along the event circle. This assists improved background rejection, image reconstruction and sensitivity. The silicon converter/tracker also serves as an electron-positron pair detector for gamma-rays up to 100 MeV without the inherent loss of angular resolution characteristic of pair telescopes with high-Z converter materials. This is important for extending the results obtained with higher energy telescopes such as Fermi down to 10-100 MeV.

The various telescopes components have been configured to fit within the existing dimensions of a previous UC Riverside balloon-borne thin-walled pressure vessel (see Figure 10 & Figure 11). The entire detector support structure is shock-mounted on a large rigid aluminum honeycomb panel that is mounted to the pressure vessel support frame. The various electronics crates (VME, CAMAC and NIM) are mounted to the

frame below the honeycomb panel along with the DC/DC converters. Four 256 element CsI(T1)-Photodiode arrays, a plastic scintillator charge particle shield and an array of 5cm thick NaI(T1) position-sensitive scintillation detectors below the tracker/converter complete the telescope configuration.

At the basic level, Compton telescopes use two gamma-ray detector elements in coincidence; ideally, the first is a low-Z converter to favor Compton scattering over photoelectric absorption (Hiller p57, Figure 8). The second is a high-Z calorimeter to completely absorb the scattered photon. Both detector elements are position sensitive and measure the energy loss (E) and location (x, y, z) of the interactions (Tumer, et al., 1995); (O'Neill, et al., 1995). The MPE MEGA instrument is similar to this (Kanbach, et al, 2003).

A. Silicon Strip Converter/Tracker

TIGRE prototype instrument consists of 16 layers of $10\ \text{cm} \times 10\ \text{cm} \times 300\ \mu\text{m}$ thick double-sided silicon strip detectors. These boards are positioned with 1.52 cm spacing to create a 16-layer stack. The double-sided silicon strip detectors provide submillimter x, y and z spatial resolutions as the recoil electron is tracked through successive layers until it is fully absorbed. This allows measurements of the direction and energy of Compton electrons and electron-position pairs. Figure 12 shows a single double-sided detector and printed circuit board. Micron Semiconductor Ltd. developed these detectors for our specific application.

Each side of the detector has 128 orthogonal strips with a pitch of 0.758 mm. The detectors are fully depleted at a bias voltage of 40 volts (±20 volts) where the single detector leakage current is typically 2 μA. An 80 MΩ polyscin bias resistor is fabricated on the wafer at the end of each strip. Each layer consists of a mosaic of four detectors for a sensitive area of 400 cm^2. The electron track's energy loss and scattering in the silicon detectors allows its direction-of-motion to be determined, providing directional discrimination for the incident photon. Each 16-layer stack is called a tower. Four of these towers positioned orthogonal to one another creating four towers of silicon detector.

Each junction and ohmic strip is connected to a channel of one of two 128-channel ASIC chips on the detector board. Each ASIC channel features charge sensitive preamplifiers and shaping amplifiers with associated sample-and-hold, trigger and serial readout circuitry. The prototype balloon instrument has a total of 64 silicon detectors. Triggers from each detector board are OR'ed to produce the converter/tracker trigger. Figure 13 shows a ^{57}Co (122 keV) spectrum of a single junction strip from one detector. All 7,680 junction strips are calibrated individually. The ohmic-strip pulse heights were not used for the energy loss measurements.

B. CsI(T1)-Photodiode Calorimeter

TIGRE uses CsI(T1)-photodiode detector arrays surrounding the converter/tracker on the sides as a calorimeter for the scattered photons and as a critical low energy gamma-ray shield. The shield is important at energies below 1 MeV where directional discrimination of the gamma-rays is less certain due to the shortness of some of the

electron track lengths. The side CsI(T1) arrays enhance the instrument's capabilities as a gamma-ray polarimeter for energies below 2 MeV.

Each of the 4 arrays consist of 256 $1\,\text{cm} \times 1\,\text{cm} \times 3.5\,\text{cm}$ long CsI(T1) crystals (Hilgar Ltd.), individually wrapped with multilayers of Teflon tape and bonded to 1cm^2 photodiodes (Hamamatsu S-3590-03) to measure the energy and direction of the scattered gamma-ray. Single crystal spectra with discrete electronics consistently gave 5% (fwhm) resolution at 662 keV. Each array is read out using two of the same ASIC chip used for the silicon detectors. Figure 14 shows one of these arrays. The total array bias current is typically 0.5 µA with a bias voltage of +40 volts.

C. NaI(T1)-PMT Calorimeter

Eight $1\,\text{m} \times 5\,\text{cm} \times 5\,\text{cm}$ NaI(T1) scintillator bars have been added below the Si converter/tracker to detect and absorb pair-produced positrons and electrons. These scintillators are from a previous balloon experiment and are shown in Figure 15. Photomultiplier tubes are coupled to both ends of each bar with right-angle acrylic light pipes. Due to the attenuation of the pulse heights with distance of the interaction from each end of the bar, the two pulse heights can be combined to yield an energy-independent parameter related to the position of the interaction along the bar. For this purpose, we use the difference in the two pulse heights divided by the sum of the pulse heights. There is a discontinuity at the center position of the bar due to the optical interface between the two single crystals that make up the full length of the bar. The calibration curve allows us to determine the location and energy loss for radiation in the

bars. The bars also provide needed shielding from lower energy atmospheric gamma-rays. The eight PMT signals from each side of the array are summed and coincidences between the two sides are used to register a possible interaction. In post-flight analysis, when the energy converted pulse height is larger than 60 keV, the event is considered a valid interaction.

D. Plastic Scintillator Charged Particle Shield

A thin plastic scintillator surrounds the entire sensitive material to discriminate against cosmic rays. Six sheets of 0.635 cm thick plastic scintillator, with 4 Photomultiplier Tubes (PMTs) face-coupled to each sheet, surround the Si converter/tracker, CsI-PD arrays and the relevant sections of the NaI-PMT bars. Forty (40) photomultiplier tube assemblies are required for the charged particle shield and NaI(T1) bars. Each has a built-in computer-controlled low-power DC/DC high voltage power supply. The CAMAC and NIM electronics are primarily used for the PMT signals.

E. ASICs and Readout System

The front-end readout for the silicon and CsI(T1) detectors are implemented with custom Application Specific Integrated Circuits (ASIC) circuits that, in turn, are controlled individually via addressable interface boards and VME digital I/O modules. An embedded low power Pentium III processor controls the entire ASIC biasing and

monitoring as well as the data readout and data storage. Each 128-channel front-end readout chip (TAA-1, IDE AS, Oslo) is mounted on our custom ceramic chip carrier. The TAA-1 is specifically designed for asynchronous operation.

Each chip provides a prompt asynchronous signal-above-threshold trigger. Event coincidence requires trigger overlaps from at least one of the 64 silicon detector boards and one of the four CsI-PD arrays or one of the eight NaI-PMT bars with no signal from the charged particle shield. The timing is arranged so that the leading edge of the silicon trigger generates the *hold* signal needed to sample the peak value of all the ASIC shaper pulses. Coincidence signals from the PMTs at both ends of the NaI scintillation bars are required. When the external coincidence criteria are met, each pair of detector chips is read out serially with a VME 96-channel 12-bit ADC (Pentland Industries). Figure 16 shows a triggered event from a single silicon detector board. The negative (junction) side is used for position and energy whereas the positive (ohmic) side is used for position only. At a sampling rate of 85 kHz all the ASIC channels are digitized and buffered in the ADC FIFO memory in 3.0 ms. With ~36,000 bytes of information per event and a total of 500 GB of on-board hard drive data storage capacity, a maximum counting rate of ~80 events/s can be sustained for 48 hours. This is substantially higher than we expect during a balloon flight with the prototype instrument, given the limited amount of silicon in the converter/tracker. Only systems rates, which include several burst counters with 5 ms time resolution, and housekeeping parameters are telemetered to the ground command station in real time. A clock (and stable oscillator) provides an event time stamp with an accuracy of 10 μs (UTC).

UTC is determined with our ground-station GPS clock. Three-axis magnetometer readings with each event provide the telescope's orientation to an accuracy of 0.5º. Both a limited number of discrete commands to manage the instrument's power and a full range of digital word commands for the individual detector control are utilized. Figure 17 shows a block diagram of the main telescope systems.

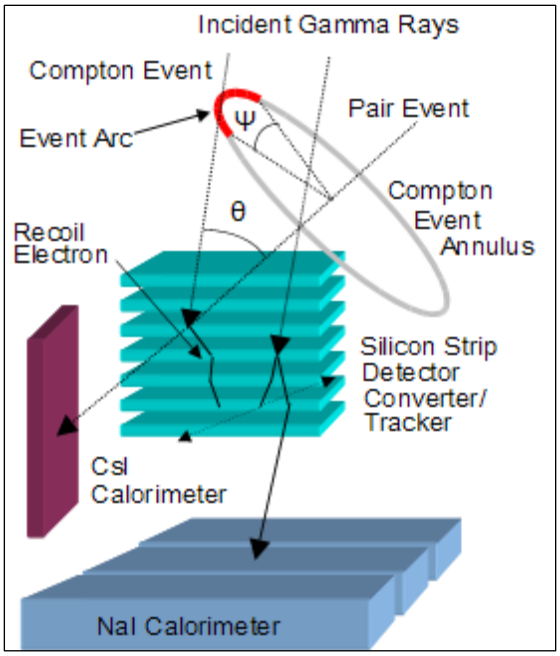

Figure 9 TIGRE's design. The electron tracking capability allows for a more precise reconstruction of the incident photon.

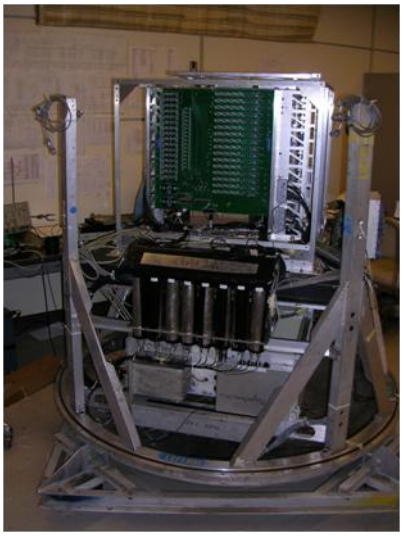

Figure 10 TIGRE Prototype Balloon Instrument

Figure 11(cw) Single Si layer, pressure vessel, detector support structure and bias control box.

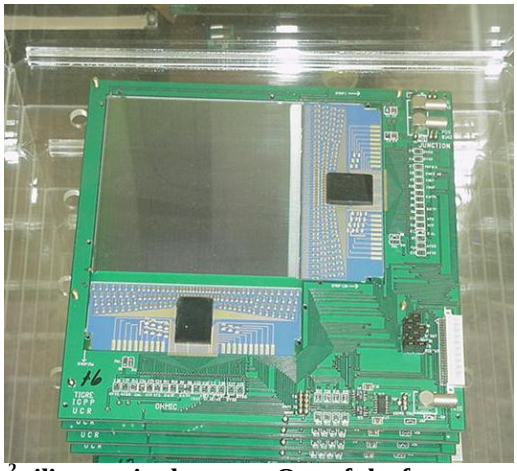

Figure 12 100-cm^2 silicon strip detector. One of the four towers is shown here.

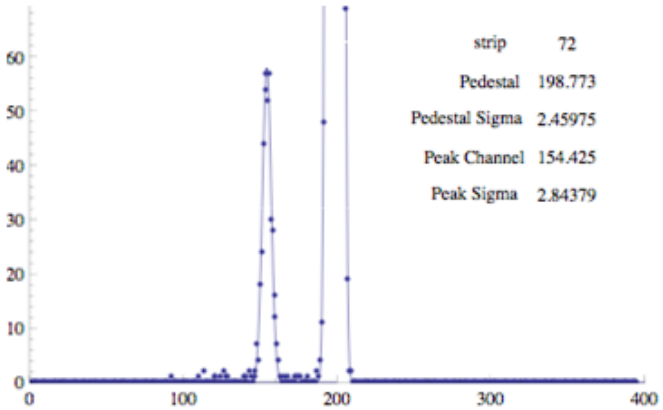

Figure 13 Single-strip energy spectrum for 122 keV γ-ray (on left) with truncated pedestal peak.

Figure 14 CsI-PD array with cover removed.

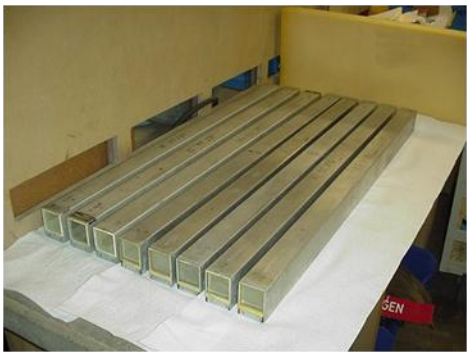

Figure 15 NaI(Tl) scintillator bars

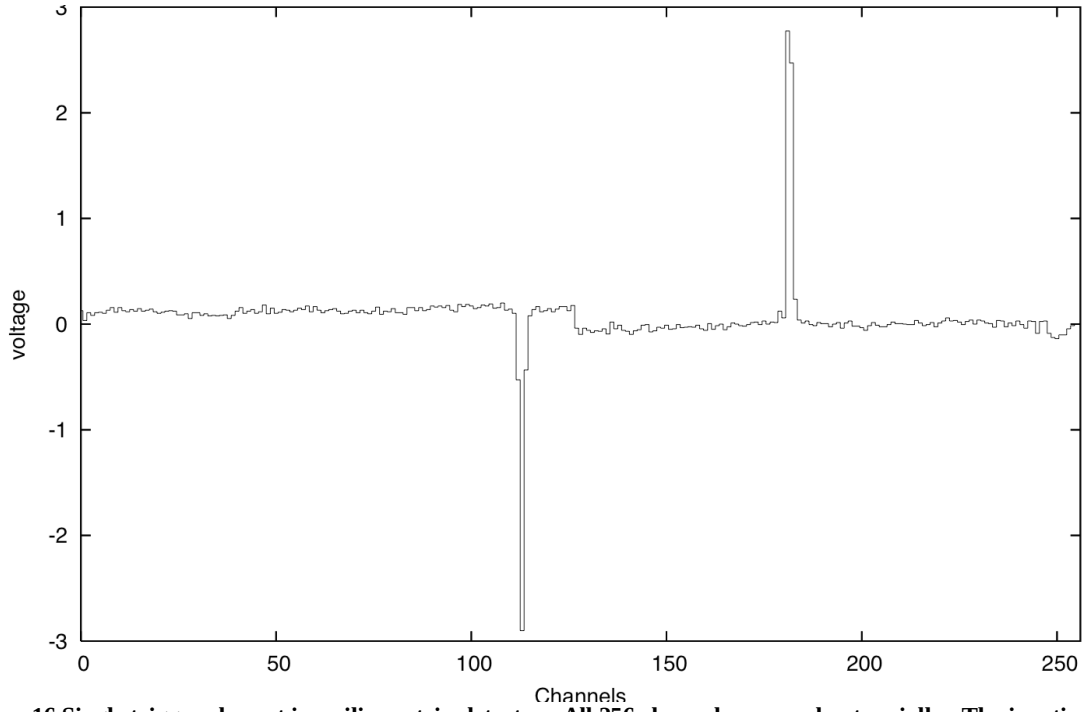

Figure 16 Single triggered event in a silicon strip detector. All 256 channels are read out serially. The junction signal is negative and the ohmic signal is positive.

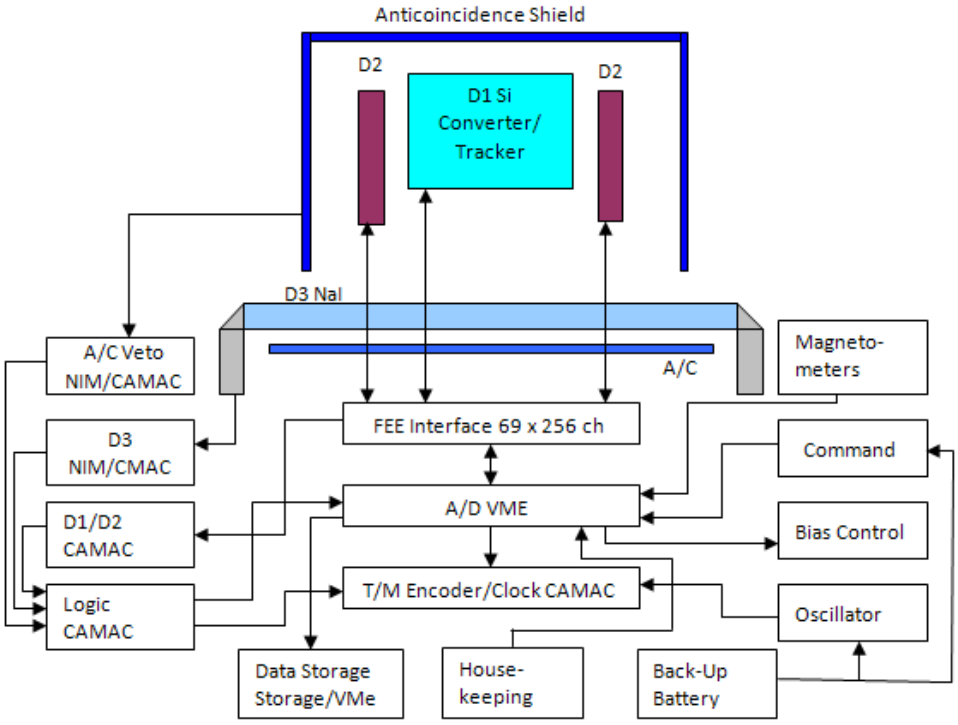

Figure 17 Block diagram of primary telescope systems

Chapter 4 Expected Performance

Each components of the prototype telescope were thoroughly tested and calibrated for optimum detection of Compton events. This chapter describes them in detail.

A. Recoil Electron Tracking

As a low-Z material (Z=14) the Compton effect in silicon dominates above 100 keV, making it an ideal converter. As a tracker, recoil electrons can still be tracked between successive layers at gamma-ray energies below 1 MeV (O'Neill, et al., 1995). For eample, at 0.511 MeV, 9% are tracked events. At 0.900 MeV this number is 20%. TIGRE still operates as a conventional Compton telescope when the electron stops in a single layer and cannot be tracked. Monte Carlo simulations show that the percentage of tracked events is 57, 82, 94, and 94% for 1, 2, 6, and 10 MeV gamma-rays.

The direction of the recoil electron is determined from the positions in the layer of the initial interaction and the adjacent layer (details at page 102). Recoil electron tracking gives a unique incident direction for each event. This direction can be compared with the true incident direction. The electron-tracking feature translates into a simulated radially symmetric point-spread-function (PSF) shown in Figure 18 for a 1-30 MeV Crab-like source. The source directions for individual simulated events are summed to construct the PSF.

Minimum ionizing particles (MIPs) traversing 300 μm of silicon produce on the average 25,000 electron-hole pairs (277 e/keV) that can be collected within 10 ns because of their high mobility. The most probable energy loss in thin silicon detectors is 26-

keV/100 μm. Preliminary measurements for a single detector strip gave 4.6 keV(1-σ) at 122 keV (O'Neill, el al., 2003). An energy calibration curve for the lines from ^{133}Ba is shown in Figure 19. Figure 20 shows a full detector hit pattern for an uncollimated ^{90}Sr beta source near the center of the detector surface. The full detector is self-triggering.

TIGRE has been implemented with a tracking and a non-tracking mode. In the tracked mode, TIGRE only records events which have electron tracks by requiring an event to have more than two silicon interaction in successive layers. In the non-tracked mode all events and hits are accepted. The latter situation allows for classical Compton analysis, where only one interaction in the tracker is in coincidence with an interaction in the calorimeter. The former tracked feature allows for more precise reconstruction of the incident gamma-ray.

B. Unique Incident Direction

In the schematic diagram for a Compton scattered event shown in Figure 9, the event circle is dictated by the positions and energies measured with the silicon strips and CsI(T1) crystals. TIGRE, with its ability to track the Compton scattered electron, constrains the event to a plane that includes the incident photon direction. The scattered electron direction is obtained from the first and second interaction positions in the silicon detectors. TIGRE uses a Direction-of-Motion parameter (DOM) to determine the beginning of the electron track. The scattered electron is required to have a velocity component in the direction of the incident photon (forward scattered). In reality, the event incident direction is constrained to a length of arc length ψ along the Compton

event circle due to the electron multiple Coulomb scattering for electrons produced by ~MeV gamma-rays.

C. TIGRE Compton Telescope Sensitivities

TIGRE is designed as a prototype for a full-sized Compton telescope designed for future Long Duration or Ultra Long Duration balloon flights (ULDBF). Its potential performance and sensitivities were simulated (O'Neill, el al., 2003); (Bhattacharya, O'Neill, Akyuz, Samimi, & Zych, 2004) using the Los Alamos Monte Carlo Neutron Photon (MCNP) code. The model of the full scale telescope had thirty-two silicon layers with an area of 1600 cm^2. The energy and spatial resolutions for the converter/tracker were taken to be 3 keV (1-σ) and 0.75 mm, respectively. Thresholds of 30 keV, 100 keV, and 100 keV for the silicon, CsI, and charged particle shield were used. The standard scaleable resolution (5% at 662 keV) for the CsI(T1) was used. The telescope gamma-ray background was simulated and scaled to the level expected at an altitude of 40 km (3 mbars). The atmospheric fluxes were taken from our previous balloon flight results (Akyuz, et al., 1997) and modeled over the full 0-180º zenith-angle range. Source fluxes were simulated using a Crab-like E^{-2} power law spectrum. The smaller cosmic diffuse gamma emission was not included in the downward background at 3 mbars.

TIGRE's energy-averaged angular resolution for a Crab-like source is 1.7º (1-σ) at 1 MeV, depending primarily on the distance, size, and energy resolutions of the CsI detectors. The absolute detection efficiency of TIGRE is 5% giving a high effective area of 80 cm^2 at 1 MeV. At 1 MeV the energy resolution is 18 keV (1-σ). TIGRE's

background was significantly reduced by accepting events with scatter angles greater than 35º and within the 70º half-angle FOV. With a 7-hour exposure to the Crab Nebula and Pulsar at zenith, it will be detected with a 9.6-σ statistical significant while the same source at 30º off-axis will be detected at 7.5-σ (Akyuz, Bhattacharya, O'Neill, Samimi, & Zych, 2003). When the electron tracking information is disregarded the corresponding sigma-values are 3.8 and 3.3. The 9.6-σ significance represents a 3-σ sensitivity of $4\times10^{-4}\ \mathrm{ph}\cdot\mathrm{cm}^{-2}\cdot s^{-1}$.

For Ultra Long Duration Balloon flights with ~100-day observations, the single source flux sensitivity is improved by a factor of ten. Mid-latitude Long Duration Balloon flights of ~10 days will improve our sensitivity by a factor of three. An improvement in the angular resolution from 2º to 0.4º with improved calorimeter materials (e.g., CZT or Ge), will improve the sensitivity by another factor of 2.2. For a 100-day observation with TIGRE and an improved calorimeter (2 keV, 1-σ), the broad line sensitivity at 1.8 MeV (^{26}Al) is $1.4\times10^{-6}\ ph/cm^2\cdot s$.

D. Doppler Broadening

Doppler broadening occurs in Compton interactions due to the nonzero momentum of the bound atomic electrons of the target material. This shows up as an energy fluctuation in the Compton scattered gamma-ray. TIGRE measures the full energy of recoil electron and the scattered gamma so that the total event energy is unaffected. However, this effect causes an error when the Compton scatter angle, θ, is

calculated with Equation 13, affecting the angular resolution of the telescope. Multiple Compton interactions and high-Z converters both work to increase this effect. TIGRE uses single interactions in silicon so that the effect of Doppler broadening is minimized. This also greatly simplifies the event reconstruction. For low energy incident photons of a few 100 keV in germanium detectors, the Doppler broadening uncertainty in θ can approach $\Delta\theta$ as given in Equation 14, caused by the energy resolutions. Figure 21 shows our calculated angular resolutions, including the contribution from Doppler Broadening, for 60º Compton scatters. The Doppler broadening calculations followed the method of Ribberfors (1983), Namito, Ban, & Hirayama, (1994) and the tables of Biggs, Mendelsohn, & Mann (1975). As shown in Figure 21, the limiting energy resolution of the CsI(T1) detectors dominates the angular resolution in the MeV range. With a Ge calorimeter with energy resolutions of a few keV this can be reduced to 0.3º (1-σ). This is just below the 0.4º (1-σ) limit due to Doppler broadening in silicon at 1 MeV. For higher-Z converters this effect is more severe. An Advanced Compton Telescope based on the TIGRE concept with a silicon converter/tracker and Ge or CZT calorimeter will be able to work at the DB limit.

E. Polarization

Compton telescopes are natural gamma-ray polarimeters, making use of the polarization dependence of the Klein-Nishima cross section for large angle Compton scatter events. The response of a polarimeter can be described in terms of the measured azimuthal angle distribution of the Compton scattered photons for an incident linearly

polarized beam of gamma-rays. According to the Klein-Nishima cross section the polarization is most detectable for scattering angles near 90º. Thus, TIGRE's well-type calorimeter design makes it well suited as a gamma-ray polarimeter for energies below 2 MeV. The polarimetry properties of the TIGRE Compton telescope have been fully described in Akyuz, et al., (1995). A conventional balloon observation with the full-area TIGRE instrument (1,600 cm^2) will be able to detect polarized gamma-rays at the 10-20% fractional polarization level for source fluxes comparable to the Crab flux.

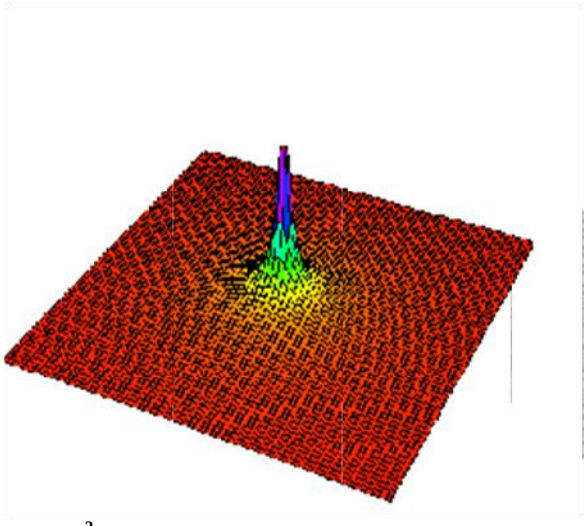

Figure 18 PSF for an E^{-2} discrete source above 1 MeV. The full FOV is 140^{O} x 140^{O}

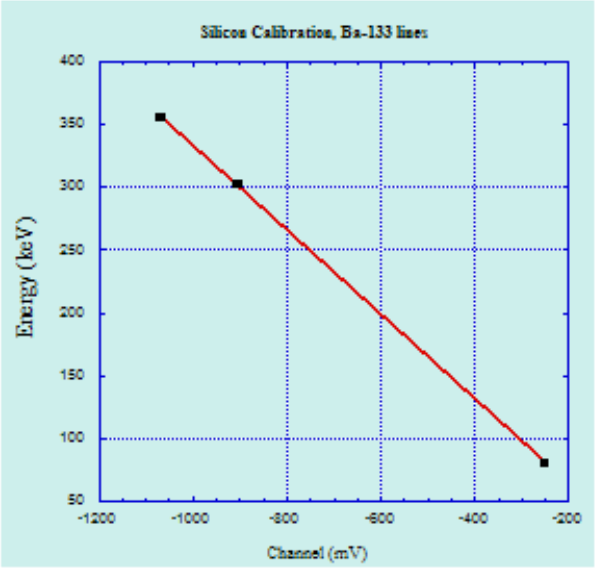

Figure 19 Energy calibration curve for single strip.

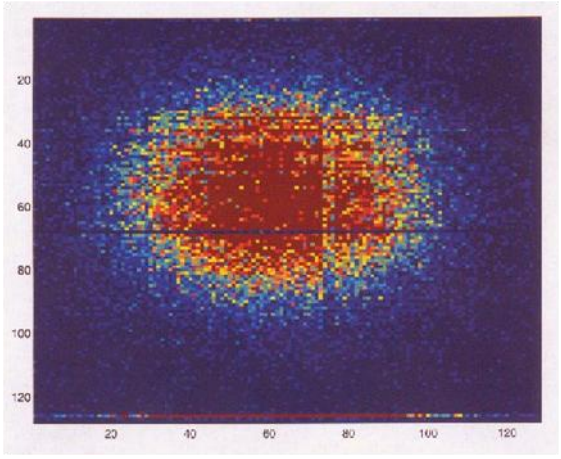

Figure 20 Self-triggered silicon detector hit image for ^{90}Sr electrons

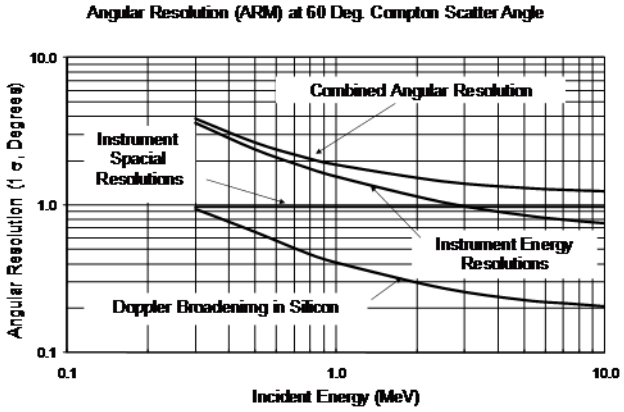

Figure 21 Angular resolution of the TIGRE prototype instrument including Doppler Broadening for 60º scatter angles in silicon

Chapter 5 Simulation for Compton events

After testing the components of the detector components, it is of great interest to know potential yield of Compton events. The expected number of Compton events is determined by n (counting rate), flux of atmospheric gamma-rays (f), effective area (A_{eff}), and observation time (t).

$$n = f \times A_{eff} \times t$$

Equation 15

The observation time used was approximately 5.1 hours (18,436 seconds). This time was chosen to match the flight situation (page 95). A_{eff} is determined by simulating gamma-rays upon a model of TIGRE. This was done using the Medium Energy Gamma-ray Astronomy Library (MEGAlib) (Zoglauer, 2006). MEGAlib allows users to create a model of TIGRE in the virtual medium, and thus simulate gamma-rays and high energy interaction in a controlled environment.

A. MEGALIB

MEGAlib is an open source Monte Carlo simulation package developed by the MEGA team in Germany as a tool to accurately predict the measurements and performance of their detector. MEGAlib uses GEANT3 as the main framework. GEANT3 and GEANT4 (Cosima) were developed by CERN as a toolkit to simulate high energy particle passage through matter using Monte Carlo simulations (Allison, et al., 2006). MEGAlib contains real physical processes of Compton interactions, such as Doppler broadening effects and generation of secondary particles in passive materials. It

allows customization of size, material and geometry of the mass model to be closer to that of TIGRE.

i. Geomega

In order to start the simulation, the simulating mass model has to be created. The Geomega package is included in the MEGAlib software for this purpose. For each component of the telescope, such as the silicon, CsI and NaI calorimeters, support structure, plastic scintillator and the outer pressure vessel, the material, atomic component, density, volume and shape were defined. The material, position and rotation of the component relative to the mother volume are also defined. Then the detector components are defined. For example, the silicon detector is defined as Strip2D. User defined energy thresholds can be chosen. Size and location of all passive material, such as air, aluminum honeycomb and the aluminum pressure vessel are defined to account for incomplete absorptions.

After completing this setup, a mass model that accurately describes the actual TIGRE telescope is created. This is shown in Figure 22, and a close up of the model of the multi layer detector is shown in Figure 23. The materials and dimensions of the mass model are given in Table 1.

Table 1 The following material make up the parts of TIGRE. These were arranged in MEGAlib for the simulation

*** - Printed Circuit Board**

Part	Material	Size	Mass (g)

Outer dome	Aluminum	Top and bottoms are half spheres with 87.0 cm radius. Connected with a 180.0 cm tall cylinder. Material is 0.2 cm thick	104,495.2
Mounting board for the Silicon detector	PCB*	35.0x35.0x0.03 cm An area of 20x20 cm is cut out from the center of this board to mount the silicon detector.	26.7
Silicon detector	Silicon	10.0x10.0x0.03 cm for each board. 16 boards in one tower, and four towers total = 64 boards.	447.4
Electronic readout	PCB	35.6x0.6x24.0 cm, on four sides outside the silicon towers, surrounding them.	2,460.7
Anticoincidence box (6 sides)	NE110 Scintillator	81.3x0.64x71.1 cm	28,631.5
Honeycomb support	Aluminum	109.2x109.2x2.0 cm Actual dimensions are	64,416.7

platform		109.22x109.22x7.5 cm, but since it is hollow inside, the vertical distance was reduced to 2 cm	
NaI calorimeter	NaI	Each bar is divided into five segments of 10.9x6.4x8.8 cm. Five of these are arranged length wise to make one bar. Eight of these bars are arranged widthwise. Total volume is 54.6x50.8x8.81 cm	89,737.7
Outer Al frame	Aluminum	Four posts at four corners, each dimension 6.0x6.0x200.0 cm	77,760.0
Inner frame	Aluminum	In four corners, each dimension 1.0x1.0x50 cm	540.0
NIM bins (Electronics modules below the Al honeycomb)	Aluminum	106.0x106.0x76.0 cm	2,305,627.2

ii. Cosima

A Cosmic Simulator for MEGAlib based on GEANT4 (Cosima), which is integrated with the MEGAlib package, is a universal simulator for low-to-medium energy gamma-ray telescopes. In the simulated environment, a model of a gamma-ray telescope is created to the user's necessary settings. Cosima simulates gamma-rays with specified energies onto the telescope mass model. These gamma-rays interact with the telescope model by means of photo-effect, Compton scattering, and pair creation, as it would in a real space environment. These simulation-triggered events are recorded on a "sim" file for further analysis, to be used with tools included in the MEGAlib package, which are described later. The exposure time of the simulated gamma-rays is user defined by the number of triggered events. The definition of a trigger is also user defined to match the real life telescope. For our usage, Cosima was set at 500 triggers for each simulation.

The mass model is read by Cosima as it simulates high energy particle interactions. Whenever the simulation gives a trigger Cosima stores the hit information in a file. The definition of a trigger is also customizable. For our purposes, a trigger is defined as at least one hit in the silicon as well as at least one hit in the calorimeter. The number of triggers is customizable, and Cosima will simulate high energy incident gamma-rays until the desired number of triggers is reached. Typically, 500 triggers were required for each trial run.

Cosima allows enormous flexibility for simulating photons. The energy spectrum and the incident beam can be customized. For our purposes, we have used monochromatic and negative power law for the energy spectrum, and homogeneous beam

and farfield area source for the beam parameters. A monochromatic, homogeneous beam simulates a simple and highly controllable environment. This is used to determine the effect of gamma-rays with different energies at different angles on the telescope. The power law spectrum from a farfield area source is used to simulate a realistic isotropic near space environment.

When defining an incident beam on Cosima, one must define the parameters of the "Surrounding Sphere". The Surrounding Sphere is a virtual sphere with a circular disk whose center is located tangential on the outer surface of the sphere. The concept of this is shown in Figure 24. The surface and center of the circular disk is always facing the center of the sphere. The center of the sphere is user defined, and it is usually set to the center of the detector. The size, or the radius, of the sphere is also user defined. When the radius is defined, the circular disk is automatically defined to have its center situated on the surface of the sphere. The size and location of the center of the disk along the surface of the sphere is user defined. The customized incident beam is originated from a random location on the circular disk, and the angle of the incident beam is also user defined. Therefore, it is also necessary to define the disk size and beam angle to cover the entire detector, including the outer housing. Sketches of incident beams at angles are shown in Figure 25 and Figure 26.

For our purposes, three types of simulations were made. First, a monochromatic homogeneous beam was simulated on the mass model to find the energy and angle dependency of TIGRE's detection efficiency. Next, the homogeneous beam was repeated with a power law energy spectrum. This simulated a discrete celestial source of

gamma-rays. Thirdly, an isotropic power law source was simulated. This simulated the atmospheric background at balloon altitudes. In this setup, the disk is situated on a random location on the sphere for each simulated gamma-rays (Figure 27). The simulation of the power law spectrum takes the form of $I(E) \propto E^{-\alpha} \ \forall E \in [E_{\min}, E_{\max}]$. The customizable parameters are α, E_{min}, and E_{max}.

iii. Revan

The information of the 500 triggered events as well as the number of trial events was stored in a "sim file". An event is stored as long as it triggers the detector, no matter the type of interaction. Each event in the sim file has a unique event ID, energy of the incident simulated gamma-ray and time of interaction. The x, y, z location of each interactions with the telescope model is recorded along with its type of interaction (Compton, Pair, Bremsstrahlung, etc.). If the nature of the particle changed after the interaction, it is recorded with the kinetic energy of the new particle. This file is read by the Real Event Analyzer (Revan) that can be tailored to user specifications, and the desired event reconstruction is performed. It reads the output file from Cosima combining it with the mass model defined earlier, and gives detailed results on the desired events that occurred within the 500 triggers that Cosima generated.

First Revan looks for clustered hits in a single detector and combines them by calculating the energy-based center of gravity. This is for hits which occurred across multiple silicon strips. Secondly, Revan screens for pair events by looking for the

signature “inverted V” structure in the silicon hit sequence. Third, high energy charged particles such as muons are screened. These are recognized by a straight line through many layers of silicon. Last, Compton events are reconstructed. The Compton sequences are recognized by short curved paths through the silicon layers. The recoiled electron will deviate from the original path as it loses momentum, and sometimes it can scatter back at the end of the track. Therefore, numerous options are included as methods for determining the correct tracking sequence including Pearson Correlation and Bayesian electron tracking. For our purposes, we have selected the Pearson Correlation method.

Revan allows the user to choose reconstructing Compton events with or without electron tracks. Events without electron tracks refer to the situation where there was at least one interaction in the silicon layers in coincidence with at least one interaction in the Calorimeter. This is identical to Compton events detected in classical Compton telescopes. On the other hand, events with electron tracks refer to multiple signal hits in the silicon layers in coincidence with one interaction in the Calorimeter.

Revan also takes into account of the thresholds defined in the setup files. For each detector, a noise (i.e., trigger level fluctuation) and trigger threshold can be customized in the setup file. If the energy of the incident gamma-ray simulated in Cosima is lower than the energy threshold defined in Revan, this event will be ignored eventually, leading to fewer detected Compton events.

B. Efficiency of TIGRE

Knowing the potential detection efficiency of the prototype TIGRE instrument is of great interest for developing a full-scale telescope. For our purposes it is needed to convert incident fluxes into counting rates. With the first simulation, beams of gamma-rays with fixed energy were incident on the mass model with a fixed location for the disk on the surrounding sphere. This was repeated for different energies. Then the position of the disk on the surrounding sphere was modified to be set at a new angle and the simulation was repeated. The center of the surrounding sphere was positioned to be at the center and base of the eight NaI bars with a 200 cm radius. The circular disk was positioned 200 cm directly above the detector. The radius of the disk was set to 90 cm and the homogeneous beam was set to move directly downward. In this way, a monochromatic beam is positioned to interact with the entire detector (Figure 25). The number of triggers was set to 500, and the total number of incident gamma-rays needed to achieve this number of triggers was recorded. This was repeated for the energies of 0.3, 0.5, 0.8, 1, 2, 5, 10 and 50 MeV.

Next, the position of the disk was move at selected angles away from the zenith to simulate incident gamma-rays entering at different angles away from the zenith. The radius of the surrounding sphere was kept at 200 cm. Since the setup is done in Cartesian coordinates, the corresponding x, y, z coordinates for each angles were calculated and the center of the disk was set to that location. The beam direction was set to be orthogonal to the disk surface (Figure 26) so that it is incident directly on the detector. Precaution was taken at larger angles to take into account of the increased projected size of the detector.

The angles chosen were θ = 0, 15, 45, and 60 degrees from the main axis of the telescope. Since the projected area of the detector increases as the angle increases, the radius of the disk was increased to 90 cm, 95 cm, 100 cm, 120 cm, and 150 cm respectively.

To calculate the efficiency, the number of Compton events found was recorded for each simulation. By determining the number of reconstructed Compton events found from the 500 events with Revan, the effective area of the TIGRE telescope can be calculated. The effective area is found by

$$A_{eff} = \eta A_{\det} = A_{beam} \frac{N_{Compton}}{N_{tries}}$$

Equation 16

where η is the absolute efficiency of the telescope, A_{det} is the area of the detector, A_{beam} is the area of the incident beam (i.e., disk area), $N_{Compton}$ is the number of Compton events that Revan finds, and N_{tries} is the total number of simulated gamma-rays that Cosima needed to achieve 500 triggers.

The area of the detector is the projected surface area of the silicon converter/tracker array that the incident beam sees at any given time. The disk on the surrounding sphere was initially set directly above the detector. From above, the detector area is defined by the 2x2 array of 10 cm square silicon strip detectors or 400 cm^2. When the disk of the surrounding sphere is tilted at an angle, the disk will view a projection of the top part of the silicon arrays, added to a projection of the side of the array in view (Figure 28). The orientation was defined such that there is only one side of the detector visible. i.e., the corners and adjacent side of the detector are not. Therefore, the area of the detector for incident beams at an angle is,

$$A_{det} = A_{top}\cos(\theta) + A_{side}\sin(\theta)$$

where A_{top} is 400 cm^2 and A_{side} is 427 cm^2, and θ is the angle of the tilt.

Simulations of a monochromatic beam incident on the mass model were made for all the angles and energies described in page 61. Revan was used to find Compton events for all simulation. Equation 16 was used to calculate the efficiency for each incident angle simulated with different incident energies, summarized in Table 2.

Table 2 Telescope efficiencies at different energies in percent. Each angle represents the deviation from the zenith of the telescope.

Angles / Energies	0°	15°	30°	45°	60°
0.3 MeV	0.23±0.05	0.14±0.03	0.13±0.03	0.12±0.03	0.09±0.02
0.5 MeV	0.68±0.08	0.45±0.06	0.51±0.06	0.27±0.04	0.24±0.04
0.8 MeV	0.62±0.07	0.63±0.06	0.46±0.05	0.54±0.06	0.28±0.04
1 MeV	0.76±0.08	0.57±0.06	0.57±0.06	0.53±0.05	0.45±0.05
2 MeV	0.82±0.09	0.63±0.06	0.53±0.06	0.44±0.05	0.55±0.05
5 MeV	0.87±0.11	0.78±0.10	0.59±0.08	0.55±0.07	0.55±0.07
10 MeV	0.75±0.12	0.59±0.11	0.55±0.09	0.58±0.09	0.76±0.11
50 MeV	0.48±0.12	0.35±0.10	0.31±0.09	0.32±0.09	0.45±0.12

A plot to visualize TIGRE's angle dependence for efficiency is shown in Figure 29. A decrease in efficiency can be seen as the incident beam deviates from the zenith of detector. The maximum efficiencies occurred at approximately 5 MeV for all angles. These are given in Table 3. The errors are statistical 1-σ errors due to the limited number of successful triggers.

Table 3 Absolute efficiency at 5MeV

Angle (º)	Maximum Efficiency (percent)
0	0.87 ± 0.11
30	0.59 ± 0.08
45	0.55 ± 0.07
60	0.55 ± 0.07

Revan allows the user to control the energy threshold values of the silicon layers and the NaI detectors. Its effect on TIGRE's efficiency was analyzed. First the thresholds were set the same way TIGRE had for its analysis, with 80 keV for silicon and 700 keV for the NaI calorimeter. Then the Calorimeter threshold was decreased to the ideal value of 200 keV to find the potential Compton yield. Thirdly, the threshold for the silicon was increased to 200 keV with the Calorimeter also back to 700 keV. Figure 30 shows that the overall efficiency of the detector decreases with increasing threshold as expected. The number of Compton event found is halved when the NaI threshold is increased from 200 keV to 700 keV.

The second simulation was of the power law energy source at a fixed point. This was done to find TIGRE's potential counting rate of gamma-rays originating from a source. The disk of the surrounding sphere was returned to the position 200 cm directly above the mass model. The parameters available for Cosima for the power law simulation are described in page 59. The power law was set with a E^{-2} spectrum, from 0.78 MeV to 30.0 MeV, and the trigger limit was again set to 500. The counting rate was determined from Equation 15 with Equation 16 for A_{eff}. The Crab Nebula was used for

the source of gamma-rays. Its flux in the 0.78-30.0 MeV range is 1.85×10^{-3} gamma/cm^2 * sec (van der Meulen, et al., 1998). Revan returned 55 Compton events from 130,988 total tries. A_{beam} is π*(90 cm)^2 = 25,446.9 cm^2, and A_{eff} is 2.17 cm^2. The observation time was taken to be the portion of TIGRE's flight time when it was operating in the tracked mode, which was 18,436 seconds. The number of expected Compton events obtained this way was 74 gammas.

To determine the expected number of gamma-rays from the atmospheric background, it is necessary to determine the flux of the atmospheric gamma-ray. Peterson, Schwartz, & Ling (1973) conducted a detailed study of the gamma-ray flux at the balloon flight altitude for the low gamma energy range. Here, the omnidirectional counting rate per MeV was determined with a standard 3"x3" NaI scintillator. Assuming a detection efficiency of 100% for the NaI detector, this gives a lower limit to the flux of gamma-rays from the atmosphere. The power law slope, α, was derived from figure 12 in (Peterson, Schwartz, & Ling, 1973) (Figure 31). From this figure, one can deduce the following for the single power law approximately representing the measurements.

Table 4 significant points of atmospheric flux

Energy (MeV)	counts/cm^2 sec MeV
0.1	15
1	0.4
100	8e-4

Since $\text{counts}/\text{cm}^2$ sec MeV = $\beta E^{-\alpha}$, using two points from the table above one may solve for the necessary constants. They were found to be α = 1.42 and β = 0.4 counts/cm^2 sec

MeV. Using $Flux = \int_{E_1}^{E_2} \beta E^{-\alpha}$, the flux for the energy range 1.0-10.0 MeV is 0.588 gamma/cm^2 * sec. These are approximately the minimum and maximum energies from the TIGRE flight data (ref p112). To find A_{eff}, Cosima was set for an isotropic radiation with a power law spectrum. The environment and conditions were set to match those of the actual flight conditions. E_{min}, and E_{max} were set to be from 1.0 MeV to 10.0 MeV. The radius of the surrounding sphere was 150 cm. Revan found 62 Compton events from the 2,415,457 total tries. Using Equation 16, A_{eff} was 2.22 cm^2. Putting this effective area in Equation 15, the expected total number of Compton events was 24,102, or 1.31 events/second. The expected efficiency of the telescope from Equation 16 with A_{det} = 400 cm2 is 0.56%. This assumes that all the gamma-rays interact in the silicon array first.

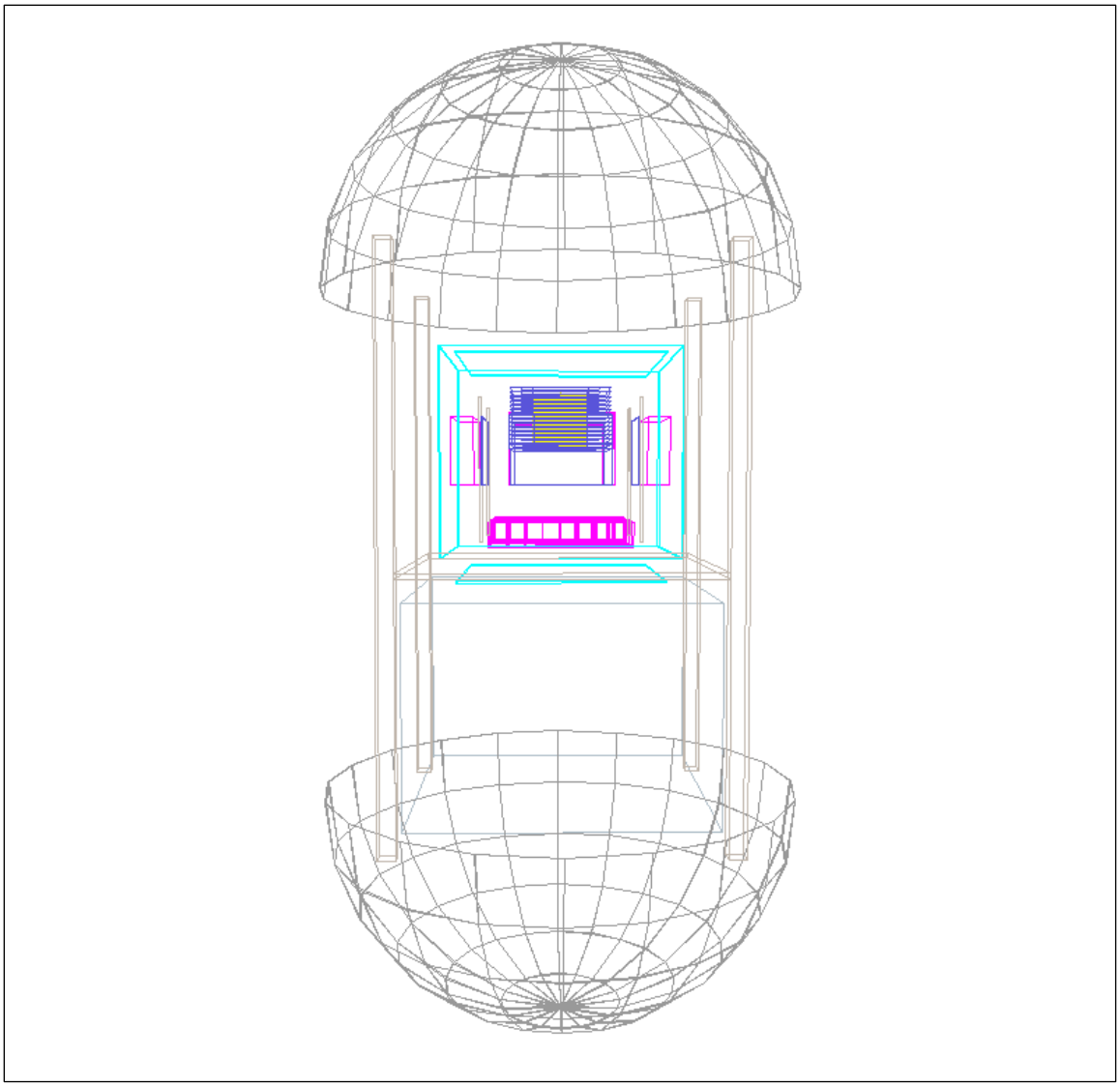

Figure 22 The mass model for TIGRE generated using MEGAlib.

The dimensions and composition of all passive and impassive objects are identified.

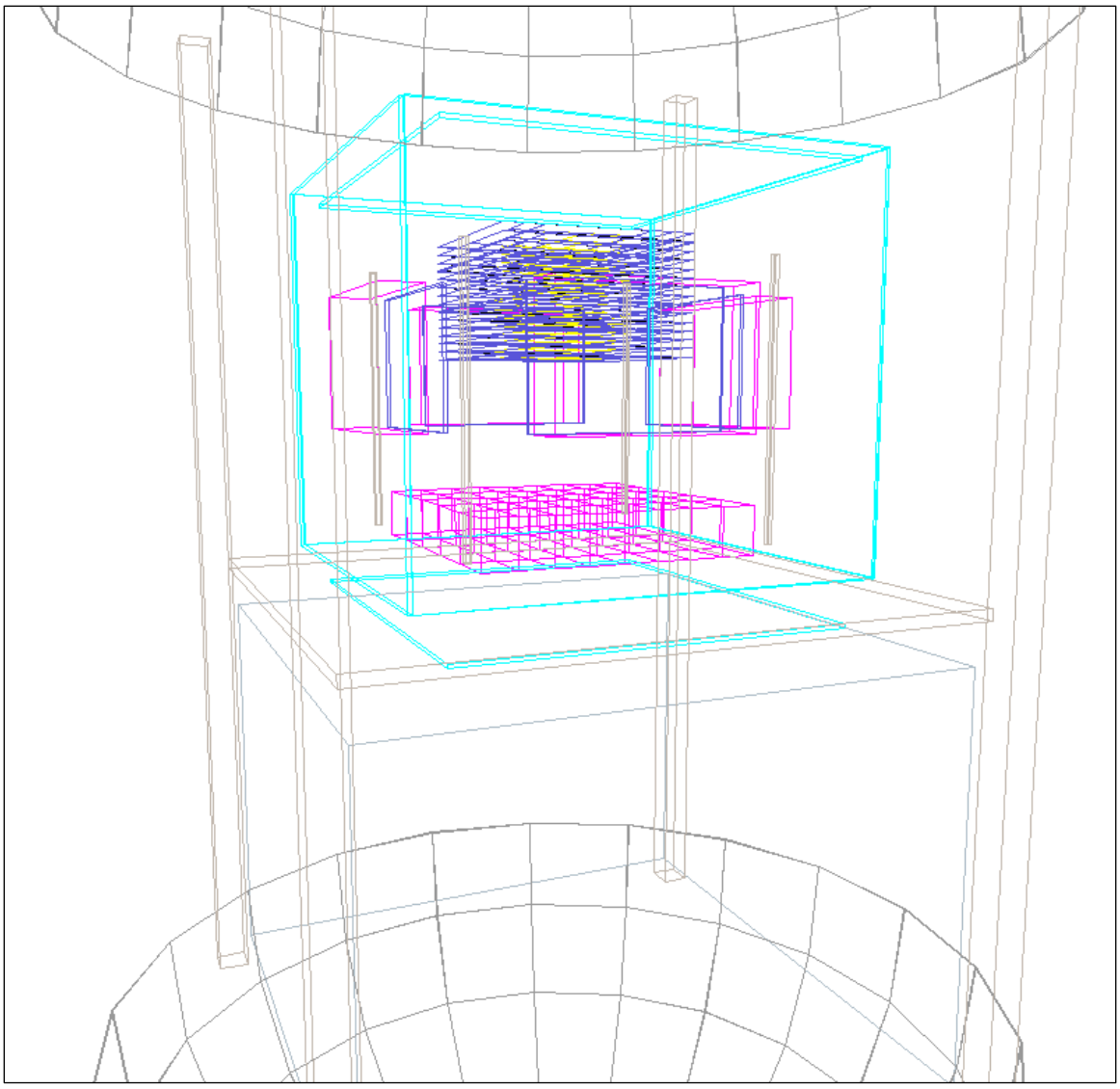

Figure 23 A close up of the electron tracker.

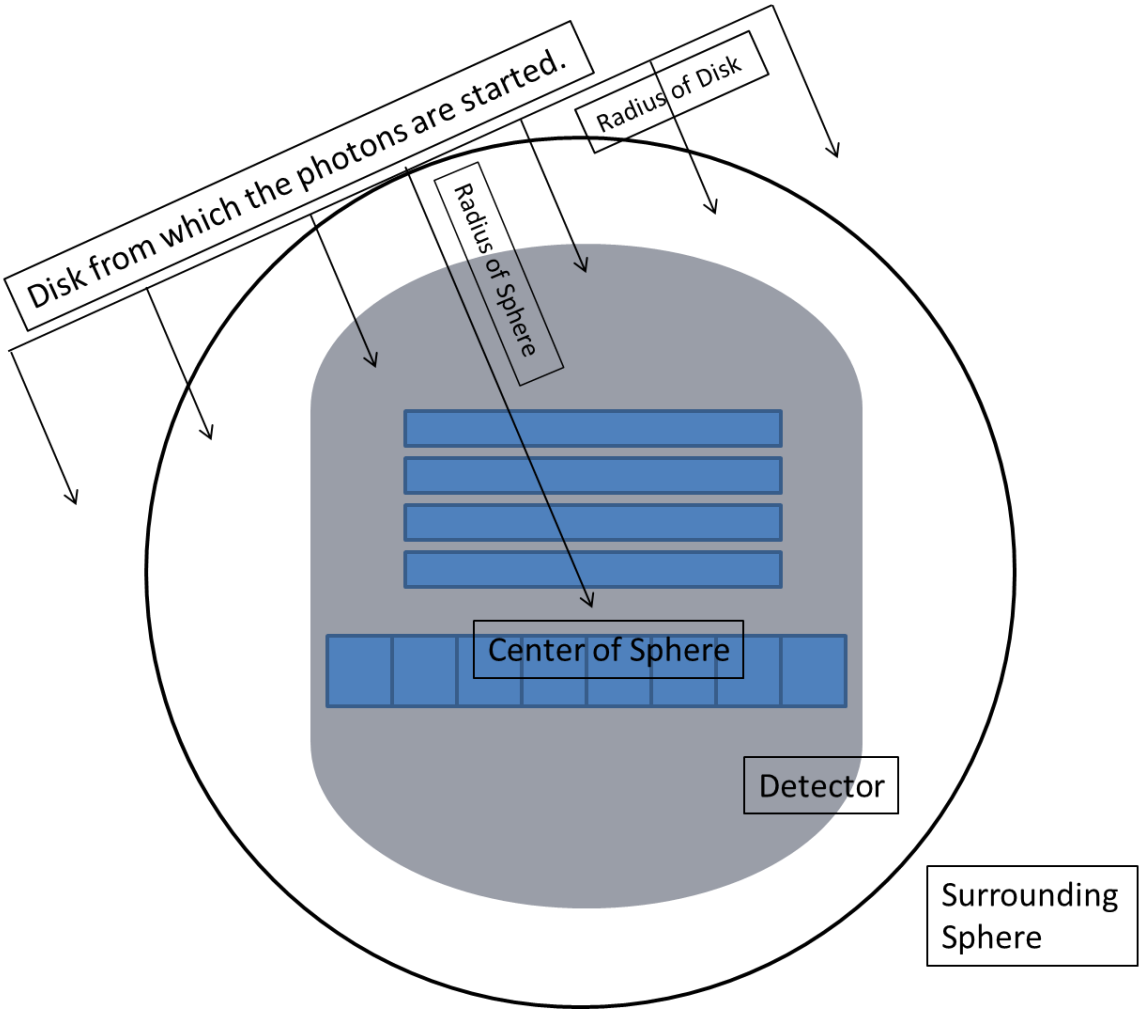

Figure 24 The Surrounding Sphere. The simulated gamma-rays are all originated from somewhere on the disk. The direction of the gamma-ray, the radius of the disk and the radius of the sphere are customized.

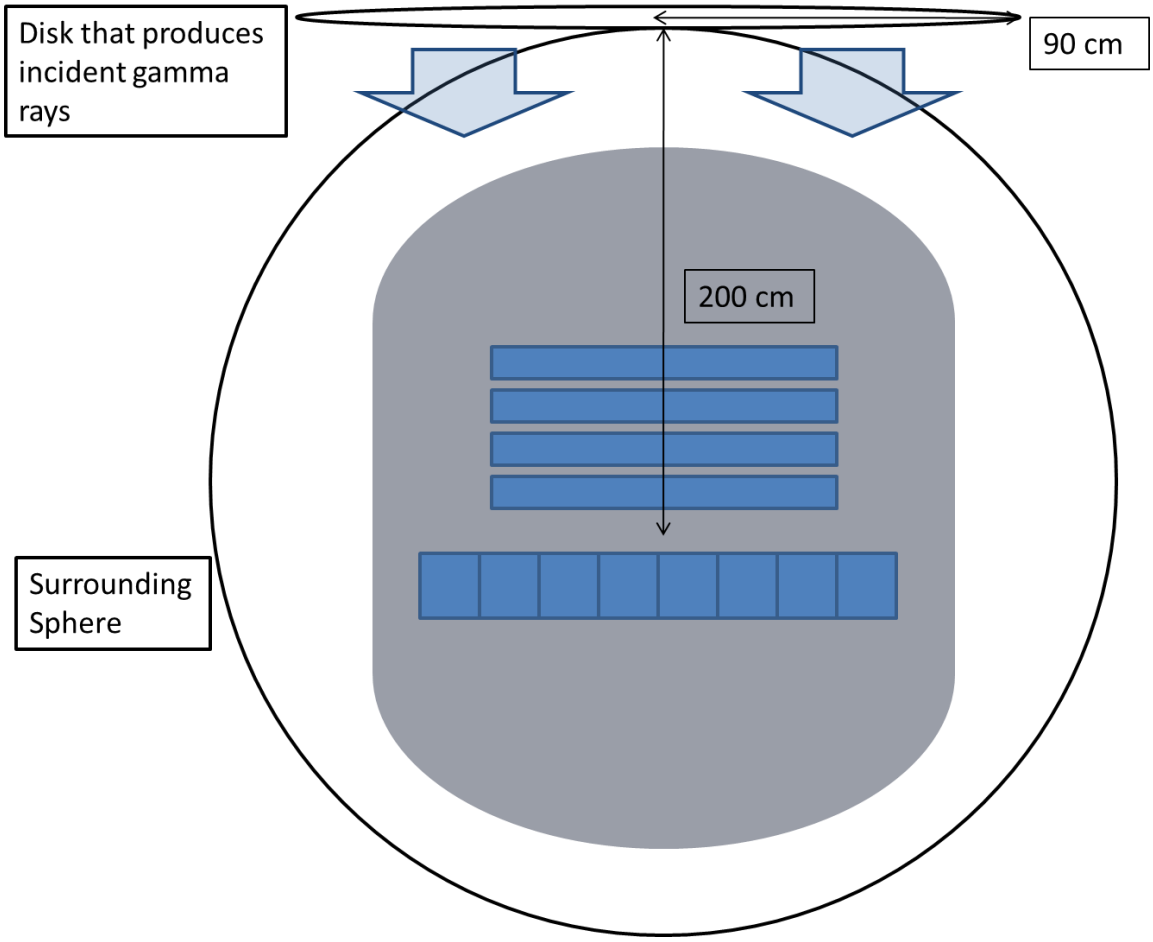

Figure 25 Surrounding Sphere setup for monochromatic photons incident directly above the detector.

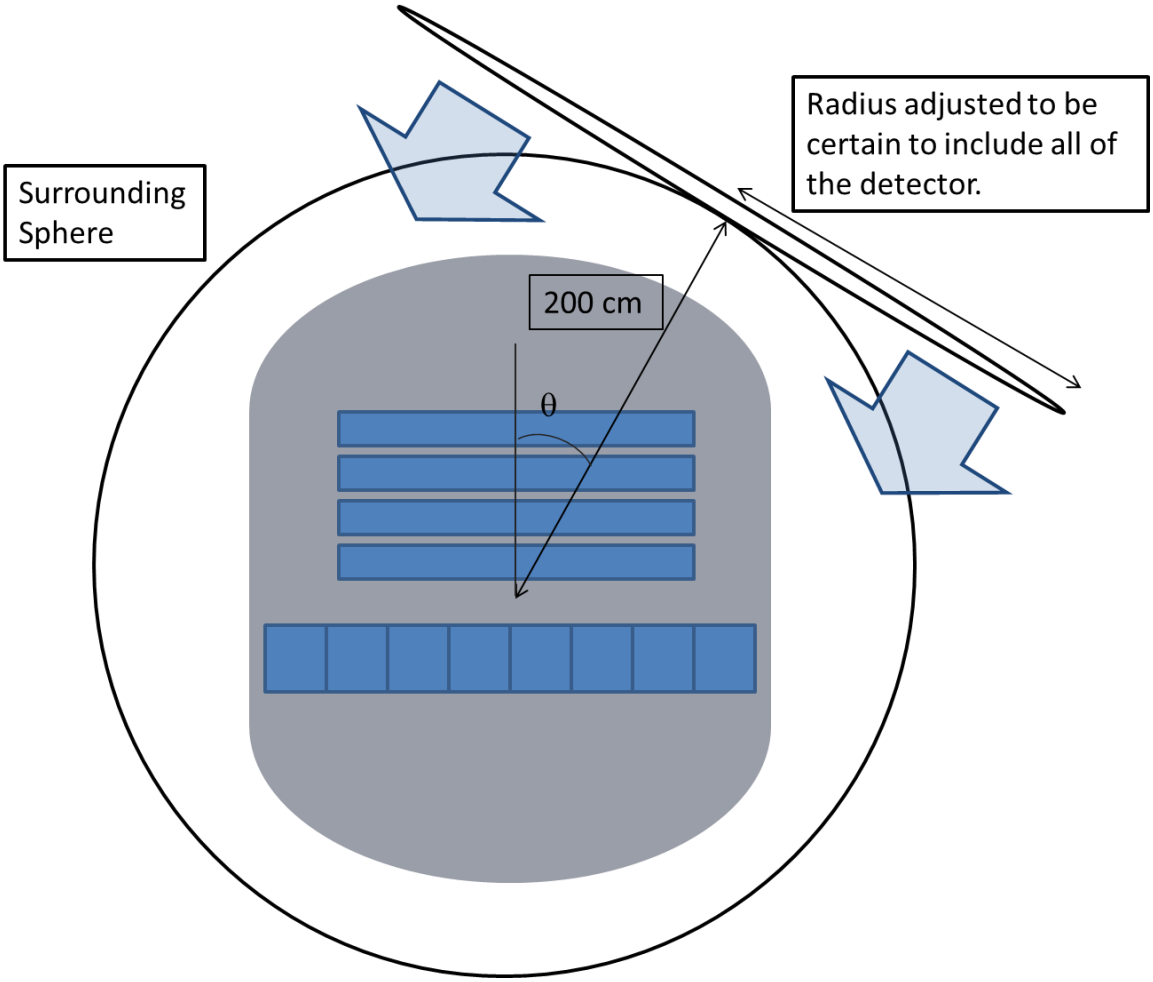

Figure 26 Monochromatic gamma-ray incident at an angle.

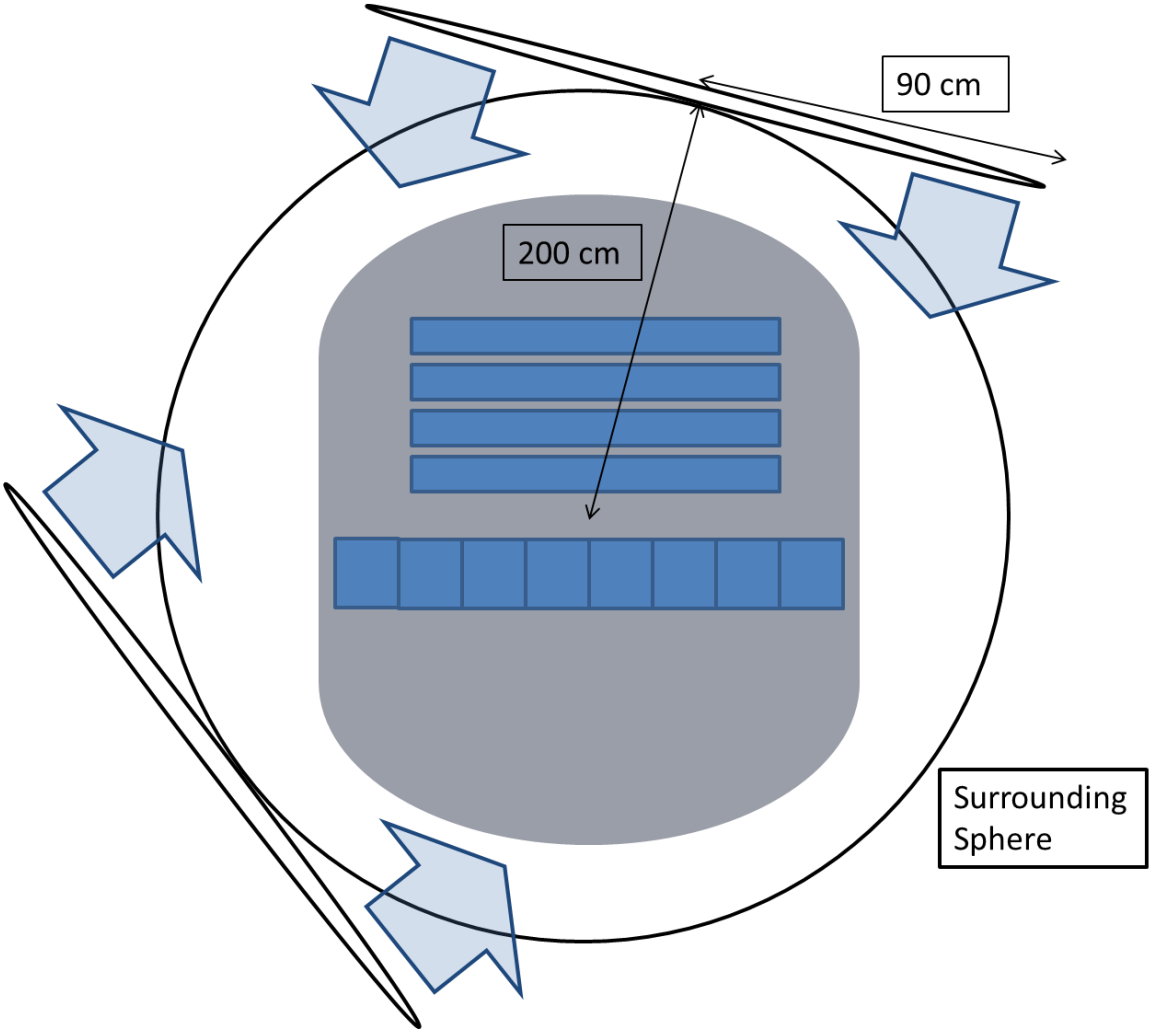

Figure 27 Surrounding sphere for simulating isotropic radiation. Each time the gamma-ray is emitted, it originates from the disk, whose center is on a random position on the sphere.

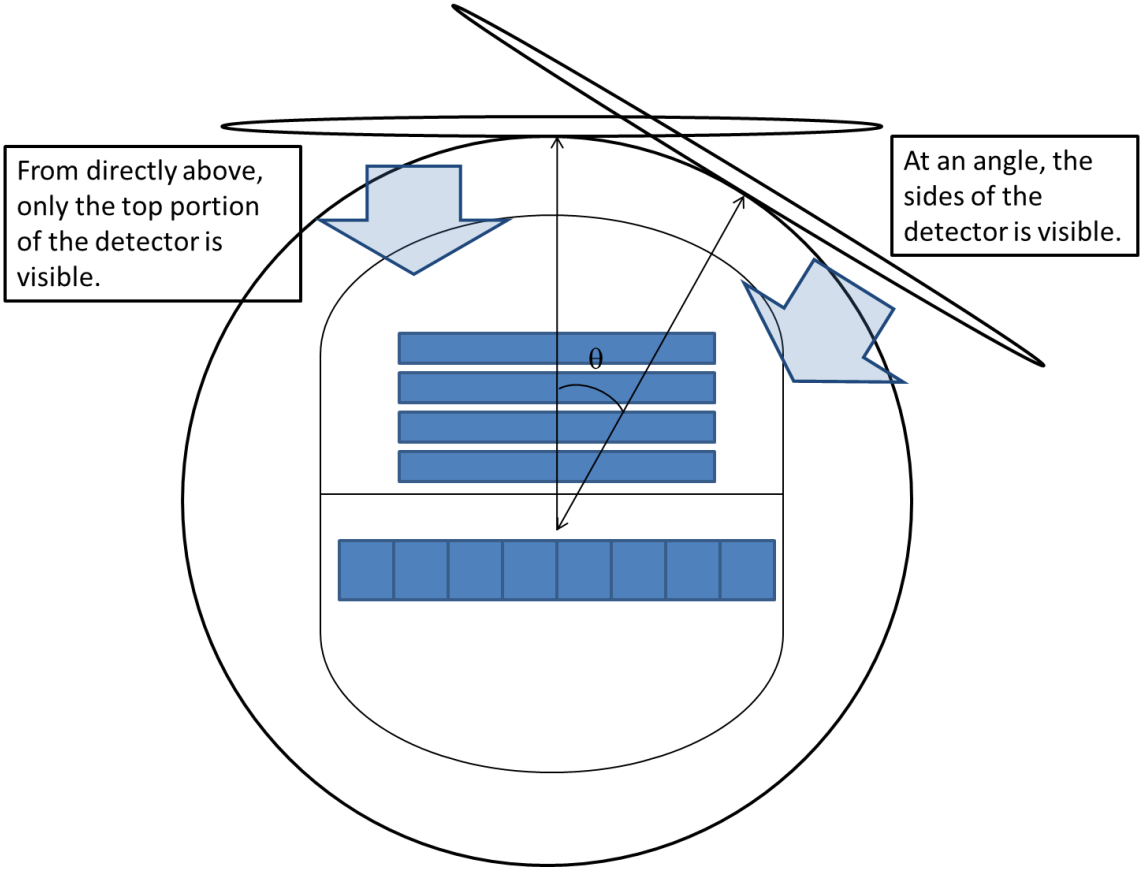

Figure 28 The visible area of the detector is dependent on the defined angle.

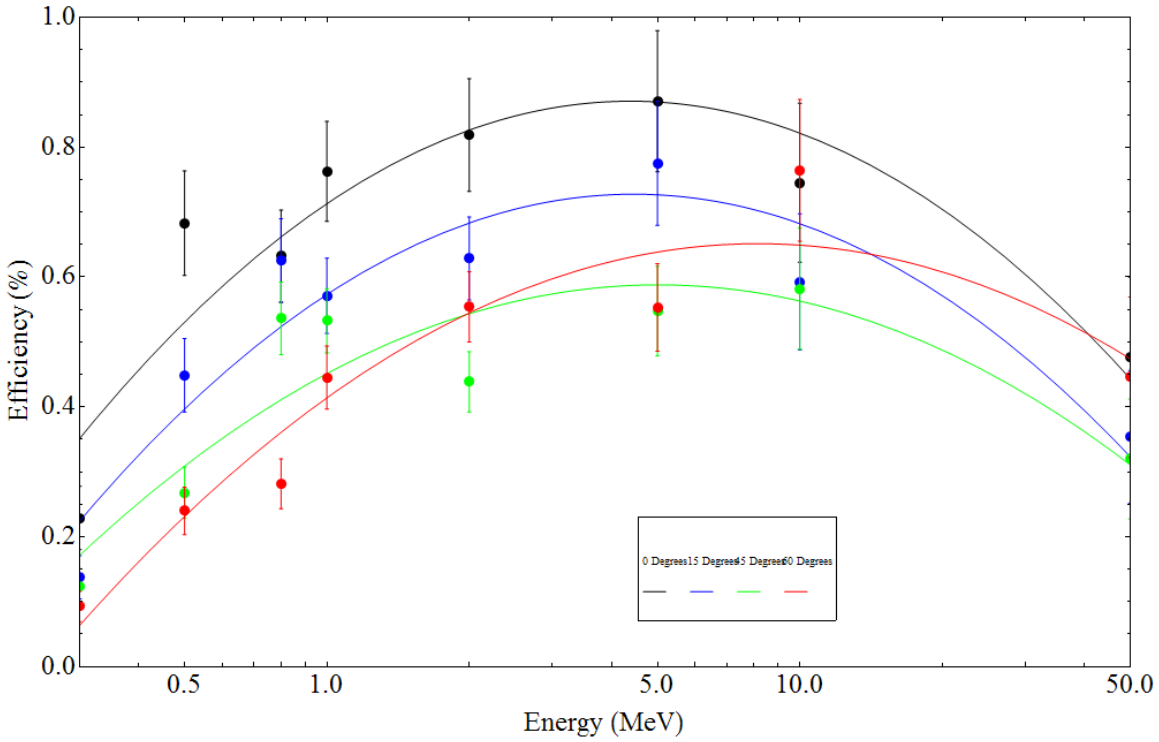

Figure 29 Simulation of a monochromatic incident gamma-ray beam using MEGAlib shows that increasing the incident angle (measured from the zenith) of the incident photons decreases the overall efficiency of the telescope. From the top, 0 degrees, 15 degrees, 45 degrees and 60 degrees. The threshold of the NaI bars were set at 700 keV and the Si threshold at 50 keV.

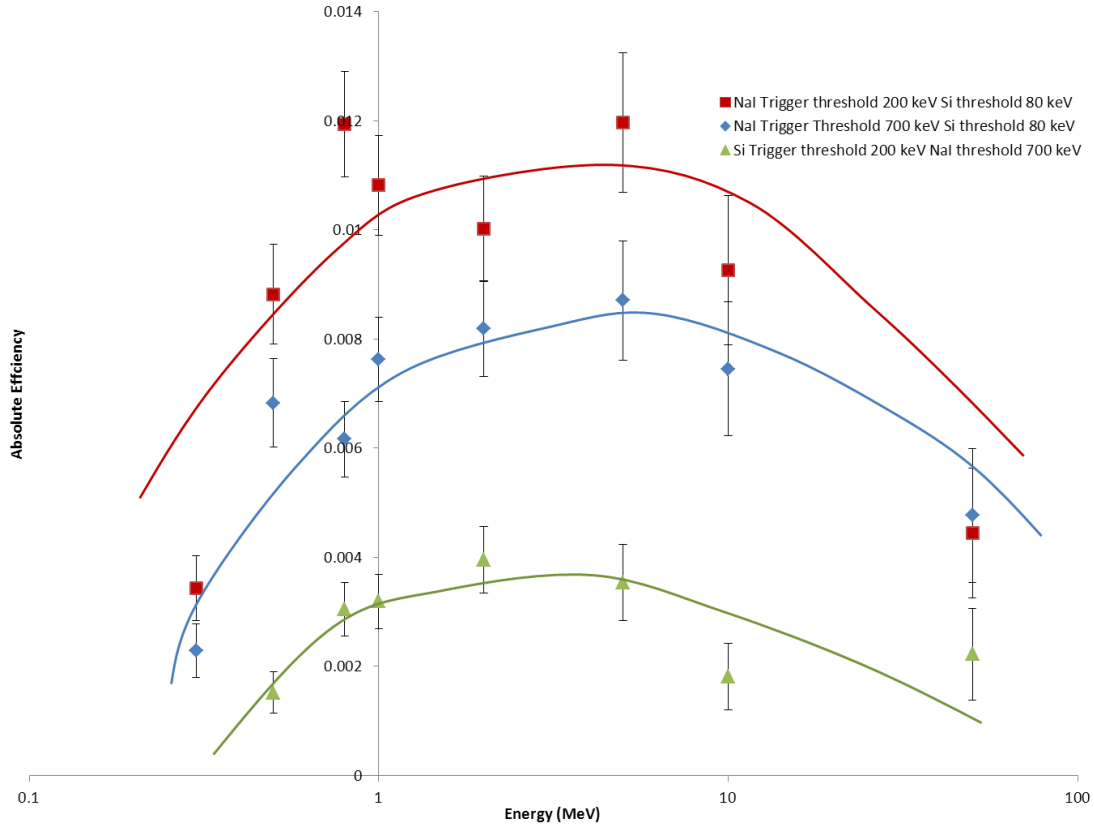

Figure 30 The Compton events yield decreases as the threshold of the detectors increases. Red: NaI bars at 200 keV and Si boards at 80 keV threshold. Blue: NaI bars at 700 keV and Si boards at 80 keV. Green: NaI bars at 700 keV and Si boards at 200 keV. The incident angles were at 0°.

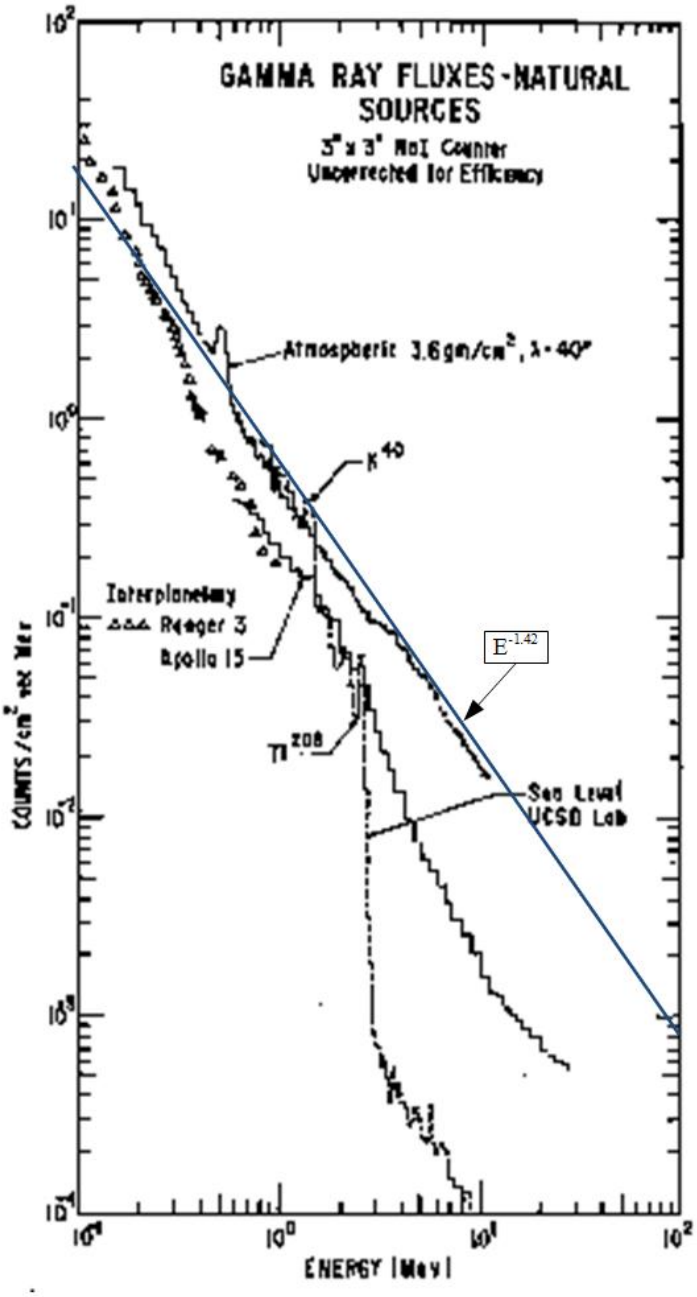

Figure 31 Chart of atmospheric Gamma ray flux used from Peterson et. Al.

Chapter 6 Flight Preparation

After its construction, TIGRE had to be calibrated for accurate detection and analysis. Once the telescope was moved to the launch site in Ft. Sumner, NM, further checks and preparation had to be conducted. This chapter will discuss them in detail. The UC Riverside team included A. D. Zych, T. J. O'Neill, D. Bhattacharya, E. J. Harris (computer specialist), and graduate students Kaoru Kamiya, the writer, and Charity H. Trojanowski.

A. NaI calibration

This section describes the detailed calibration of the NaI detectors in preparation for the first balloon flight with the TIGRE prototype instrument. The procedure was also repeated at the launch site. When the scattered photon interacts with any one of the bars, the signals are read from both ends of the long side of the bars, which are labeled A and B. These signals are added to determine the energy of the scattered photon. In order to do this, the signals must be converted to the appropriate units. The radiation detection is position sensitive along bar, so we must first determine where along the bar the scattered photon hit, and then the signals must be corrected to MeV.

A collimated ^{88}Y source was placed underneath each bar at 2 inch intervals from 8 inches to 32 inches from the end of the 40 inch bar. The 8 inch sections of each bar nearest to the PMTs were excluded from the telescope's sensitive volume. The source was placed for a few minutes as the radiation information was collected. Then the source was moved 2 inches, and the information was collected again. For each bar position, the

sum of both ends of signals ($A+B$) and the difference over the sum $\left(\frac{A-B}{A+B}\right)$ was calculated. The gains of the two PMTs were adjusted so that (A-B) was zero at the center position (20 in.). Histograms of the signal summation were generated for all the positions that the source was placed. Two examples of these histograms are in Figure 32 and Figure 33. Both histograms show two clear photopeaks, corresponding to the 0.900 MeV and the 1.836 MeV energies of the ^{88}Y. Using Gaussian fits to the photopeaks, the pulse height value of the peaks were estimated. These peak signals were plotted against the position of the NaI bar in inches to show the variation of the peak signal along bar in Figure 36 of the peak signal vs. position plot from the $A+B$ plot are two concave lines, each corresponding to one of the energy values. Histograms were also created for $\left(\frac{A-B}{A+B}\right)$, also for all positions. These values lie between -1 and 1. Two examples of these are shown in Figure 34 and Figure 35.

For the histogram for $\left(\frac{A-B}{A+B}\right)$, it can be seen that there is a dominant peak as the source was moved along the bar. This is attributed to the fact that the PMT closer to the source will receive a larger signal. Only the dominant 1.8 MeV peak was taken. At the 20 inch position, two peaks are seen due to the attenuation at the crystal interface discontinuity. When plotted as a function of position, the result can be approximated as two linear curves with a discontinuity at the 20 inch position (Figure 37). Using an inverse linear fit for both upper and lower lines, the equation to determine the position (x) is

$$\left(\frac{A-B}{A+B}\right) = \text{slope} \times x + \text{intercept}$$

Each event $\left(\frac{A-B}{A+B}\right)$ gives the position along the bar that the interaction occurred.

The $A+B$ summed pulse height plot is fitted with a quadratic equation.

$$(A+B)_{peak} = a \times x^2 + b \times x + c$$

where a, b, and c are constants determined from the fit and x is the position along the NaI bar. The positions determined from the previous step are inserted back to the quadratic equation, which give a theoretical value of A+B. These values were divided by the value at the 20 inch position to give a factor for each event to normalize pulse heights to the central position.

$$Factor = \frac{(A+B)_{theoretical}}{(A+B)_{20inches}}$$

These normalizing factors were applied to the corresponding experimental $A+B$ values, and now that all the values are normalized to 20 inches, an overall histogram can be created again, this time combining the data from all positions along the bar (Figure 38). This plot is fitted again to determine the peak positions. Since these two peaks correspond to the two gamma-ray energies of ^{88}Y, a plot with these two points is created. From the straight line passing the two peaks, the signals are now converted to MeV (Figure 39). Energy spectrum created using the appropriate energy units is shown in Figure 40.

B. Flight Preparation in Ft. Sumner

On April 7, 2007, TIGRE was secured in a large 24' van and was driven to Ft. Sumner, NM. This was where NASA's Columbia Scientific Balloon Facility (CSBF) held its "turn-a-round" launches for their spring 2007 operation. CSBF (previously known as the National Scientific Balloon Facility) was established in 1961 in Boulder, Colorado. Now based in Palestine Texas, they conduct the launching of scientific research equipment into the stratosphere around the world. CSBF use large helium balloons for launching the equipment into the atmospheric to altitudes of 130,000 feet. In 1988, NASA chose Fort Sumner Municipal Airport as a permanent launching site since other locations such as Palestine or Houston, TX became more populated and had less desirable wind conditions.

The balloons are made of polyethylene film and 0.002 cm thick. They can carry a payload of 3,600 kg and can stay afloat for up to two weeks. The balloons are partially filled with helium when launched. The low pressure in the stratosphere expands the balloon to its full size. The payload will reach its float altitude in approximately two to three hours from launch. Longer flights can occur during the "turnaround" time, when the float winds are light and variable. This occurs during the spring and fall, and it is advantages to have the balloon experiments during these times, or the payload will drift too far.

When preparing the TIGRE instrument for the launch, numerous calibrations had to be repeated. The NaI bars had to be recalibrated at Ft. Sumner due to some changes made to the readout system. All calculations and fits were repeated. A special reflective

aluminum tape was cut in strips for the detector. They were measured and arranged to cover the entire top surface of the detector dome. This tape was designed to have the best balance of deflecting the sunlight while radiating heat from within the detector casing.

Thick fiberglass insulations were measure and cut to fit around and underneath the pressure vessel of the detector. The pieces were taken outside to paint with a white reflective paint. This was a specially chosen paint graded by NASA which is designed to most effectively reflect sunlight. This insulation was placed on the side of the detector. Another piece was cut out to place on the bottom of the detector and was painted.

Lithium primary battery packs to power the telescope while afloat were supplied by CSBF. However, the battery containers for them had to be constructed at Ft. Sumner. Aluminum frames were used for the structure of the containers. Plywood and Styrofoam were measured and cut to fit as walls for these containers. The corresponding Styrofoam pieces were glued to the plywood and inserted in the containers as walls with insulators. Three of these battery boxes were constructed and painted. With the batteries inserted, the detector, combined with all materials that would be with it at launch, were weighed by the CSBF crew. This determined the amount of ballast required, which would be used to control the height of the telescope from ground.

The azimuthal orientation of the telescope is determined with x- and y-axis Hall Effect magnetometer probes that sense the horizontal components of the earth's magnetic field. This is needed to determine the orientation of the payload and the gamma-ray incident directions on the celestial sky. The probes, aligned along the telescope's x- and y-coordinate axes, were calibrated at known angles with respect to magnetic north with

the telescope suspended in an area where the earth's field is uniform (i.e., away from steel structures, etc.). At Ft. Sumner, NM, the magnetic declination was 8° 32' E. A central point was chosen beneath the suspension point of the telescope, and the angle between the true north and magnetic north was noted. Starting from the magnetic north and the center, marks were laid out at 10 degrees intervals. The detector was moved to this location, and the center of the telescope was aligned with the chosen center. The magnetometer readings were taken at every 10 degree marks. After returning from New Mexico, this information was processed to convert from detector coordinates to celestial coordinates. Figure 41 shows a graph of the x-y values normalized to maximum values of ±1 for a 360^{o} rotation. Also shown are the x-y points for a perfect circle, using the angle that the telescope's x-axis (and x-probe) makes with magnetic north. The variable offset of these two sets of data points, which can be as large as 4°, is due to unavoidable magnetic materials included in the construction of the telescope such as magnetic shielding for the photomultiplier tubes. To compensate for this offset a 6^{th} degree polynomial fit to the difference between the correct angle and the azimuthal angle found from $\theta = \tan^{-1}\left(y/x\right)$ is used as a correction. In this way the normalized magnetometer readings with each event are used to find the orientation of the telescope to an accuracy of ±0.5°.

The telemetry system, the consolidated instrument package (CIP), was attached to the telescope platform for testing. This was provided by CSBF as a mean to send commands and receive telemetry with the detector during flight. The ground station

command system allows up to 77 discreet commands and a 16-bit data word command. The telemetry from the payload used the Pulse Code Modulation (PCM) method with a 50 kHz NRZ (non-return-to-zero) format. Due to unpredictable stratospheric wind, there is a possibility that the payload drifts far enough to be unable to be reached by line-of-sight telemetry. For such an event, a down range station is arranged by CSBF in Holbrook, AZ. They are equipped with all electronics necessary to communicate with the telescope. It can be accessed by driving or by the tracking aircraft operated by CSBF.

C. ^{88}Y and ^{90}Sr Calibration

Just prior to the balloon flight in New Mexico, a calibration run was conducted with a ^{90}Sr positioned underneath the dome casing. Another calibration was carried out with an ^{88}Y source positioned at a fixed point. A telescope run was conducted by placing an ^{88}Y source directly above the aluminum dome casing of the telescope. TIGRE detected its gamma-ray radiation as it would during the flight. The source was positioned at x = 33.19 cm, y = 33.19 cm, and z = 129.70 cm in detector coordinates. Their results were used in post flight analysis, described in page 102 and page 137.

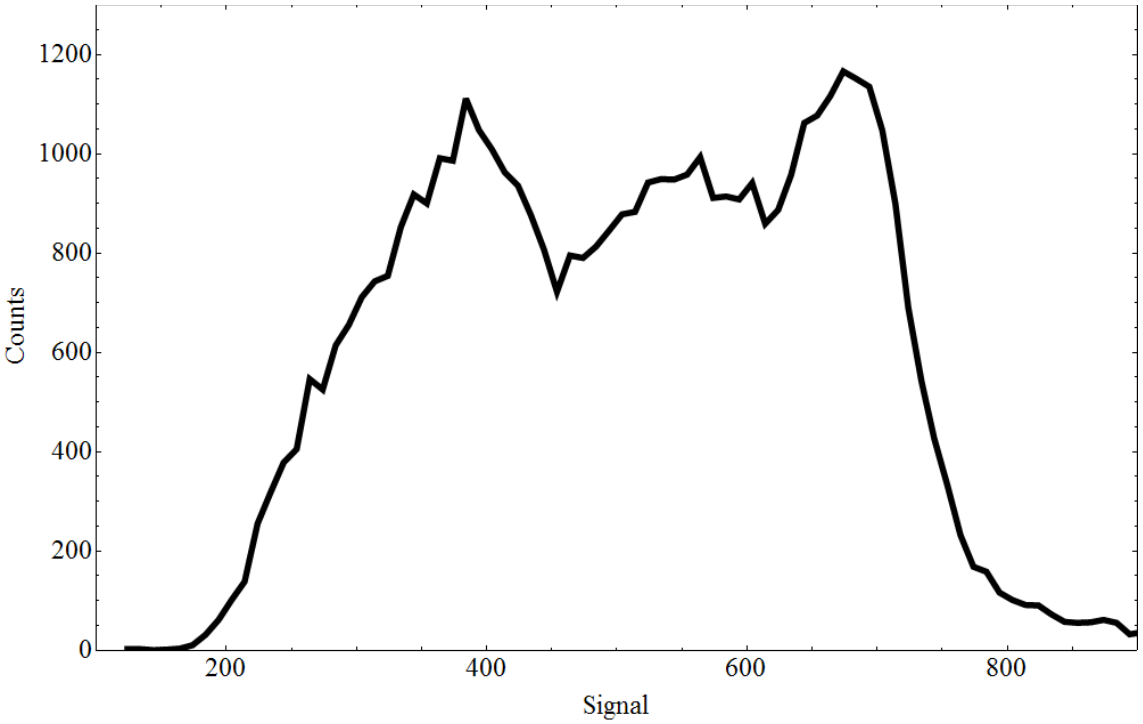

Figure 32 Summed signal read from both ends of the bar, with the source at 12 inches from one end. The lower peak corresponds to the 0.900 MeV radiation from ^{88}Y, and the higher peak corresponds to the 1.836 MeV radiation.

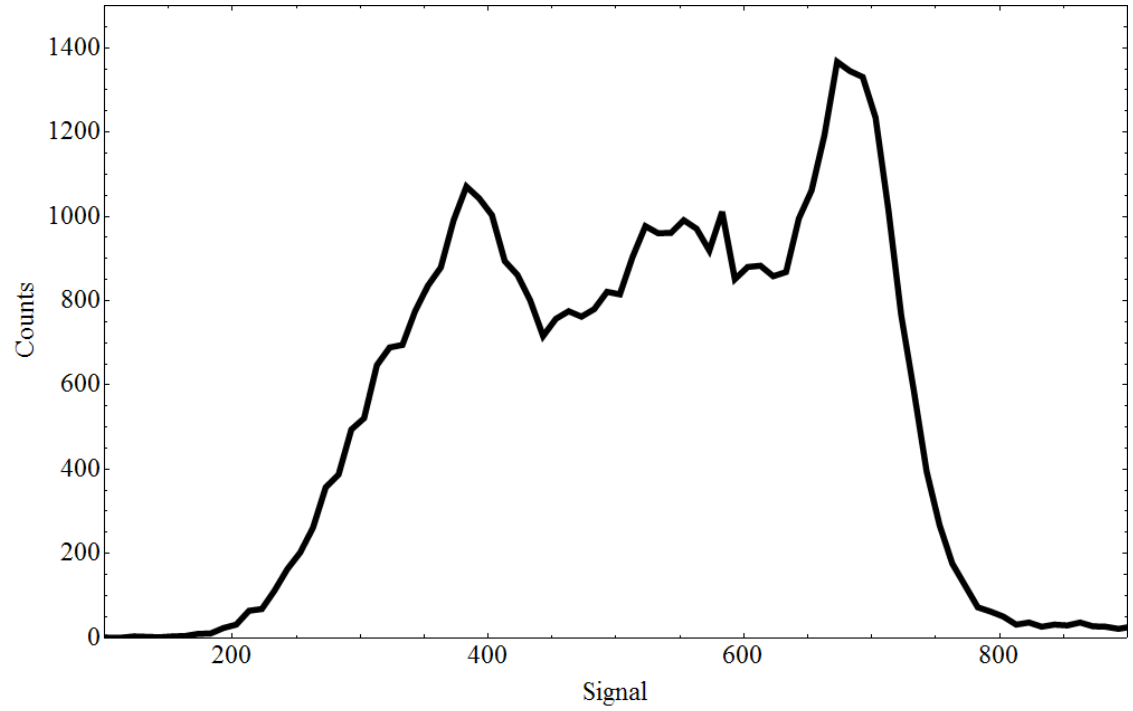

Figure 33 The source is at 20 inches; the center of the NaI bar crystal. The summed signals are dependent on the source location. Therefore it is necessary to normalize the collected signal to the central position of the bar.

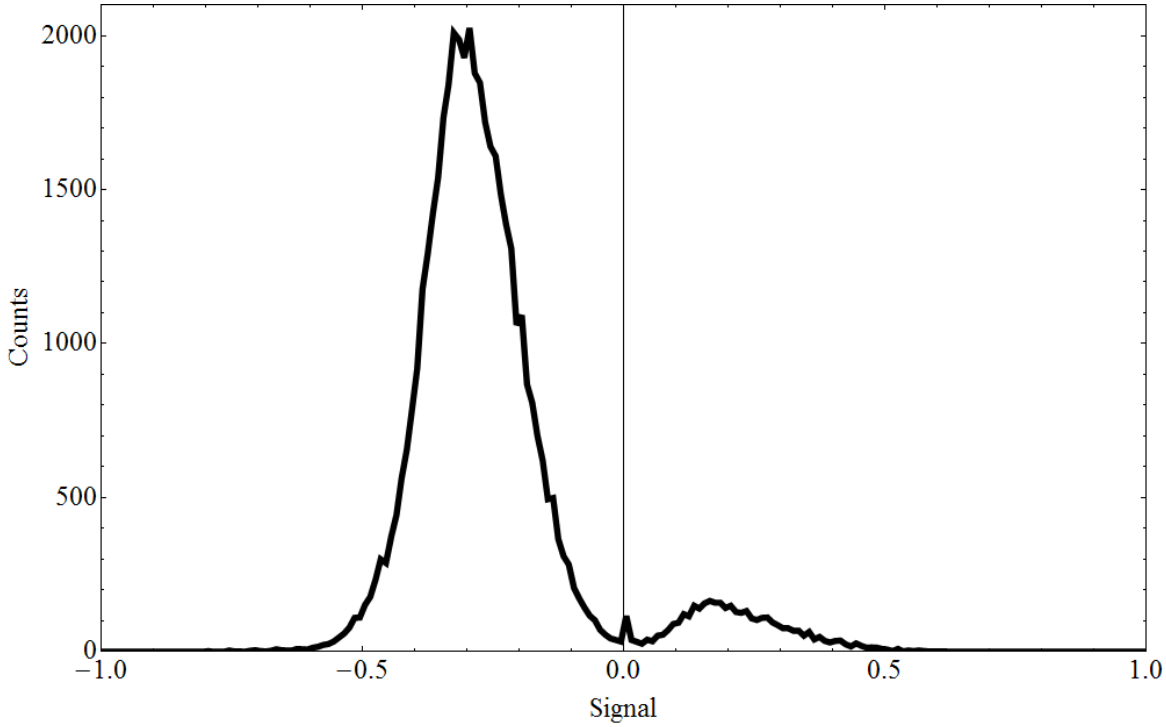

Figure 34 Histogram of (A-B)/(A+B) at 12 inches from one end of the bar.

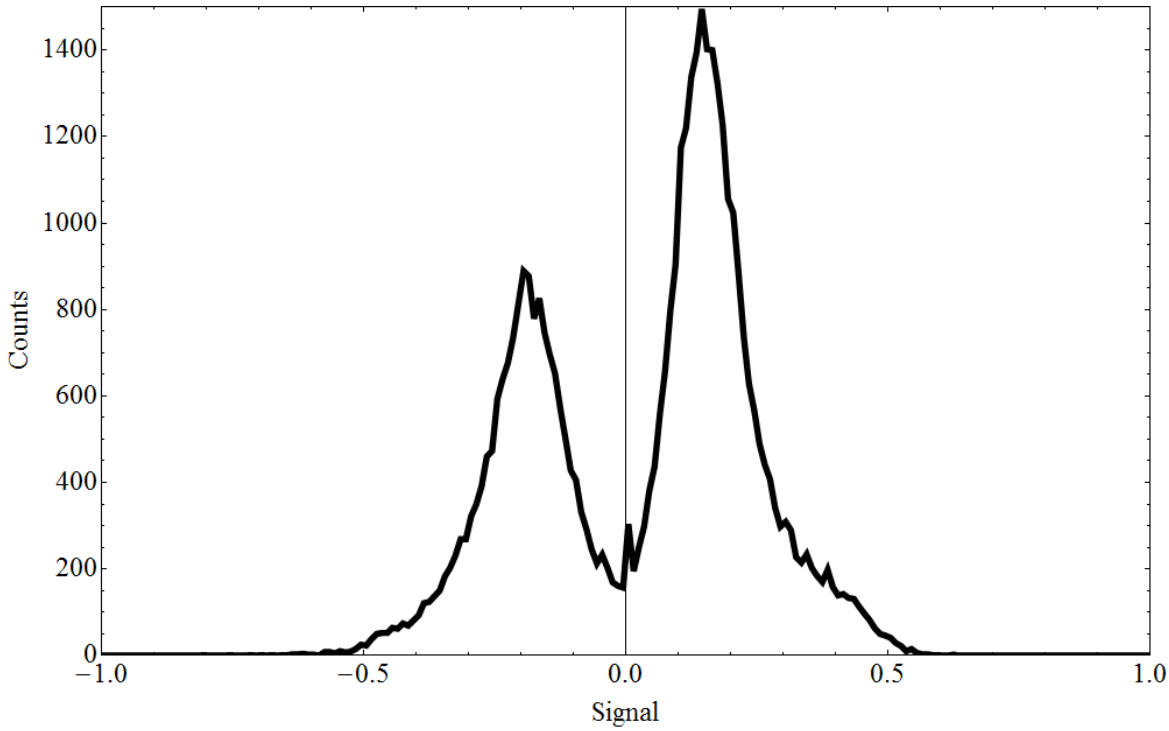

Figure 35 (A-B)/(A+B) at 20 inches. The dominant peak shifts as the source is moved along the bar.

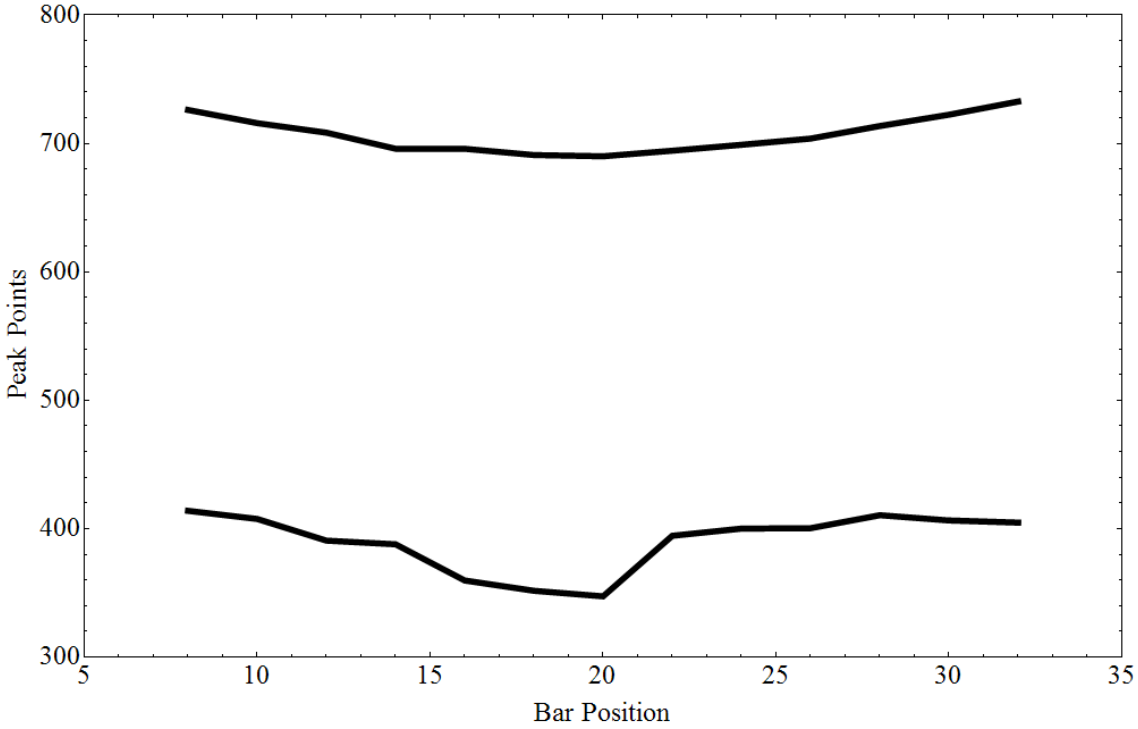

Figure 36 The peaks of (A+B) plotted against the bar position. Since the peak values vary along the bar position, the obtained signals have to be normalized at the center.

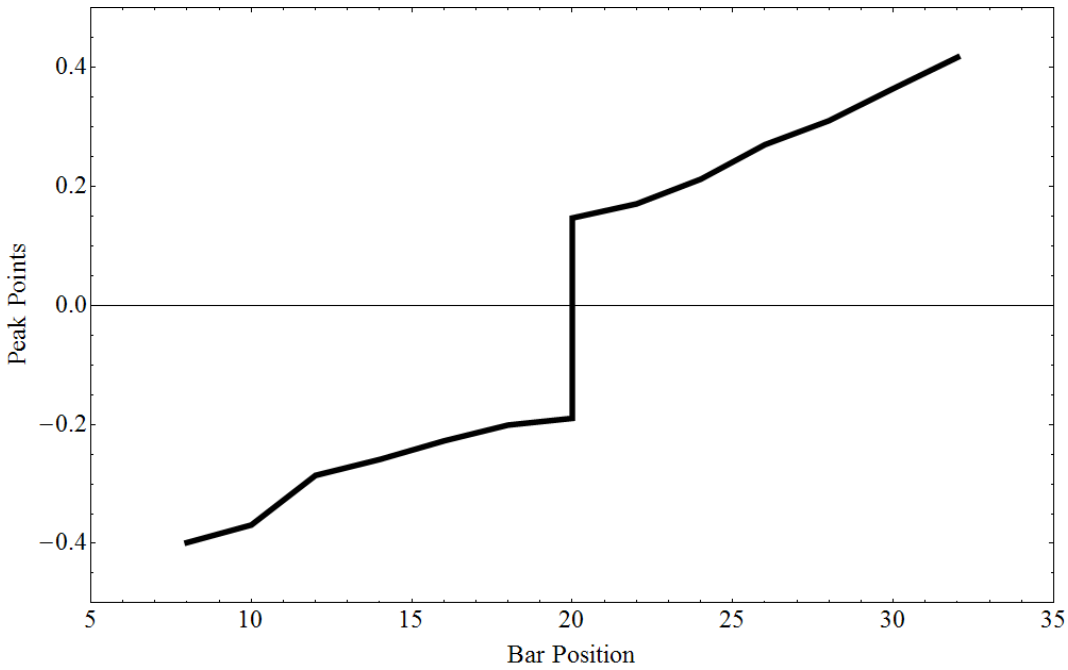

Figure 37 The variance of the (A-B)/(A+B) peak position along the bar. A straight line was fitted for both top and bottom trend.

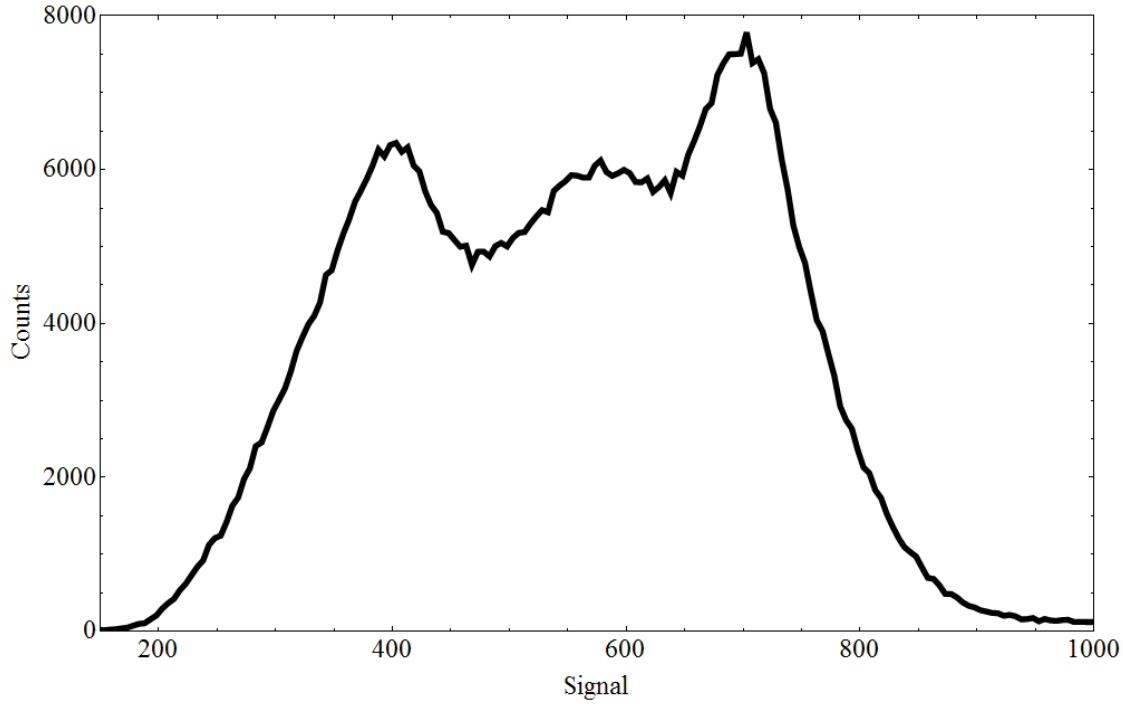

Figure 38 A+B histogram, after normalizing the signal strength to the central position, and combining data retrieved from all positions along the bar. The peak positions determined from this plot is used to convert to energy units.

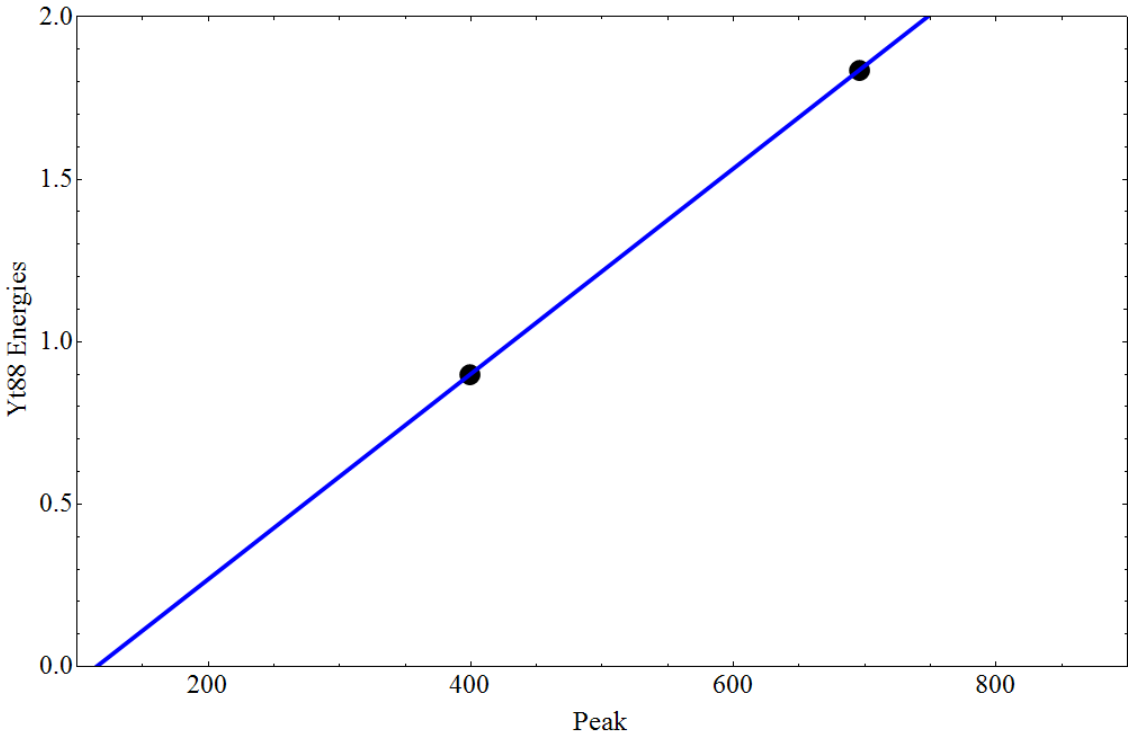

Figure 39 The peak points from Figure 38 plotted against the ^{88}Y radiation energy, fitted to convert signals to energy.

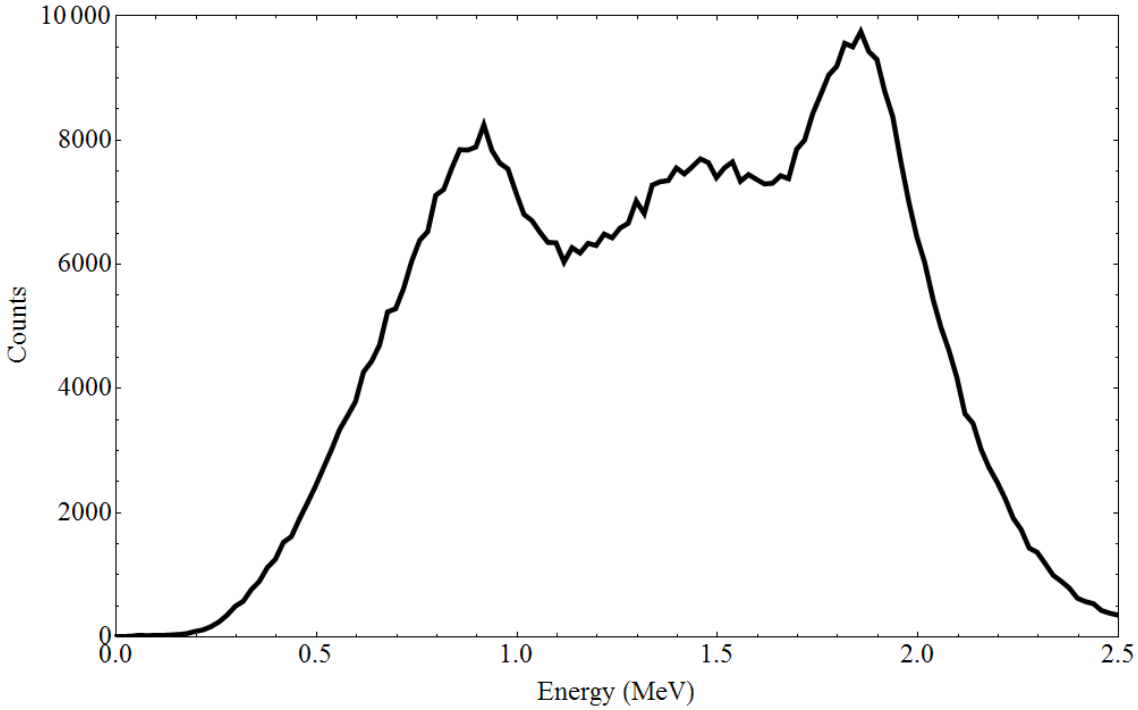

Figure 40 NaI bar energy spectrum for ^{88}Y. A similar spectrum was generated for each NaI bar. These converted values are what would be used for subsequent analysis.

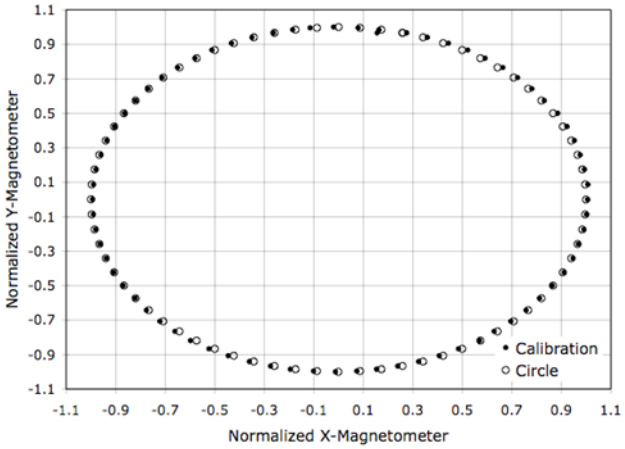

Figure 41 Normalized x- and y-magnetometer values (closed circles) and perfect circle (open circles).

Chapter 7 TIGRE Balloon Flight

Apart from the telescope preparation, the launch date and time are determined by the weather. Low wind is essential to keep the balloon in the local region. Daily weather briefings were held to receive reports on both the stratospheric and surface wind conditions. Once CSBF informed us of the arrival of the turnaround conditions, the telescope's pressure vessel was sealed. The detector was enclosed in it with a pressure of 1 atmosphere, absolute. The insulation was wrapped around the vessel and it was set on its frame.

A. Description of Balloon Flight

The prototype TIGRE balloon instrument was launched from Fort Sumner, NM, on 02 June 2007 at 08:23 LDT. An initial float altitude of 133,800 ft (2.7 mbar or 40.8 km) was reached at 10:46 LDT. After several hours at float, the payload was observed to be moving west rapidly. An hour after launch it was decided to have several members (K. Kamiya and T. J. O'Neill) fly to Holbrook with the others joining at a later time. A 39.57×10^6 cu ft (11.21×10^5 m^3) high altitude scientific balloon weighing 4,148 lbs, or 1,882 kg was used. The scientific payload weighed 1,013 kg and the ballast, parachute and rigging added another 907 kg to the suspended weight. In mid-afternoon (~14:00 LDT) the balloon started slowly descending and continued to descend to 91,800 ft. (28 km) just before sunrise the next day. TIGRE was in float for a total of 27 hours. On June 3, the telescope's CPU was noted to be spontaneously rebooting and the temperature inside the pressure vessel dropped to -15 ºC. After sunrise the balloon rose to 135,800 ft.

(41.4 km) just before termination at 10:54 LDT on 03 June 2007. Impact occurred at 11:45 LDT near Snowflake, AZ. At 05:17 LDT, TIGRE's power was shut off and the observations were ended. With more than 24 hours of observation time, this mission is considered a success. The parachute deployment and decent were nominal. However, the payload landed on a dry river bed and had to be lifted out by a helicopter. The payload was recovered successfully with minimal apparent damage. Figure 42 shows the altitude profile for the flight as well as several temperature profiles. After minor delays in the recovery, the instrument was returned to Ft. Sumner on June 5. Although the top dome of the pressure vessel was slightly dented due to the landing impact, there was no damage to the data.

B. Telescope Flight Performance

While TIGRE was in float, its performance and conditions could be observed at the ground level via telemetry. It was started at launch in the "tracked mode", where it stores gamma-ray information only when there were "hits" in 2 or more consecutive layers in the silicon detectors. Approximately 7 hours later, it was switched to the "non-tracked mode", where it will record any coincidence detection including those with no "hits" in consecutive silicon layers.

i. Temperature and Altitude

The excessive decline in altitude during the nighttime was due to an extended and very high (and cold) cloud layer in western New Mexico. This affected the thermal balance of the balloon, lowering its altitude into the lower stratosphere to a region of very low wind velocity ("turn-around" conditions) and almost stationary position. The decreasing outside air temperature (see Figure 42) in the lower stratosphere accelerated this effect. Passive radiative thermal control for the pressure vessel and interior of the TIGRE instrument is primarily accomplished via the exposed aluminum ellipsoidal dome. The remainder of the pressure vessel was covered with fiberglass insulation. The exterior of the dome was covered with a high emittance low solar absorbance Teflon/Al (α/ε = 0.14) tape. As shown in Figure 42, with an internal power usage of 500 W, the daytime internal ambient temperature stabilized at +12-15^{o} C, decreasing during the night to -14^{o} C just before sunrise the next day. Overall, the telescope operated properly for over 20 hours recording and storing ~2 million events and ~100 GB on the on-board hard drives.

During the last hour of operation the embedded processor rebooted itself several times after the watchdog timer detected the absence of events in several 133-second intervals. We suspect this may have been due to the inability to read and write data to the cold hard drives, triggering a watchdog reboot. Since the processor was unable to find the boot sector properly on the main hard drive it instead booted into the emergency operating system on the on-board flash drive. As a secondary means out of our automated event loop the flash drive is loaded with a minimal operating system (SLAX Linux). Designed to run on small footprint software, it did not contain VME Universe or the

necessary init scripts and software to initialize the VME system. Power recycling could not get the CPU out of this flash drive mode.

ii. Counting Rates

Plots of the summed charged particle shield scalar rate and the event coincidence rate are shown in Figure 43 and Figure 44, respectively. The sampling time was 1.311 s. Spurious counts due to noisy telemetry and missed readout frames have been removed. Missed frames occur when the processor was busy writing to the hard drive. The shield counts reflect the atmospheric charged particle background (including primary cosmic rays) variation with altitude. The large changes in event counts occurred when the telescope was switched to its non-tracked event collection mode and later when the telescope rebooted and switched back to the default tracked event mode. Tracked events required hits in at least two successive silicon detector layers.

Since the observed event counting rate was near the maximum possible rate it was of interest to investigate the distribution of time intervals between successive events. This is shown in Figure 45 for 300,000 events. The observed rate during this period was 32.7/s. It can be seen from the figure that the telescope dead time for recording events (limited by the disk write time) is approximately 21.5 ms for an overall ~70% dead time. This is consistent with the predicted true counting rate of 122.9/s from the exponential fit to the data and corresponding 73% dead time. In the default tracked event mode the dead time was ~8%.

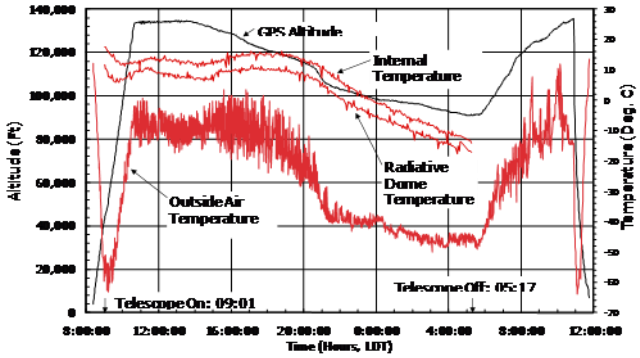

Figure 42 Flight 570N (TIGRE) altitude and temperature profiles

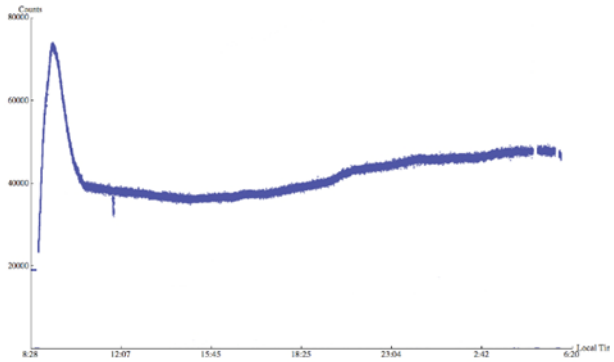

Figure 43 Plastic scintillator charged particle shield counts every 1.311 s.

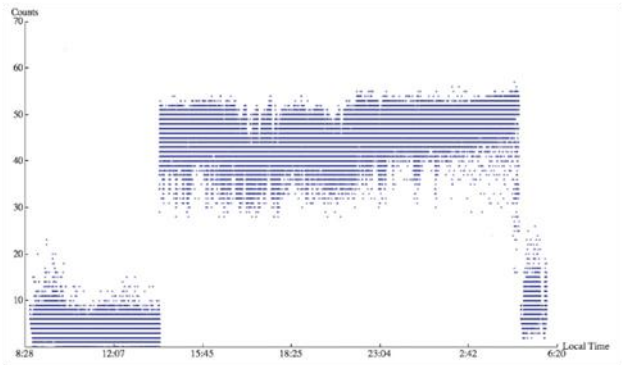

Figure 44 Coincidence event counts every 1.311 s.

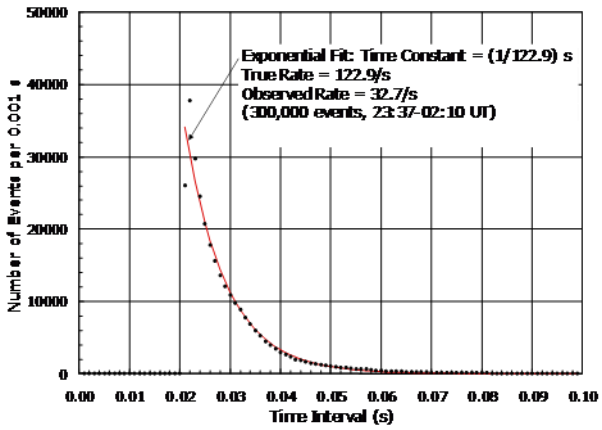

Figure 45 12 Telescope event time-interval histogram with exponential fit.

Chapter 8 Flight Data Analysis (Compton Events)

The flight data was analyzed to search for Compton event candidates. The data chosen for this was the data recorded during the flight time of 13:00 to 20:00 UTC. During this time, TIGRE was running in the "tracked" mode, which requires an electron track trigger to have two or more consecutive hits. The untracked mode includes events with only one silicon layer trigger, in which TIGRE acts as a traditional Compton detector. Since this is an analysis of the new electron tracking feature, the data from the tracked mode was chosen. The total number of recorded events during this time period was 57,958.

A. Flight data readout

The details of the electronics of the silicon readout system are described on page 38. Figure 16 shows pulse height readout from a single silicon board triggered by an event. The 256 channels correspond to the 256 silicon strips on each board. Channels 0 to 127 correspond to the junction side of the detector which produce a negative voltage, and channels 128 to 255 correspond to the ohmic side of the strips which produce a positive voltage. The junction and ohmic strips are positioned orthogonally. A "hit" in the silicon is defined by a trigger in any of the channels above an adjustable threshold voltage, in coincidence with a trigger from the NaI or CsI calorimeter, and no anti-coincident trigger from the charged particle shield.

Later in the Compton reconstruction phase described in page 106, the channel numbers are used to locate the hit position in terms of "x" and "y" positions in detector

coordinates, in cm. The origin of the detector coordinates is set at the outer corner of the fourth silicon stack, on its first ohmic strip and last junction strip, where the magnetometer sensors are located. The pulse height of the signal is calibrated with 122 keV gamma-rays from ^{56}Co and converted to MeV, to determine the energy deposited by the scattered electron. These data taken during the flight are stored as a binary file. To begin the analysis, the first step was to convert the data to a format readable from any note editor such as notepad.

B. Track Identification

First, unused channels or detectors were masked to be not included in the conversion. Some channels were seen to produce a large pulse height in every event, therefore rendering its readings unreliable. These noisy channels were unused. Next, the pulse heights of the NaI Calorimeter were read. For each operational bar, the pulse heights were converted to MeV and the bar positions were deduced in inches, as described in page 77. If the energy was greater than 0.60 MeV, all NaI parameters were recorded. The parameters are energy, bar number and bar position. All positions are in terms of detector coordinates. Next, the pulse height and channel number for each strip with a signal for each triggered silicon layers were read. The pedestal values (voltage fluctuation observed without any source present) were subtracted from the recorded voltages, and then converted to keV.

Simultaneously, cuts and cleanup were made to certain hit conditions. Valid hits occur only if the pulse-height has an energy loss above 60 keV and if there are no more

than 3 hits in one layer in either the ohmic or the junction side. Otherwise, the event is ignored. If there is only one hit from the silicon in the entire event, the event will be ignored. If the event consists of hits from only the junction or ohmic side, the event will be ignored.

After this preliminary filter, an output file in a readable format is generated. The file contains the following information: The unique event number, number of silicon interactions (i.e., hits), number of layers hit, time of event, the ohmic channel number for each interaction, the junction channel number for each interaction, the energy of the interaction, the energy of the NaI bar interaction with the scattered photon, the identification of the NaI bar, and the NaI interaction position along the length of the bar in inches. There were no events in coincidence with the CsI calorimeter due to the high threshold level.

For the purpose of selecting Compton events, further cleanup of the file was needed. First, clusters were taken into account. If the silicon hits on a single detector were one or two strips apart, they were determined to be the same hit. Their hit locations are recorded as one and their energies are added. If they are more than three channels apart, they are determined to be different hits and are left as they are. Examples of clusters are show in Figure 48.

Next, the ratio between the number of silicon hits during an event and the number of silicon boards triggered in that same event was calculated. If the ratio, (# of hits)/(# of boards), was greater than 1.25, it was assumed to be more likely a type of interaction

other than Compton, such as Pair creation. Therefore, events with the ratio greater than 1.25 were ignored.

If there was a silicon tower with readings from either the junction side or the ohmic side only, the stack was ignored. After these eliminations, it was necessary to see if the rest of the hits resembled a track. To determine this, a straight trend line was generated using all layers with one and only one hits, and its χ^2 was calculated. If the χ^2 value was close to 1 it is most likely that the hits are correlated to each other. For our purposes, if the χ^2 was less than 0.85 and the event consisted of 4 and more silicon hits, any stacks with only 1 silicon hit were ignored. If there were only 2 hits in a stack, and those hits were separated by more than 4 layers, the stack was ignored.

If the trigger only recorded the signal from the junction side, the strip number of the ohmic side was estimated by extrapolating the trend line on the layer. Combined with the recorded strip number of the junction side, this will now be seen as a definite hit. An example of this is shown in Figure 46.

If there was a layer with 2 hits, this record consisted of two readings from the junction side, and two readings from the ohmic side. To determine the correct combination, a straight trend line was generated using only the layers with single hits. The junction and ohmic combination closest to the trend line was kept, and the other readings were ignored.

C. Procedure for finding Compton events

After these preliminary cuts were performed, the number of tracked events was decreased to 20,754. The goal is to reconstruct the incident photon's direction and energy from the Compton interaction with the telescope. First, further sorting is done to choose only Compton events.

i. Coincidence with the NaI bars and single hit per layer

The first step was to look for events in coincidence with one of the NaI calorimeter bars. The NaI bars were solely used for analyzing the scattered photons. The poor timing resolution of the CsI-PD detectors led to very few Si-CsI coincidence events during the flight.

Some Si-NaI events were recorded without a NaI recorded pulse heights although ground level calibrations did not yield such events (Figure 50). TIGRE was designed to clear burst scaler readings in the CAMAC crate every 5.12 ms. Inadvertently, a line of flight code that also cleared the CAMAC ADCs every 5.12 ms, including those in the NaI bars, was not removed for the flight. This, at a minimum, is believed to be responsible for the zero NaI PHA readings. Also, the NaI parameters were recorded only if there was a hit in bars 4, 5, or 6. NaI readings in bars 1, 2, 3, 7, and 8 were difficult to calibrate because of the poor condition of the NaI bars (i.e., they had numerous cracks). Therefore, position and energies in these bars were recorded as 0. In order to reconstruct Compton events, an interaction with a calorimeter must exist. Therefore, any events without NaI pulse heights are ignored. 7,109 events were cut for this reason.

ii Definite hits requirement and dummy hit elimination

The second step was to look for single triggers in a given silicon layer. If there were two separate hits on a single silicon layer, the event was ignored. Also, after the cleanup described in page 95, triggers with only either ohmic or junction reading still existed (Figure 51). Though pulse heights solely from the junction do not provide useful information for the location of the scattered electron, they give the value of the deposited energy. Therefore, if the hit contained no more or less than one pulse height from the junction side, this energy information was used for reconstructing the event. Information from the ohmic side only provides the hit location, which is useful only when coupled with the junction side. Therefore, if there are still hits from the ohmic side only at this stage, the hit is ignored.

iii. Originate within detector

In the next step, only tracks which were contained within the silicon array are selected. First, tracks that travel across the stacks of silicon detectors were ignored, since it is most likely that these events are high energy cosmic ray particles rather than photons. 2,100 events were cut.

Next, only tracks contained within the volume of the detector were chosen. If the beginning of the electron track is the topmost layer of the silicon stack, it is unclear if the incident gamma-ray interacted with the silicon first, or if it interacted with material

outside the silicon tower. Similarly, if the end of the electron track is the last layer of the silicon stack, it is uncertain if the Compton event track is stopped at the last layer, or if there was more energy present in the recoiled electron (Figure 51). Therefore, the analysis was limited to tracks that were contained within the stack, i.e., begins and ends in the 2nd through 14th. After this, the trend line of the main electron track was extrapolated to the layers above and below the layers of the first and last interaction. This was determined in terms of x and y coordinates of the detector. If the x and y positions was not within the boundary of the active area of the silicon stack, the event was discarded. Here, 1,944 events were cut.

iv. NaI Event Selection

Some events were recorded with multiple interactions in the NaI calorimeter, usually with unrealistically high energy deposits (Figure 52). A sorting procedure needed to be carried out to select the signal most likely to be associated with the electron track. The NaI bars produced high energy events above 6 MeV, which were clearly unrelated to the ~MeV Compton events. Therefore, any interaction above 6 MeV was not included in the analysis. Those were most likely cosmic rays leaking through the anticoincidence shield. Numerous events were seen at lower energies as well, producing multiple NaI interactions for each event. In the interest of simplifying the process of finding the NaI interactions correlated to the electron track, interactions below 0.7 MeV were not included as well. 5,791 events were excluded for this. If there were still multiple NaI hits after this selection, clusters were identified. For all NaI interactions that were found

to be in adjacent bars and within 7.5 cm of one another along the bar length, the interaction locations are averaged, the medium bar was selected and the energies were summed. After this selection, if there are still multiple interactions, the record with the lowest energy is selected for the most likely interaction due to a scattered photon from Compton events.

After these filters, 3,810 events were left. These were events with definite silicon recordings for the tracked electron, and one Calorimeter reading associated with it by the scattered photon (Figure 53 and Figure 54).

v. Direction of Motion

In the next step, the direction of motion is determined for each recoil electron track with 2 or more consecutive layers of interactions. Previously, Compton and pair telescopes used the time-of-flight (TOF) of the scattered gamma-rays or pair particles between two scintillator arrays to determine their direction-of-motion and discriminate against unwanted background. TOF was crucial to the success of these experiments. This required a large converter-calorimeter separation and small field of view (FOV) and corresponding lower efficiency. To increase the FOV and detection efficiency, smaller converter-calorimeter separations are needed. The use of position sensitive solid state (i.e., Si or Ge) with their much improved energy resolutions but poorer TOF capability required another background discrimination approach. Using the track record of energy loss and position in each silicon layer traversed, TIGRE introduced the direction-of-motion (DOM) parameter for each track (O'Neill, et al., 1995).

Since TIGRE has a large FOV, it accepts gamma-rays from all directions. Therefore it is necessary to determine if the electron tracks are moving upward or downward. The method chosen to do this is by simply looking at the energy ionization energy loss and the multiple Coulomb scattering of the stopping electron in each silicon layer. As the stopping electron traverses through the silicon layers, due to the increasing ionization energy loss of electron traversing through thin matter, each interaction causes increasing momentum loss. As it loses momentum, the electron will deposit more measured energy loss in successive layers. Therefore, one may determine the correct direction by looking for the direction which records increasing energy deposits. Since the Compton electron is always forward scattered, its direction gives a sense of the incident gamma-ray's direction. A quantitative measure of the DOM is the Pearson Correlation, described in Zoglauer (2006). It uses the covariance of the deposited energies expressed as

$$\mathrm{cov}\left(E_{dep}, i\right) = \overline{E_{dep} \cdot i} - \overline{E_{dep}} \cdot \bar{i}$$

where E_{dep} is the deposited energy recorded on each silicon strip and i is the layer number starting with the assumed origin layer. The Pearson Correlation coefficient is the covariance divided by the variances of the involved variables. It has a value between -1 and +1.

$$PC\left(E_{dep}, i\right) = \frac{\overline{E_{dep} \cdot i} - \overline{E_{dep}} \cdot \bar{i}}{\sqrt{\overline{E_{dep}^2} - \overline{E_{dep}}^2}\sqrt{\overline{i^2} - \bar{i}^2}}$$

To determine the direction of motion, the Quality Factor was calculated, which is given by

$$Q_{E,Pearson} = 1 - \frac{1 + PC\left(E_{dep}, i\right)}{2}$$

This Quality Factor was determined by finding the Pearson Correlation first assuming the tracks are in the downward direction, and then repeated by assuming the tracks in the upward direction. The Pearson Correlation will return a value close to +1 for the correct direction, and -1 for the incorrect direction. Using these values of the Pearson Correlation, the Quality Factor was calculated for both assumed directions. The Quality Factor is normalized such that $Q_{E,Pearson}$ is close to zero for correct directions and close to one for incorrect directions. Therefore, the direction with the lower Quality Factor is chosen.

The validity of the Pearson Correlation and the Quality Factor were tested with the data taken with a ^{90}Sr electron source below the last silicon layer. In this way all events are in the upward direction, and the PC and QF should show this. Figure 55 shows the histogram of the resultant PC values, assuming the events move upwards. It shows most of the events are correctly identified as upward tracks. Figure 56 is the QF calculated from the same PC result. The peak leans strongly towards 0, showing the correct upward identification. For events with four or more electron hits, the Pearson Correlation may also be applied to the angle between the electron entering the silicon layer and exiting the layer. However, when this was applied to the ^{90}Sr calibration data, the results were inconclusive.

To see the portion of the events correctly identified, the QF was calculated both assuming upwards and downwards motion and the smaller value was chosen, as would be

done when searching for Compton events from the flight data. A histogram of this minimum QF is shown on Figure 57. To have a stronger confidence of choosing the correct direction, one may define a maximum value of QF to accept. Given the two choice of upward or downward, the smaller value of QF is always less than 0.5. If one chooses to accept QF values to not exceed 0.4, for example, only a portion of the data will pass this criteria. The smaller the cutoff value, the fewer events will pass.

However, this way the portion of the correctly identified direction (in this case upward) of the number of events that passed the cutoff will increase as the cutoff value becomes stricter. This percentage of the events that is correctly identified out of the entire data is what can be expected from the actual flight data, where the actual direction can only be deduced. When this method is applied simultaneously to all the ^{90}Sr events, the fraction of correctly identified directions is lower than actual results for 4 or more hits. This is because most events are of electron tracks with two hits, for which the minimum QF value is always zero. The fraction of correctly identified events does not vary with the QF cutoff value chosen for these events. Therefore, the calibration data was separated according to the number of electron hits, and the QF cutoff criteria was applied to events separated by the number of electron hits. The data was separated by 2 hits, 3 hits, 4 hits, and then 5 or more hits. 15,938 events were collected from the ^{90}Sr calibration, 8,852 were events with two electron track hits, 6,310 were events with three hits, 624 events had four hits, and 152 events had electron tracks of five or more hits. Figure 58 shows the increase in the number of events identified with the correct direction, as the cutoff QF values were made stricter.

The QF was calculated for both upward and downward scenarios, and the direction was determined to be the one with the smaller QF. Only events with a QF value of 0.1 or less were chosen. This will ensure at least at 78% confidence that the events were actually in the direction that the QF determined them to be in. 2,250 events were cut for this. After this cut there were 1,560 events left for analysis. Of the 1,560 events, 993 had two hits in the silicon detectors, 342 had three, 143 had four, and 82 consisted of five or more hits.

This method of determining the direction of motion was applied to the flight data. Figure 59 is the histogram of the Pearson Correlation of the flight events, categorized by the number of electron hits. The figure shows more events gathered at -1, which is upward. Figure 60 is the histogram of the smaller value of the Quality Factor, which determined the direction of the track. This was also separated by the number of hits in the electron tracks. QF values closer to 0 give more confidence of the direction chosen. The longer tracks (4 or more electron hits) shows a slight tendency toward the higher QF value. However, with a 0.1 QF cutoff value, we can be at least 78% certain that the correct direction was chosen. Of the 1,560 flight events, 698 events were identified to track downward and 862 events were moving in the upwards direction.

D. Event Reconstruction

To find the incoming direction of the incident photon, first its momentum must be derived. The first interaction layer in the silicon is where the incident photon interacts via Compton scattering. The second layer hit gives the initial direction of the recoiled

electron. The information from the NaI bar interaction is the absorption information for the scattered photon. To study the tracking design of TIGRE, the tracked events in the initial of the balloon flight were used, as described in the beginning of this chapter.

i. The calculations

From layer 1, the information x_1, y_1 and z_1 is obtained. From layer 2, the information x_2, y_2 and z_2 is obtained. From the NaI bar, E', x_{ph}, y_{ph} and z_{ph} are obtained. K, the kinetic energy of the electron, is obtained by adding all the electron energy deposited in the layers along the track. E_0, the energy of the incident photon, is simply K+E'. The second step is to find the unit vectors of the recoiled electron and scattered photon.

$$
\begin{aligned}
x_{e^-} &= x_2 - x_1 \\
y_{e^-} &= y_2 - y_1 \\
z_{e^-} &= z_2 - z_1 \\
x_{ph} &= x_{ph} - x_1 \\
y_{ph} &= y_{ph} - y_1 \\
z_{ph} &= z_{ph} - z_1
\end{aligned}
$$

where the indexes "1" and "2" indicate the electron track sequence in the direction determined by the Direction of Motion process described in the previous section. The magnitudes of these vectors are

$$
\begin{aligned}
\left|\overrightarrow{e^-}\right| &= \sqrt{x_{e^-}^2 + y_{e^-}^2 + z_{e^-}^2} \\
\left|\overrightarrow{ph}\right| &= \sqrt{x_{ph}^2 + y_{ph}^2 + z_{ph}^2}
\end{aligned}
$$

Then the unit vector component vectors for both the recoiled electron and scattered photon are

$$\hat{e}_x^- = \frac{x_{e^-}}{\left|\overrightarrow{e^-}\right|} \quad \hat{ph}_x = \frac{x_{ph}}{\left|\overrightarrow{ph}\right|}$$
$$\hat{e}_y^- = \frac{y_{e^-}}{\left|\overrightarrow{e^-}\right|} \quad \hat{ph}_y = \frac{y_{ph}}{\left|\overrightarrow{ph}\right|}$$
$$\hat{e}_z^- = \frac{z_{e^-}}{\left|\overrightarrow{e^-}\right|} \quad \hat{ph}_z = \frac{z_{ph}}{\left|\overrightarrow{ph}\right|}$$

Equation 17

To find the momentum, we can go back to basic principles of conservation of energy and momentum. From conservation of energy, the total energies before and after the collision are

$$E_0 + m_e c^2 = E' + K + m_e c^2$$

where E_0 = initial gamma-ray energy, $m_e c^2$ = electron rest mass energy, E' = scattered gamma-ray energy, and K = kinetic energy of scattered electron. Therefore, $E_0 = E' + K$. Also from relativistic mechanics,

$$E^2 = c^2 p^2 + (mc^2)^2$$

This can be applied for the electron's total energy after the collision.

$$(K + m_e c^2)^2 = c^2 p_e^2 + (m_e c^2)^2$$

$$K^2 + 2Km_e c^2 + (m_e c^2)^2 = c^2 p_e^2 + (m_e c^2)^2$$

$$p_e c = \sqrt{K^2 + 2Km_e c^2}$$

Equation 18

The energy read from the silicon hits is K, so applying this information to Equation 18 will yield the momentum of the recoiled electron. For the scattered photon, $E'^2 = c^2 p_{ph}^2$, so the recorded energy from the NaI bar will yield the momentum. For simplicity, the speed of light c has been left in the calculation result.

After finding the momenta, they are applied to the component vectors found in Equation 17.

$$\vec{p}_{e^-} = p_{e^-} \cdot \hat{e}_x^- + p_{e^-} \cdot \hat{e}_y^- + p_{e^-} \cdot \hat{e}_z^-$$
$$\vec{p}_{ph} = p_{ph} \cdot ph_x + p_{ph} \cdot ph_y + p_{ph} \cdot ph_z$$

Adding these two vectors, we now have the direction and momenta of the incident photon.

$$\vec{p}_{inc} = \left(p_{e^-} \cdot \hat{e}_x^- + p_{ph} \cdot ph_x \right) + \left(p_{e^-} \cdot \hat{e}_y^- + p_{ph} \cdot ph_y \right) + \left(p_{e^-} \cdot \hat{e}_z^- + p_{ph} \cdot ph_z \right)$$

Equation 19

The Compton scattering angle was determined geometrically by finding the dot product between the scattered photon's momentum vector and the incident photon momentum vector.

$$\theta = \cos^{-1}\left(\frac{\vec{p}_{ph} \bullet \vec{p}_{inc}}{\left|\vec{p}_{ph}\right|\left|\vec{p}_{inc}\right|} \right)$$

Similarly, the recoiled electron's angle was determined by the dot product between the electron's momentum vector and the incident photon's vector.

$$\phi = \cos^{-1}\left(\frac{\vec{p}_{e^-} \bullet \vec{p}_{inc}}{\left|\vec{p}_{e^-}\right|\left|\vec{p}_{inc}\right|} \right)$$

These angles depend on both the individual energy measurements, and the recoil electron and scattered gamma-ray directions.

ii. Results

Figure 61, Figure 62 and Figure 63 show the distribution of the energies of scattered photon, recoiled electron and incident photon respectively. From Figure 61, it can be seen that because the energy of the NaI Calorimeter tend to be larger than the energy deposited in the silicon stack, its contribution to the energy of the incident photon is more substantial. Figure 63 shows the energy of the incident photons above 1 MeV. The decrease in events blow 1.5 MeV is due to the silicon and NaI threshold energies.

The angles of the scattered photon and the recoiled electron obtained geometrically as described in the previous section were compared with the angles obtained using the Compton formulas Equation 8 and Equation 12 (Figure 64 and Figure 65). The direction of motion was used to assign the vector directions of the recoil electron for the flight events. These scatter plots do not show the expected 1:1 correlation between the angles determined from the Compton scatter formulas and the measured directions. The deviation from the 1:1 ratio can be attributed to the lack of correlation of the electron track with the interaction in the calorimeter. The unexpected frequency of high energy losses in the calorimeter and also the absence of any losses in some instances support the belief that the electron and scattered photon measurements were not from the same Compton scatter event. The technical reasons in this will be discussed in the conclusions.

The Compton angle and the electron scattering angle compared with the incident photon energy are shown in Figure 66 and Figure 67. Figure 66 shows the angles, calculated by both methods, have some similar characteristics; i.e., the Compton scatter angles decrease with increasing energy, though they are smaller than expected. In Figure 67, the electron scattering angles calculated from the momentum vectors of the electron and the incident photon have a far greater range than the angles determined from Equation 12. The angles obtained geometrically have results extending to larger angles up to the maximum allowed value of 90º. This may be attributed to the direction of motion found in page 102, where some electrons were determined to be in the upward direction. However, most energies of the scattered photon are ~5 times greater than the kinetic energy of the recoiled electron. This gives an incident photon vector that is much larger than that of the electron's, which reconstructs the incident direction as downward, even though the electron is moving upward. Still, some scattered electron angles were larger than 90 degrees, so the direction of motion was reversed for such instances. Of the 862 tracks that were determined to be upward by QF, 417 tracks were reversed to downward for this reason. These were included in Figure 67.

Figure 68 show the angles of the scattered photon and the recoiled electron calculated from the momentum vectors. Figure 69 show the same comparison, but the angles were determined by using the Compton formulas. This shows that theoretically they should be inversely related. The total angles between the electron and scattered photon were obtained first by adding the results of Equation 8 and Equation 12, then by taking the angles between the momentum vectors of the scattered photon and the recoiled

electron. These latter angles should be dependent only on the measured directions and not on the measured energies. To see the effect of the electron track length on the results, the comparisons were made for each electron track length (Figure 70). Again, the lack of any correlation is evident.

A sky map was generated for the incident photons to visualize their origin, expressed in terms of detector coordinates (Figure 71). Their momentum vectors from Equation 19 were divided by its magnitude to return a unit vector.

$$\hat{ph}_{xinc} = \frac{ph_{xinc}}{\left|\overrightarrow{ph}_{inc}\right|}$$

$$\hat{ph}_{yinc} = \frac{ph_{yinc}}{\left|\overrightarrow{ph}_{inc}\right|}$$

$$\hat{ph}_{zinc} = \frac{ph_{zinc}}{\left|\overrightarrow{ph}_{inc}\right|}$$

TIGRE operated in the tracked mode for approximately 18,436 seconds. During this time, there were a total of 57,958 triggered events recorded. The cuts and screening process described in this chapter was applied to these events to search for Compton events and yielded 1,560 potential events. The minimum and maximum energies of the incident photon were 0.88 MeV and 7.89 MeV respectively.

There are several possibilities for the discrepancy between the 24,102 theoretical Compton event yield and the 1,560 Compton events found during flight. First, the total number of events recorded in the 18,436 seconds of flight time was 57,958 events. TIGRE's dead time was 21.5 ms and the true counts can be obtained by

$$N_{true} = \frac{N_{obsC}}{1 - N_{obs\_tot}\left(\tau / t\right)}$$

where N_{true} is the true expected counts without the dead time, N_{obsC} is the observed number of Compton events, N_{obs_tot} is the observed number of total events, τ is the dead time, and t is the observation time. In 18,436 seconds of flight time, the predicted true number of Compton events is 1,673. Clearly the dead time did not make significant contribution to the loss of Compton events.

Another reason for the discrepancy may lie with the NaI calorimeter. As described in page 99, the flight data contained events without NaI pulse height readings. At the stage of data readout described in page 99, out of 20,754 events there were 7,109 events without NaI readings. All of this was eliminated, as it is impossible to analyze for Compton events without it. Also, as shown in Figure 30, the energy threshold of the NaI bars greatly affects the number of Compton events. For the flight data, events below 0.7 MeV and above 6 MeV were not analyzed which excluded 5,791 events. This, together with the fact that only 3 out of 8 bars were used, contributed to the low find. This was coupled with the fact that only 1 out of 4 silicon towers were mainly operational, due to the random triggers seen in other layers.

To test the effect of few operational detectors, the mass model in MEGAlib was adjusted to match the flight conditions. For the NaI calorimeters, the 3 central bars were left untouched and the 5 outer bars (2 on one side and 3 on the other) were turned off. All the CsI calorimeters were turned off. 3 stacks of silicone detector were turned off. The third simulation described in page 65 was repeated with this configuration. Cosima

was set for an isotropic radiation with $E^{-1.42}$ power law spectrum. The flux was 0.588 gamma/cm^2 and the energy range was 1.0-10.0 MeV. Revan found 42 Compton events from 18,069,568 incident gamma rays. Using these values in Equation 15 and Equation 16 number of Compton events predicted during the balloon flight was decreased from 24,102 to 1,781. The standard uncertainty is 275, which puts 1,560 well within this error.

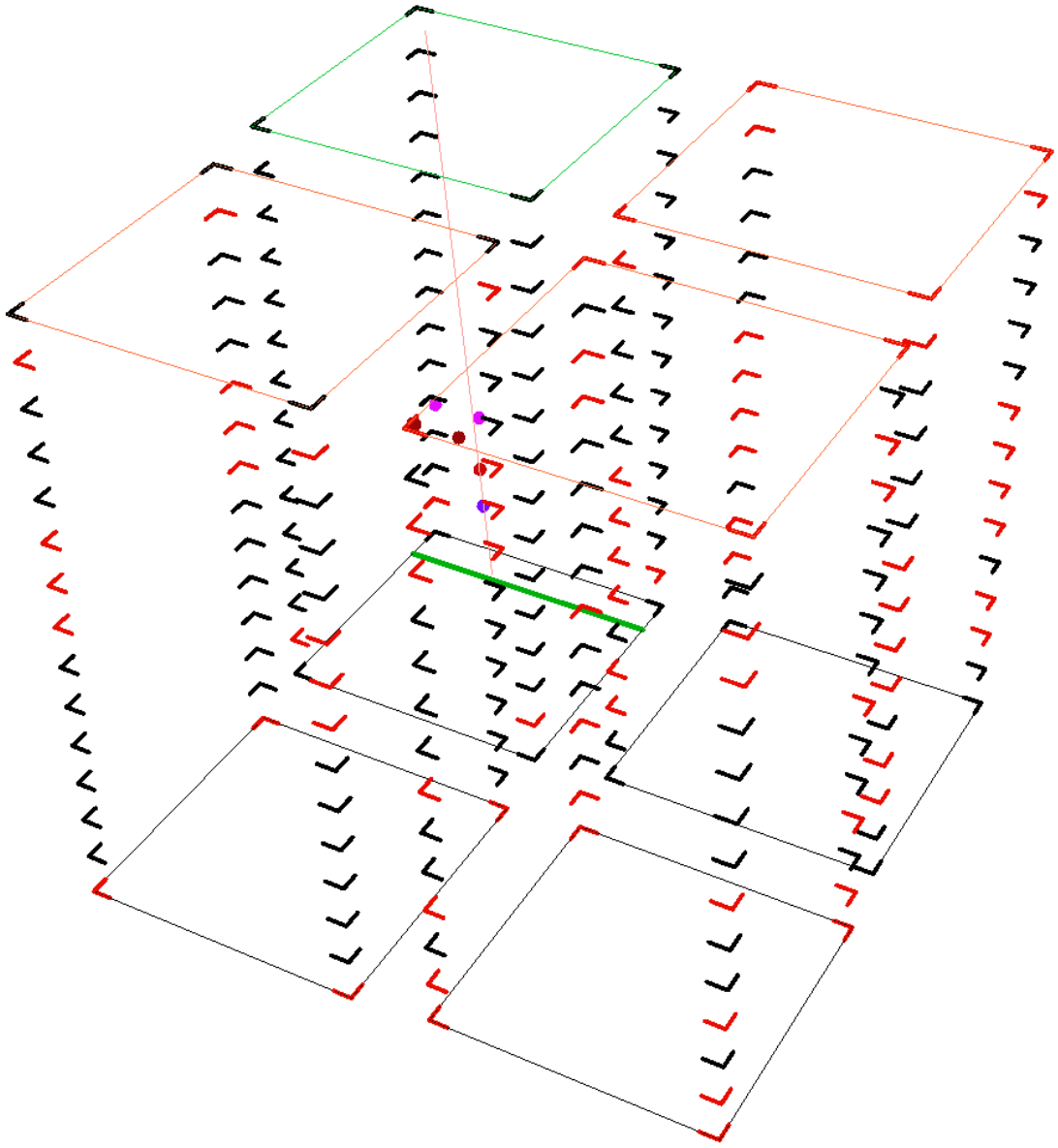

Figure 46 Example of an electron track with a hit which recorded only x or y.

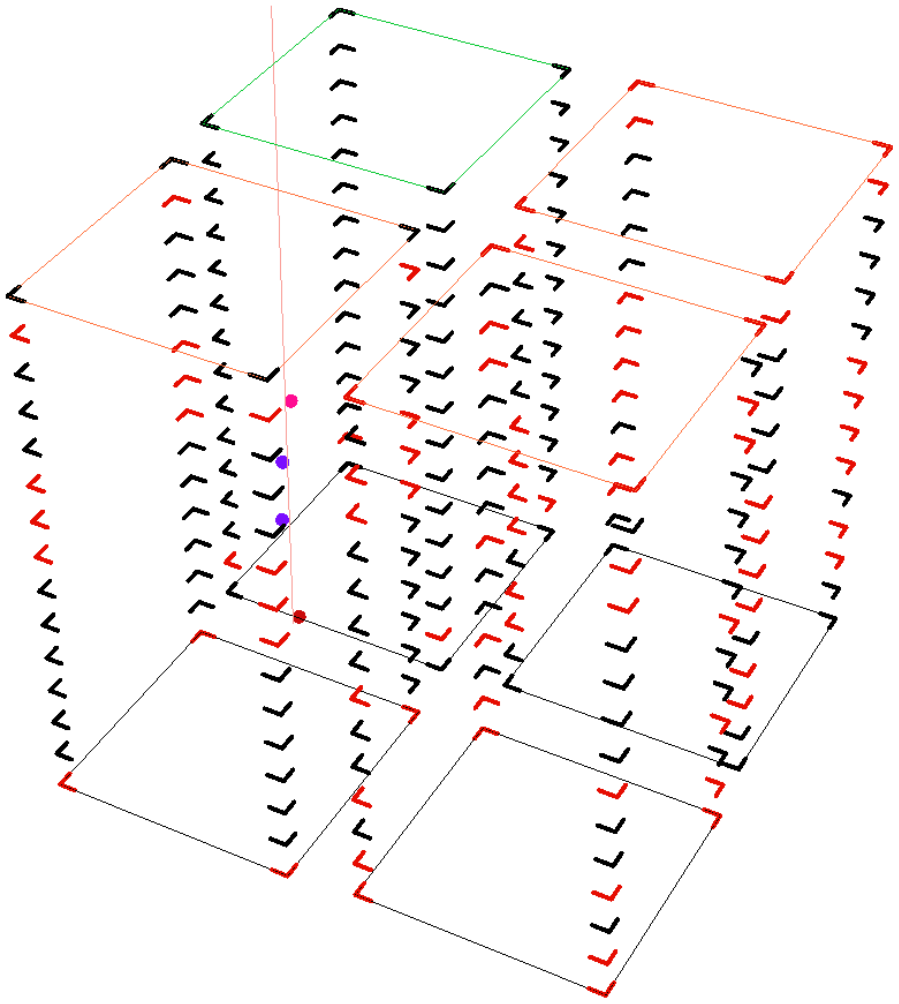

Figure 47 Example of an electron track with a gap. It is clear that there should be a hit seen between the end of the sequence and the hit previous to it.

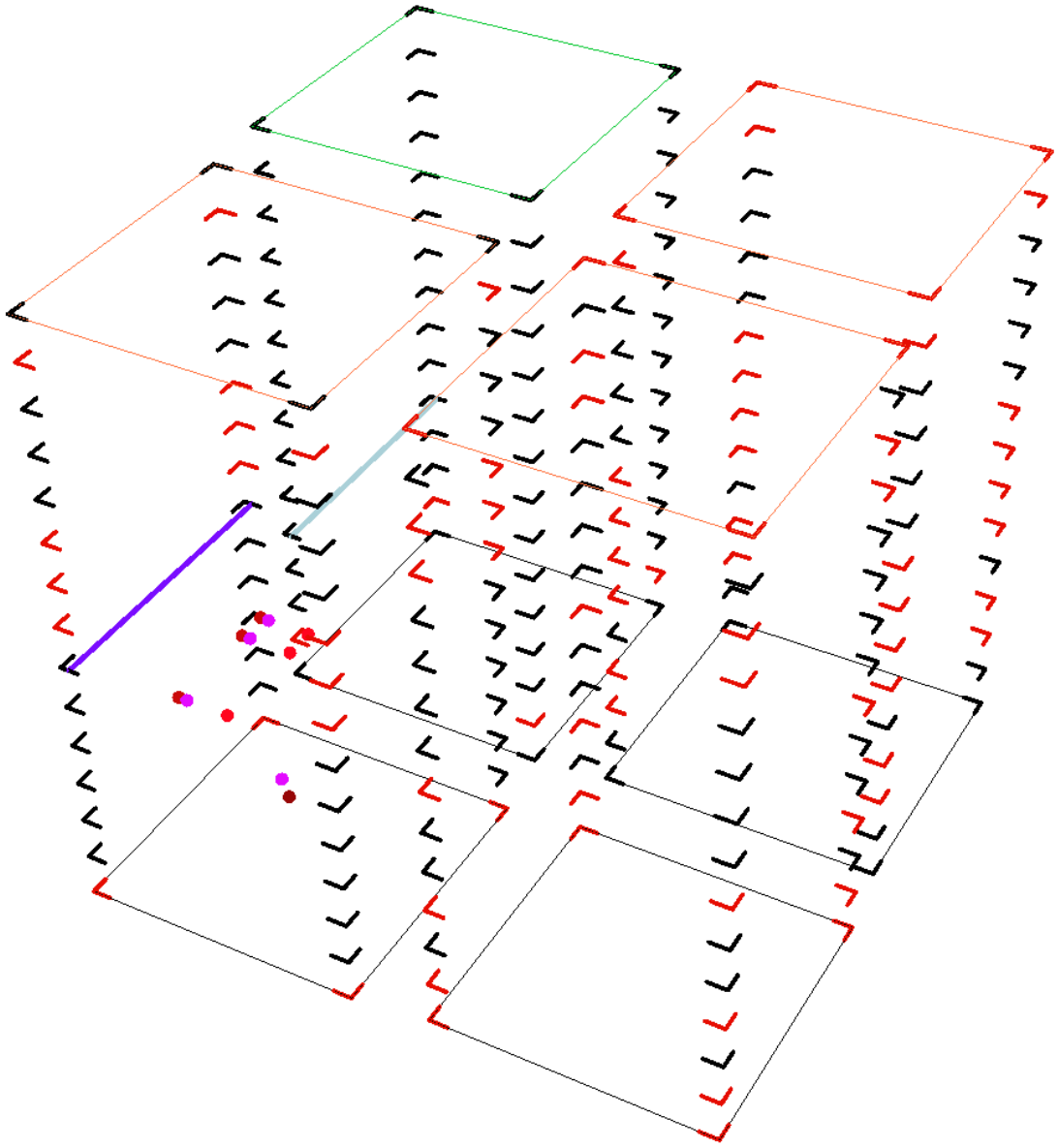

Figure 48 An example of an electron track with clusters.

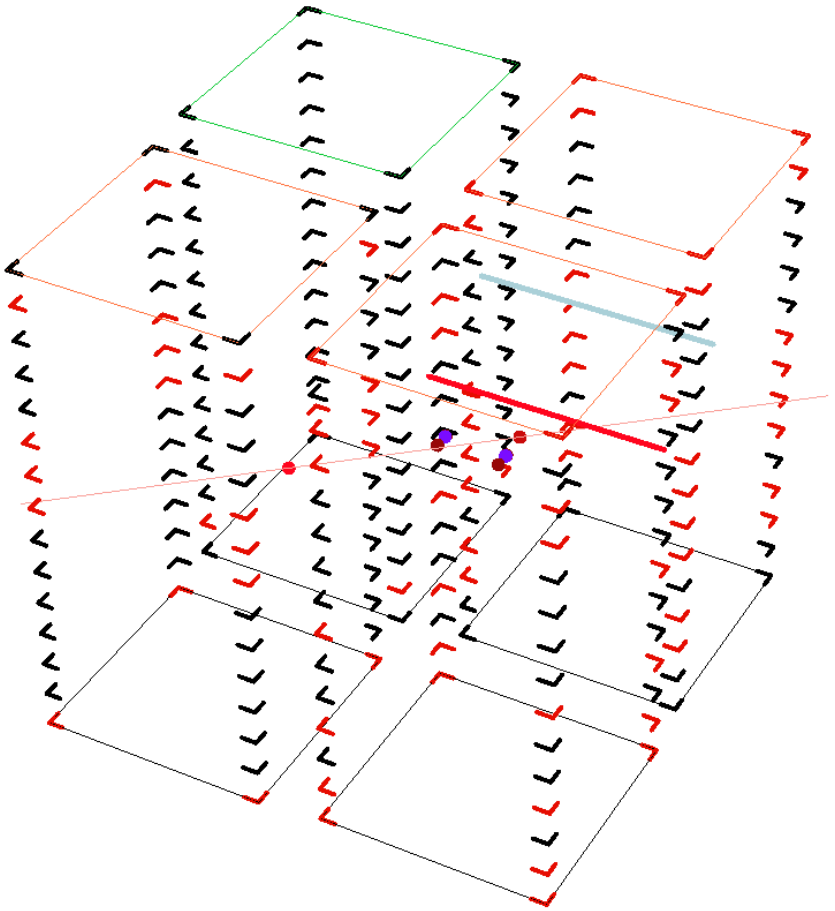

Figure 49 An example of a scattered electron hit. The interaction seen on the left is eliminated.

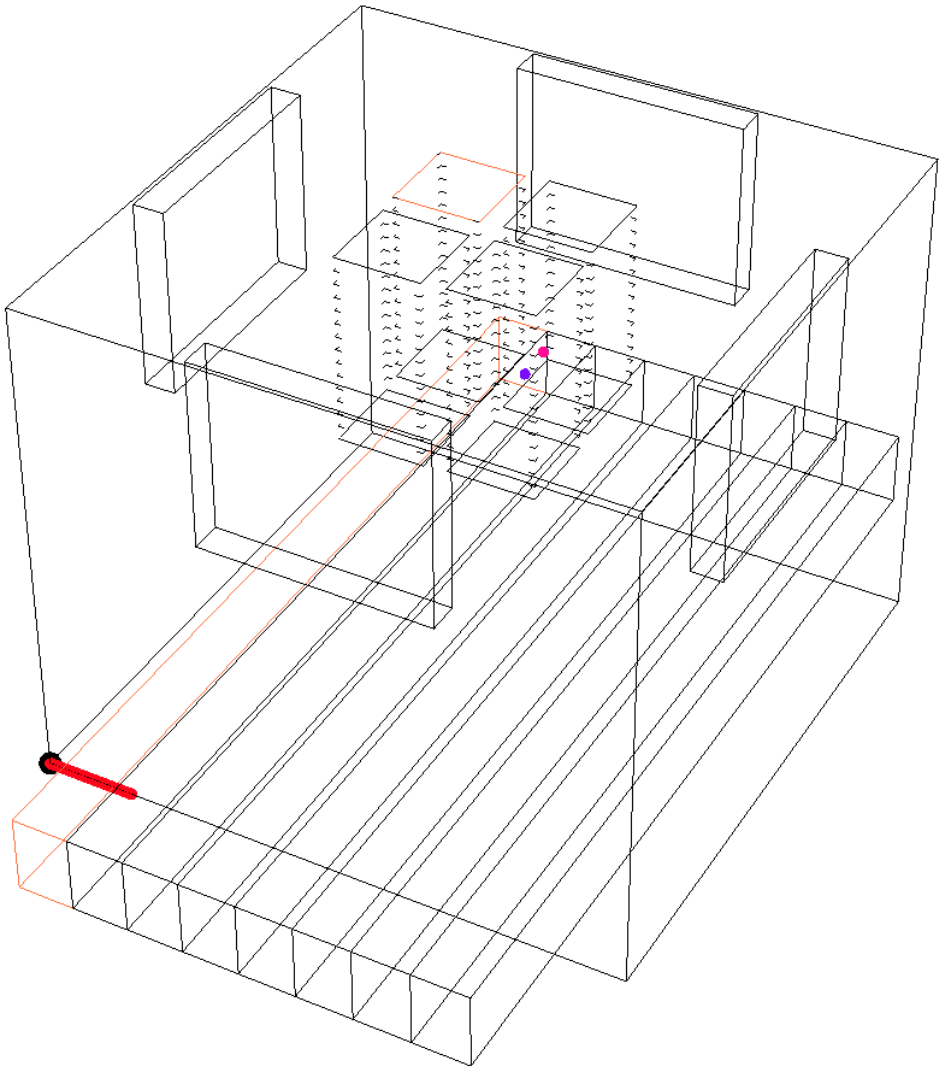

Figure 50 No hit with the Calorimeter was associated with this event.

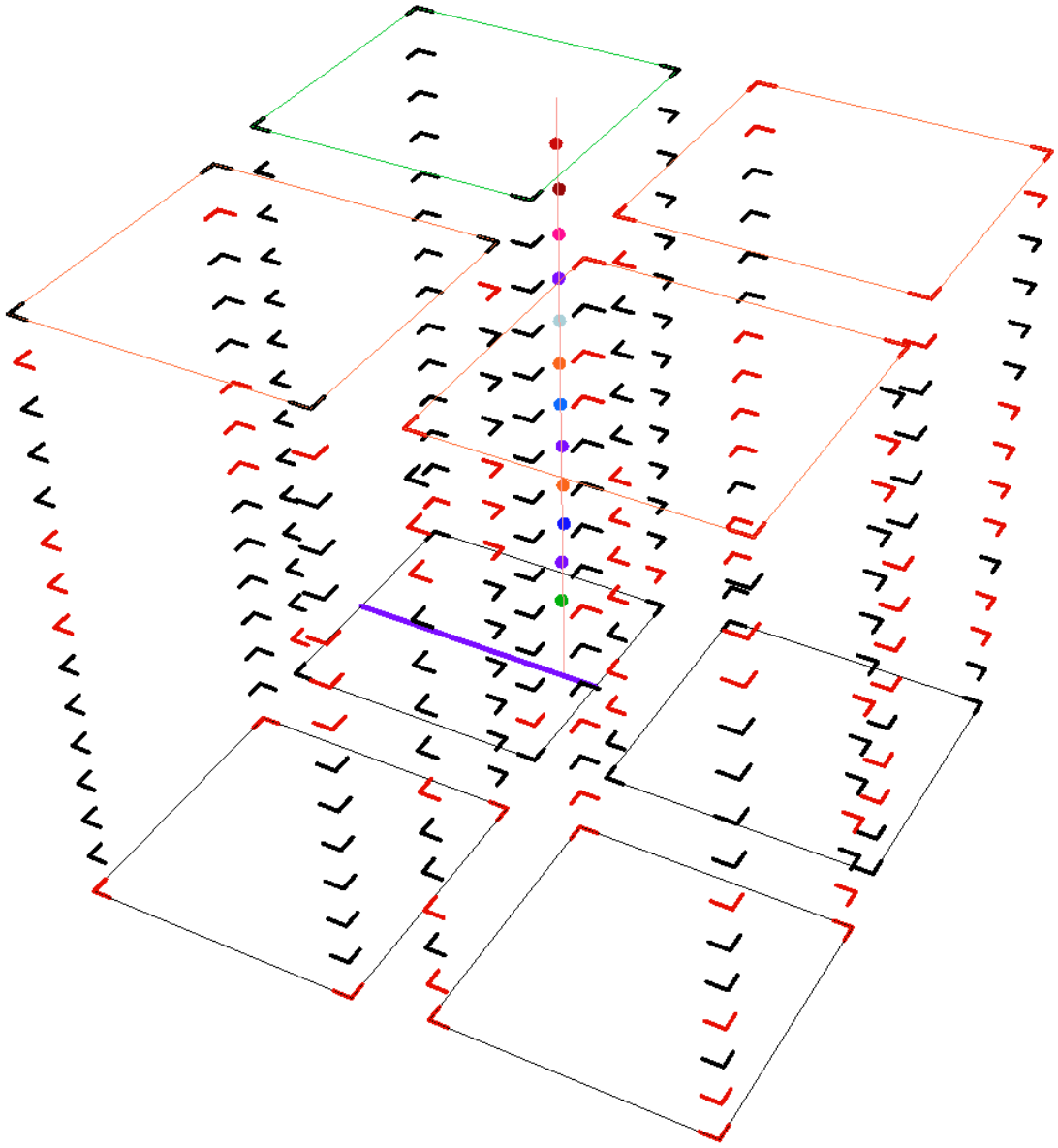

Figure 51 An event with only x or y recorded. Also, since this event begins and ends on the first and last layer, its origin is not within the detector.

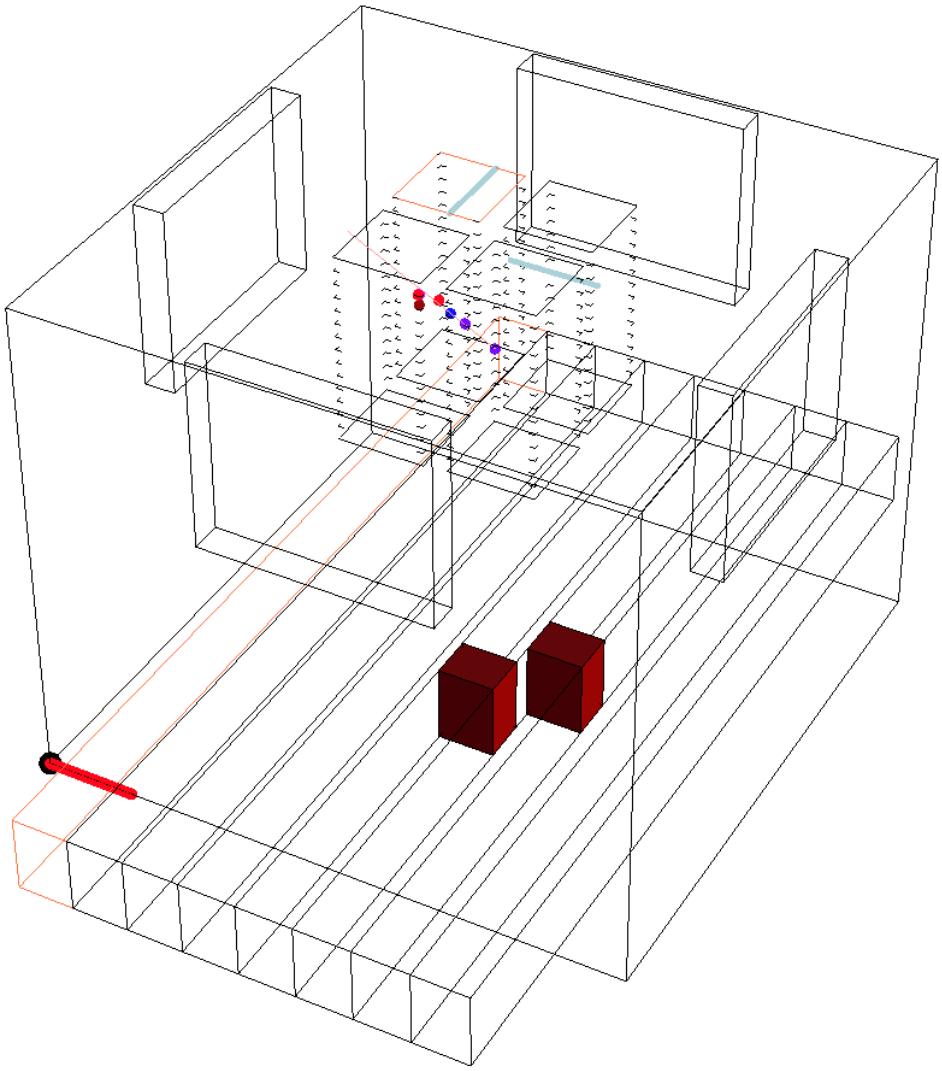

Figure 52 An event with more than 1 Calorimeter reading.

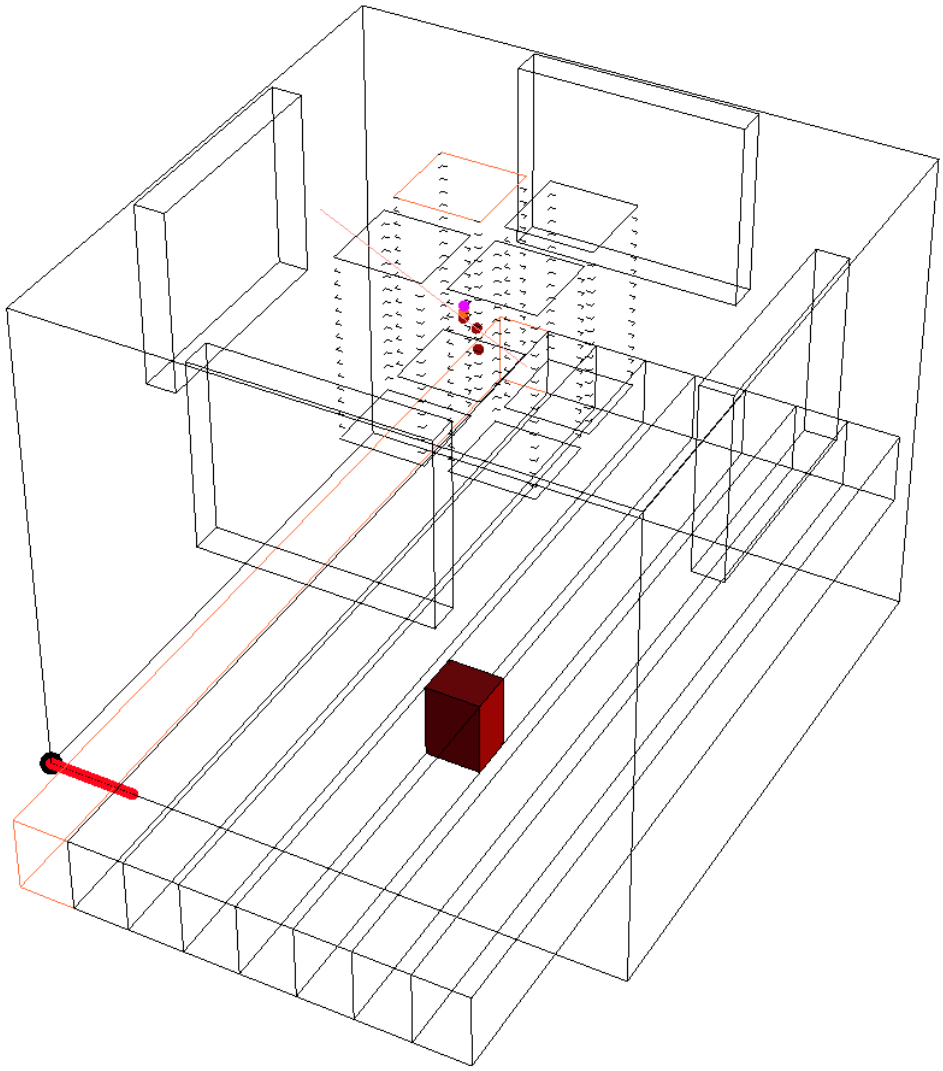

Figure 53 A Compton event candidate.

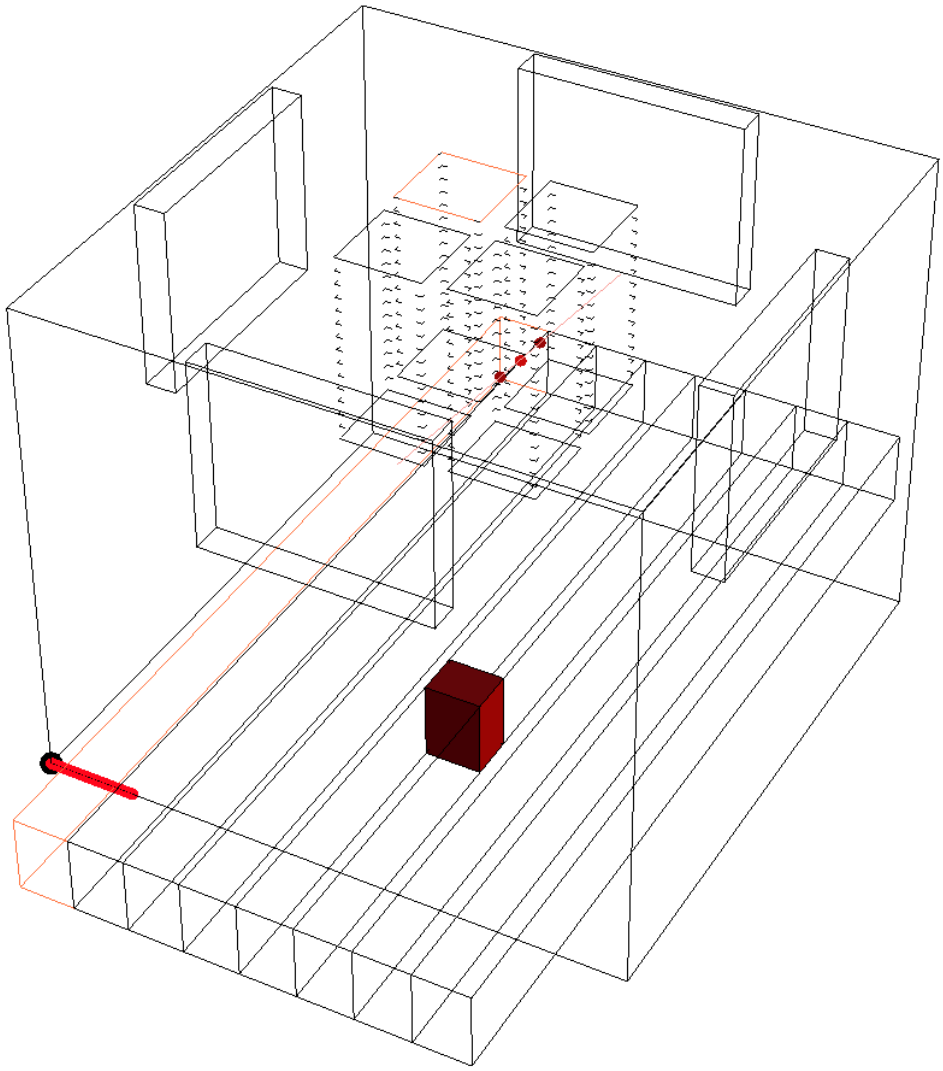

Figure 54 Another Compton event candidate.

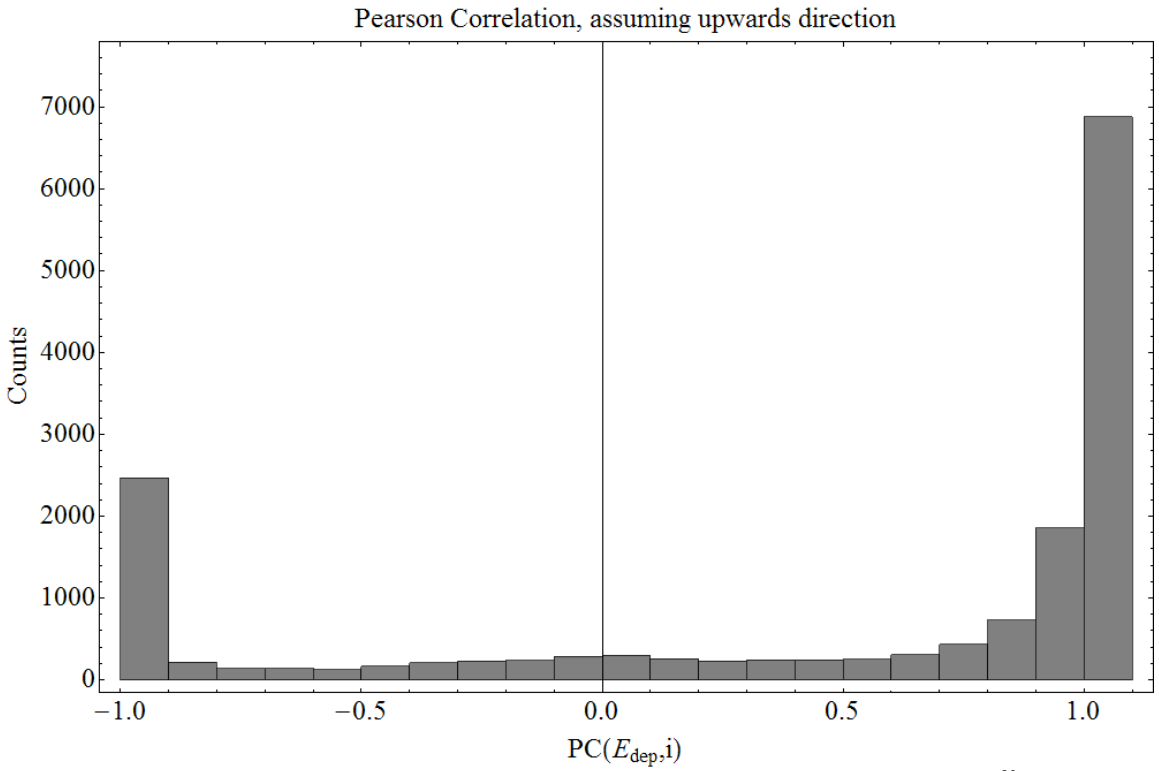

Figure 55 Pearson Correlation assuming all events move upwards. Data taken by positioning the ^{90}Sr below the silicon track, so that all events are in the upward motion. This calculation provided the correct result, showing most events at +1 (upward).

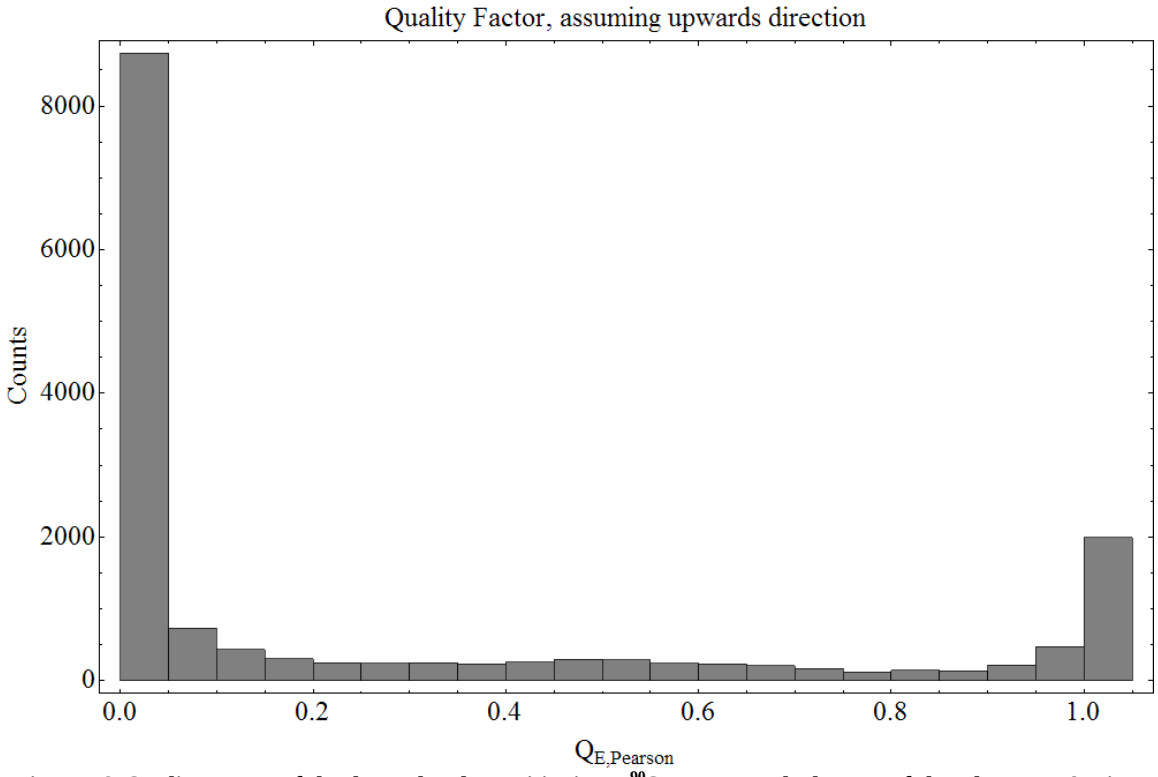

Figure 56 Quality Factor of the data taken by positioning a ^{90}Sr source at the bottom of the telescope. Again, most events are identified correctly, seen by the cluster at 0.

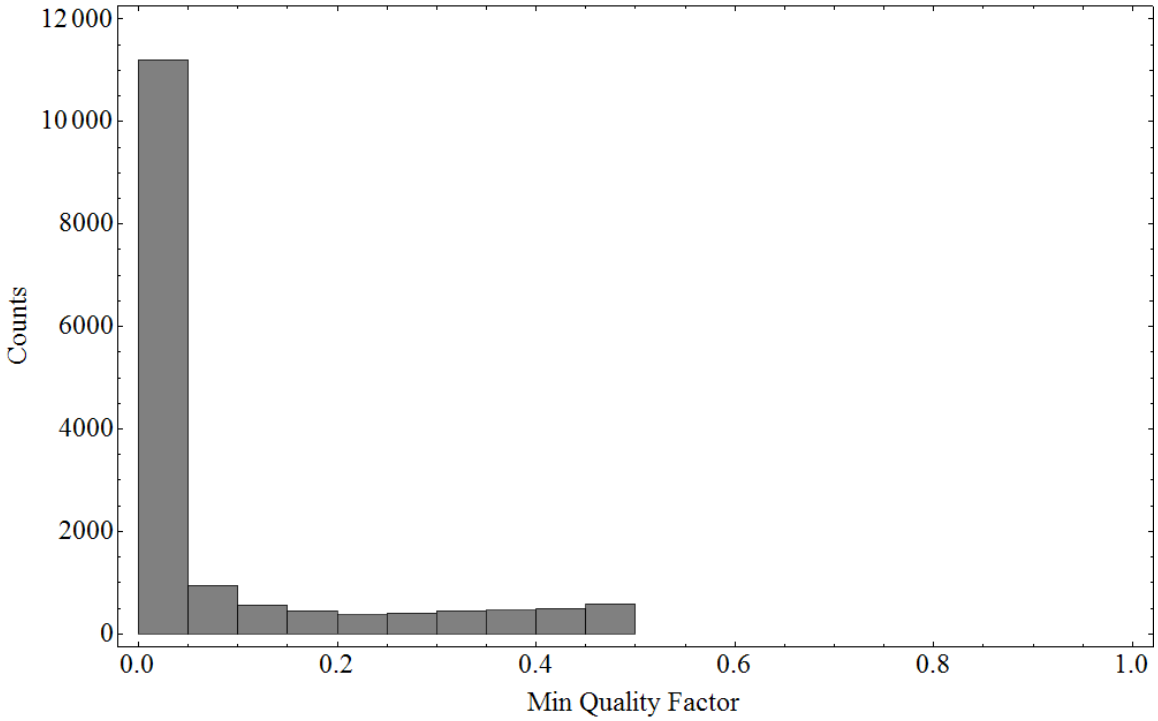

Figure 57 A histogram of the smaller QF of the two assumed direction for the ^{90}Sr tracks. The portion of the correct associated direction gives the % of correctly chosen direction.

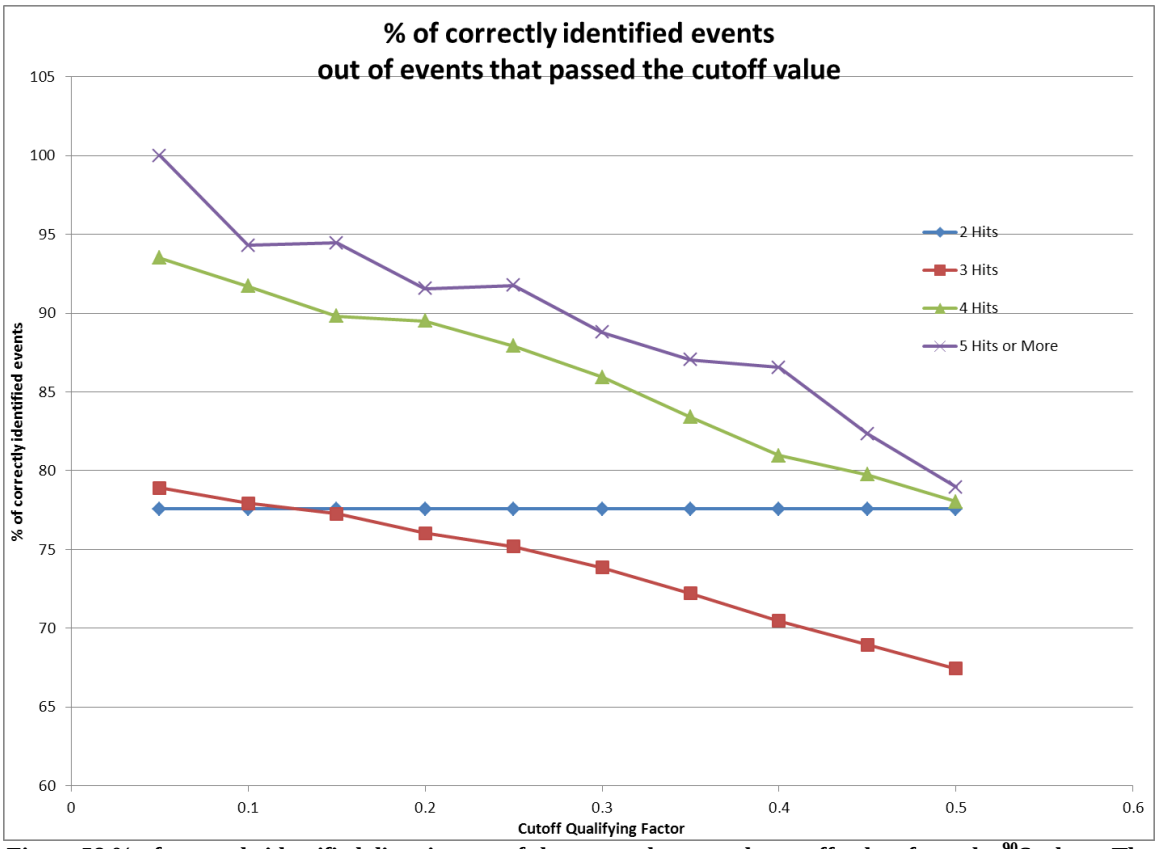

Figure 58 % of correctly identified direction out of the events that pass the cutoff value, from the ^{90}Sr data. The closer the cutoff value is to 0, more event directions are correctly identified. Out of 15,938 total events, there were 8,852 two hits, 6,310 three hits, 624 four hits, and 152 five or more hits. Since the QF for two hits events can only be either 0 or 1, the fraction of correctly identified direction does not change with the QF cutoff value.

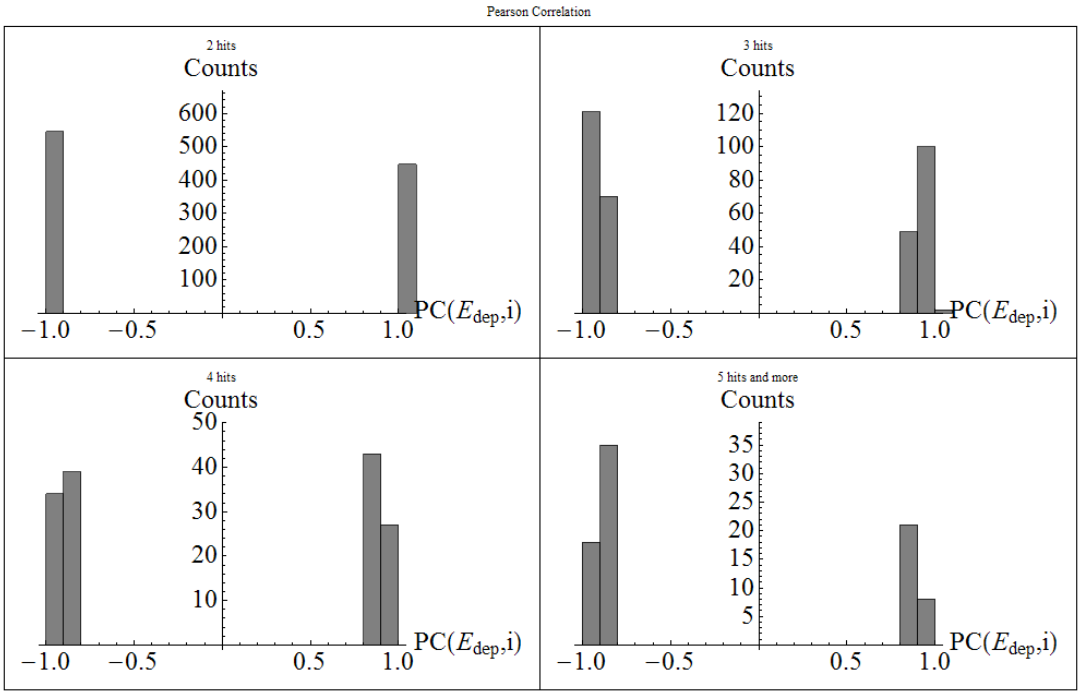

Figure 59 Pearson Correlation applied to flight events, separated by number of electron hits. Only events with QF <= 0.1 was chosen. -1 is upward, and +1 is downward. Except for the 4 hit track, more events correlate with the upward direction.

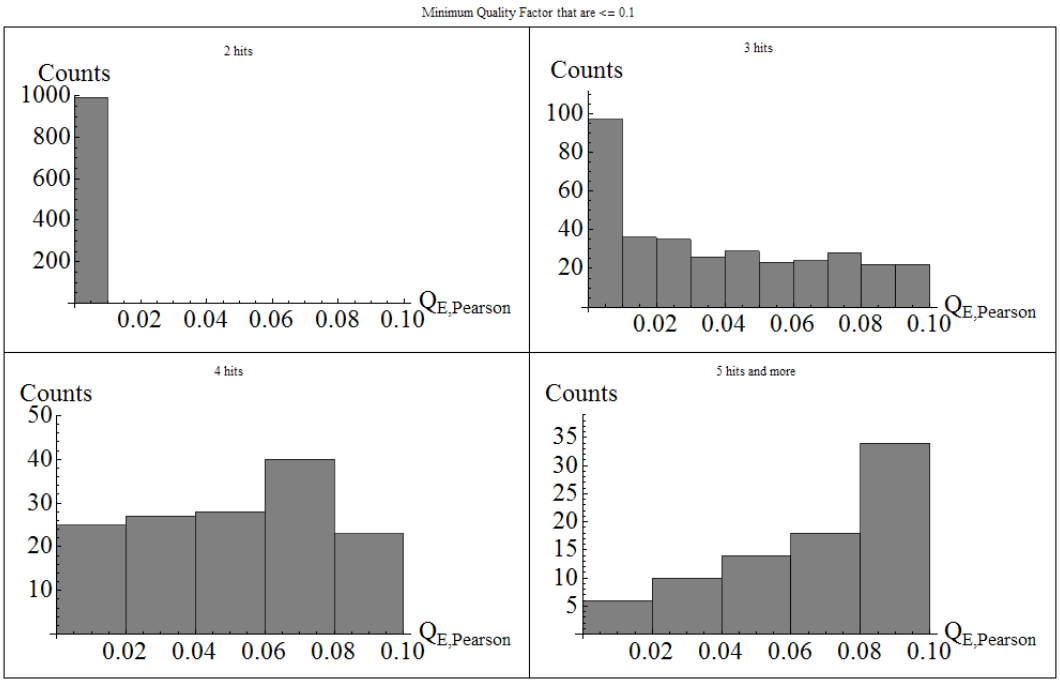

Figure 60 Quality Factor of all events with QF <= 0.1, separated by the number of electron hits. The closer the values are to 0, the more confidence we have that the determined direction is correct.

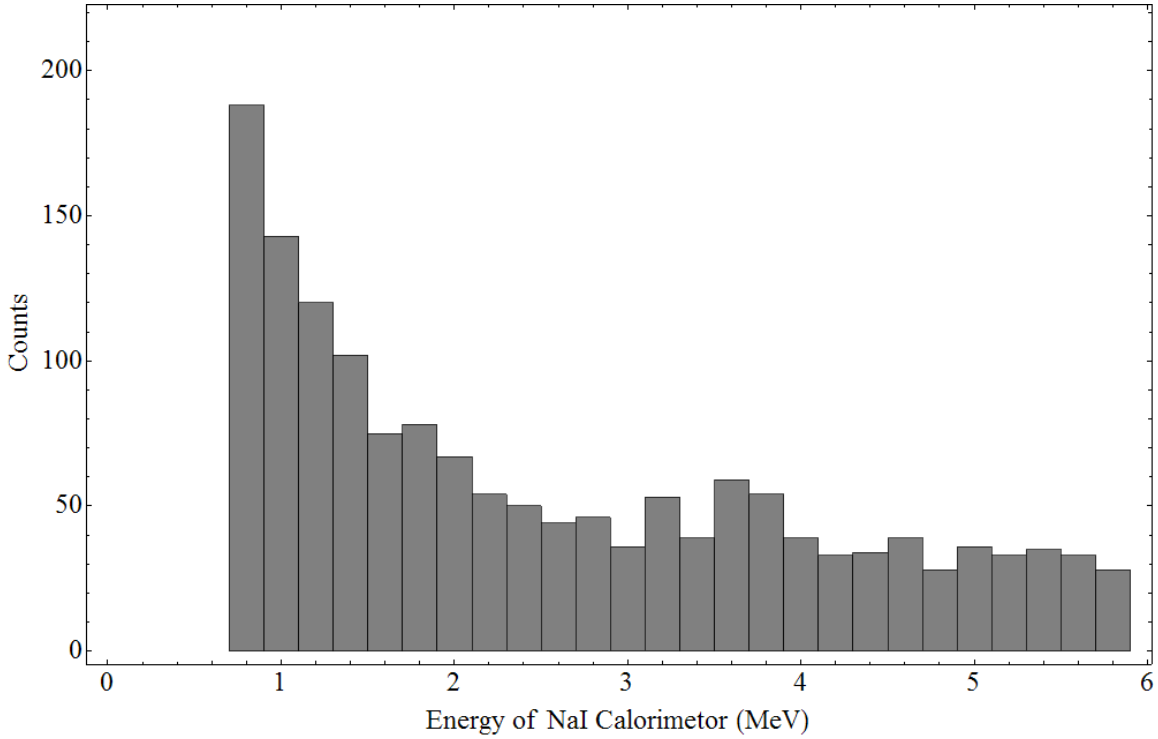

Figure 61 Distribution of the energy of the scattered photon.

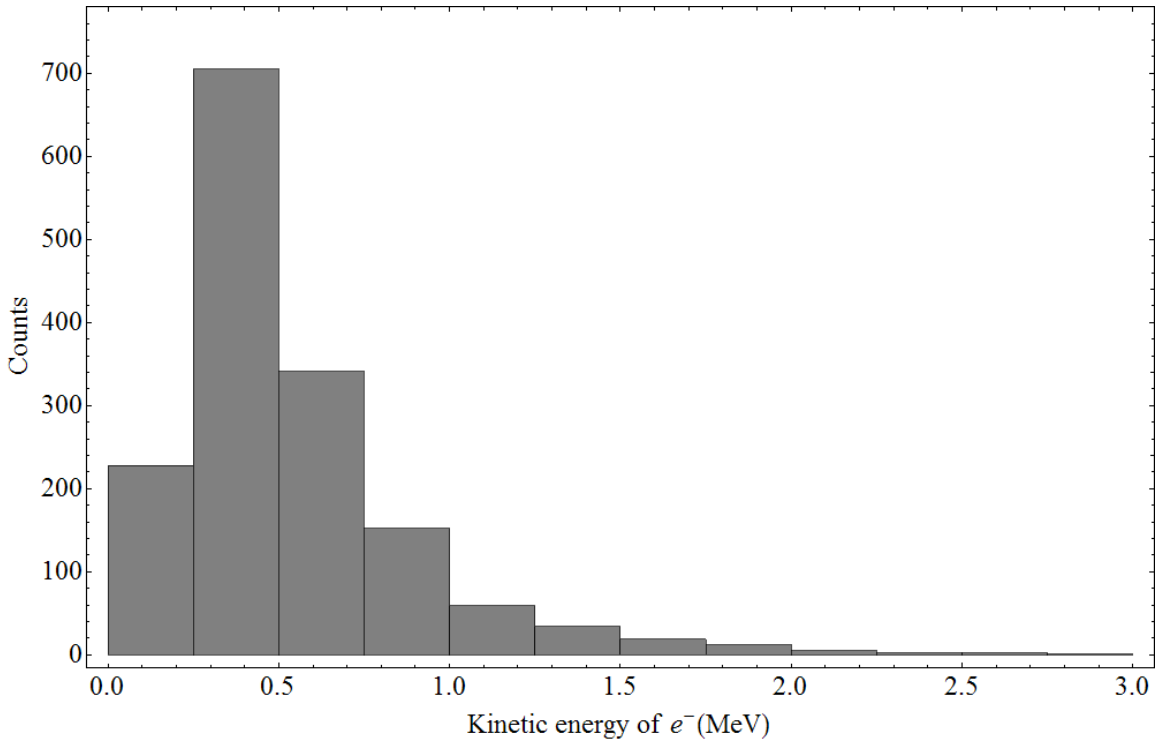

Figure 62 Distribution of the energy of the recoiled electron.

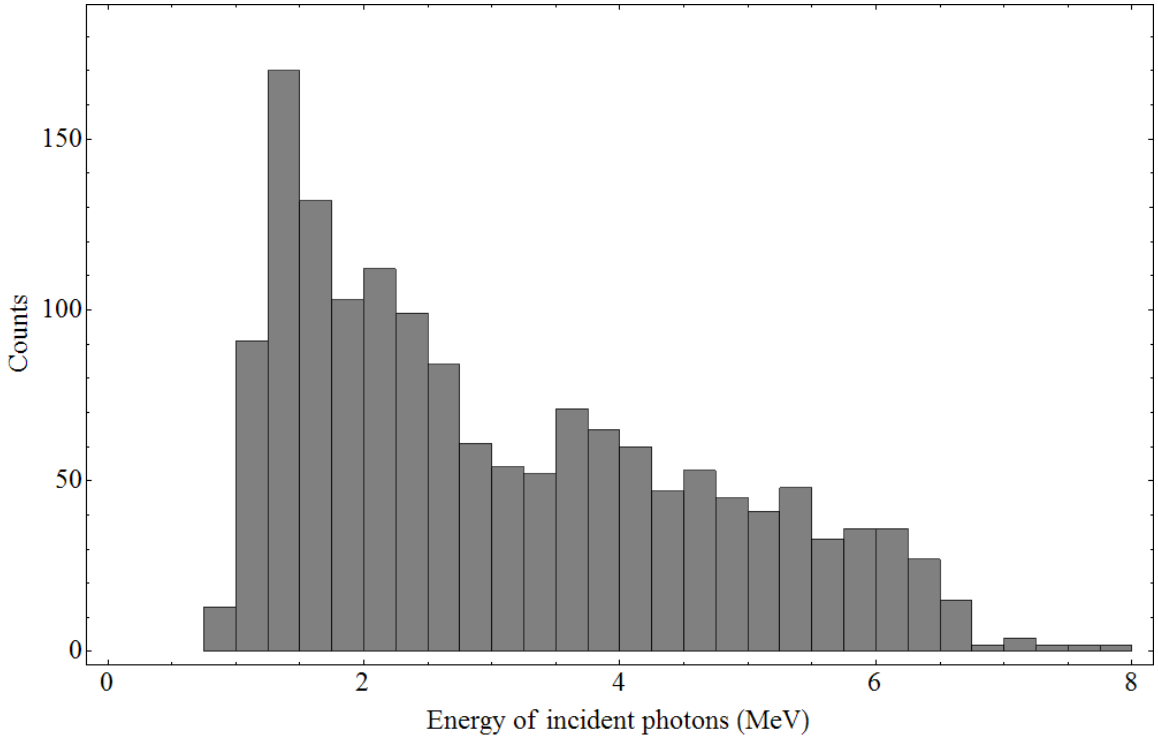

Figure 63 Distribution of the energy of incident photons.

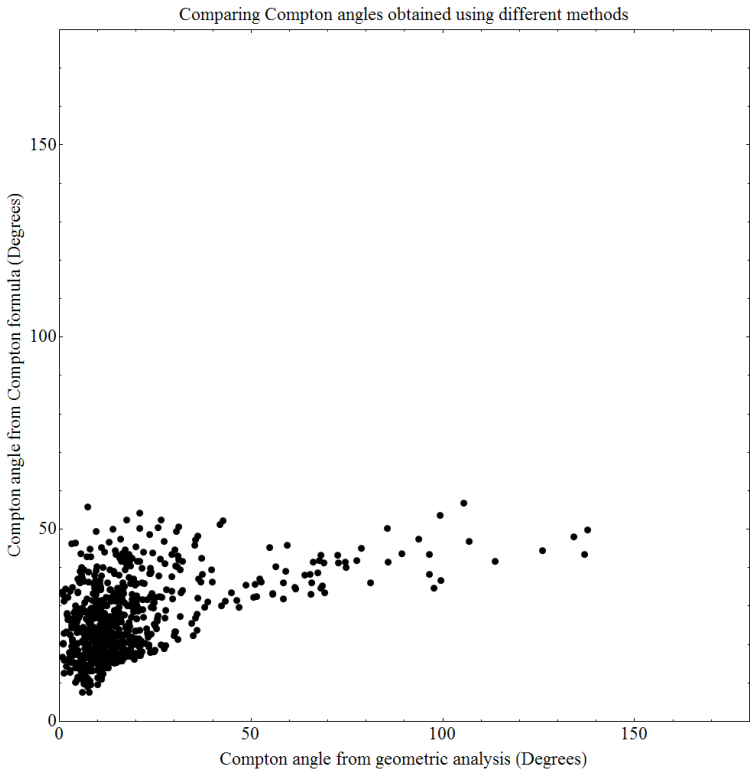

Figure 64 Compton angles calculated from Equation 8 (y axis) compared with the angles between the vectors of the incident photon and the scattered photon (x axis).

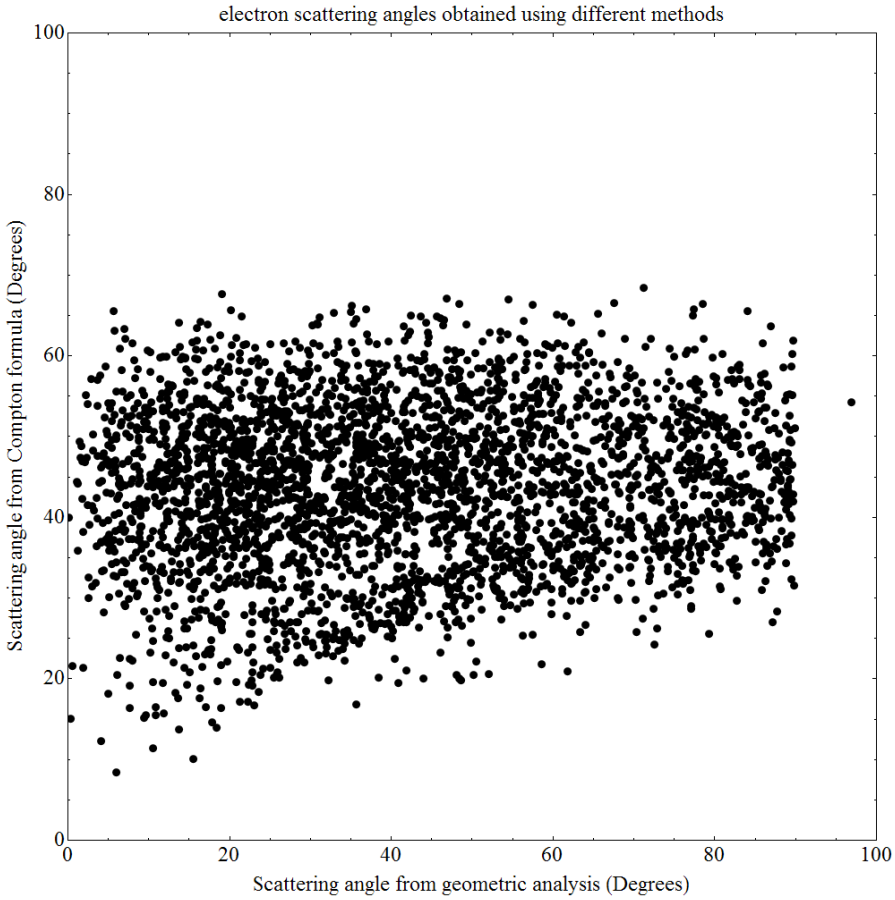

Figure 65 Scattering angle of the recoiled electron, determined by Equation 12 (y axis) and by taking the angles between the vectors of the incident photon and of the direction of the recoiled electron.

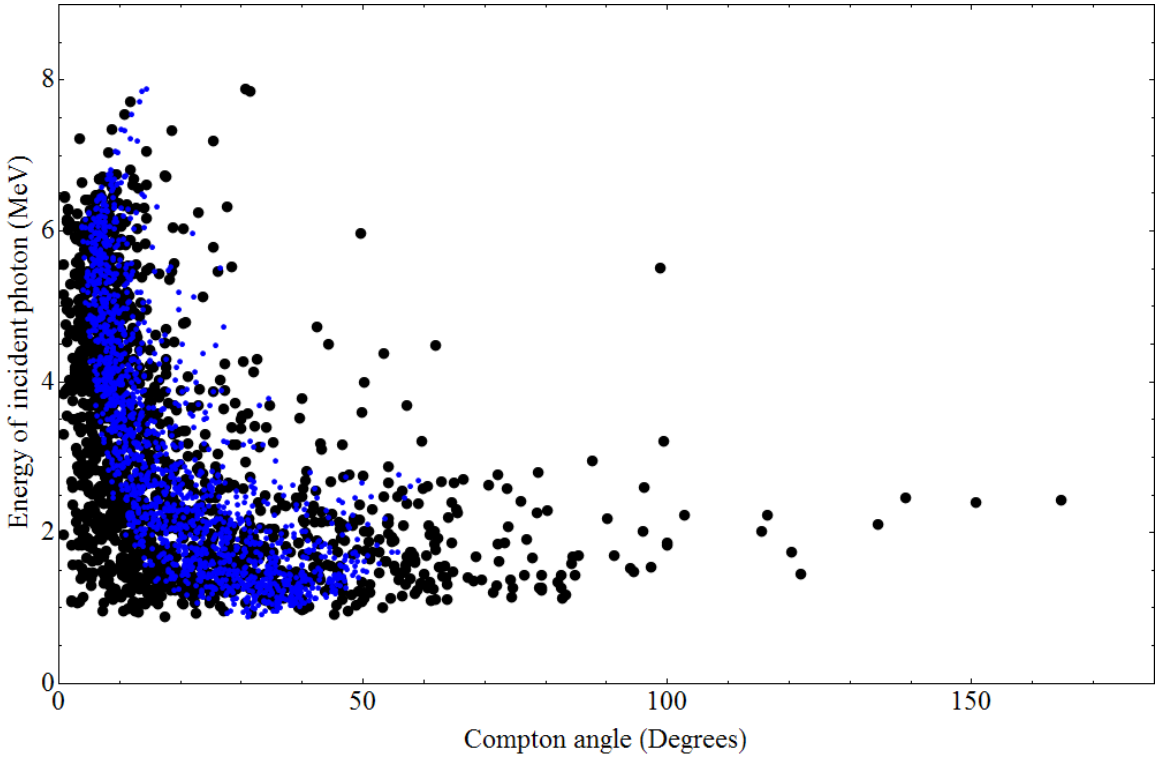

Figure 66 Compton angle (x axis), compared with the energy of the incident photon (y axis). Superimposed are the Compton angle determined by the angle between the vectors of the scattered photon and the incident photon (black) and the Compton angle determined from Equation 8 (blue).

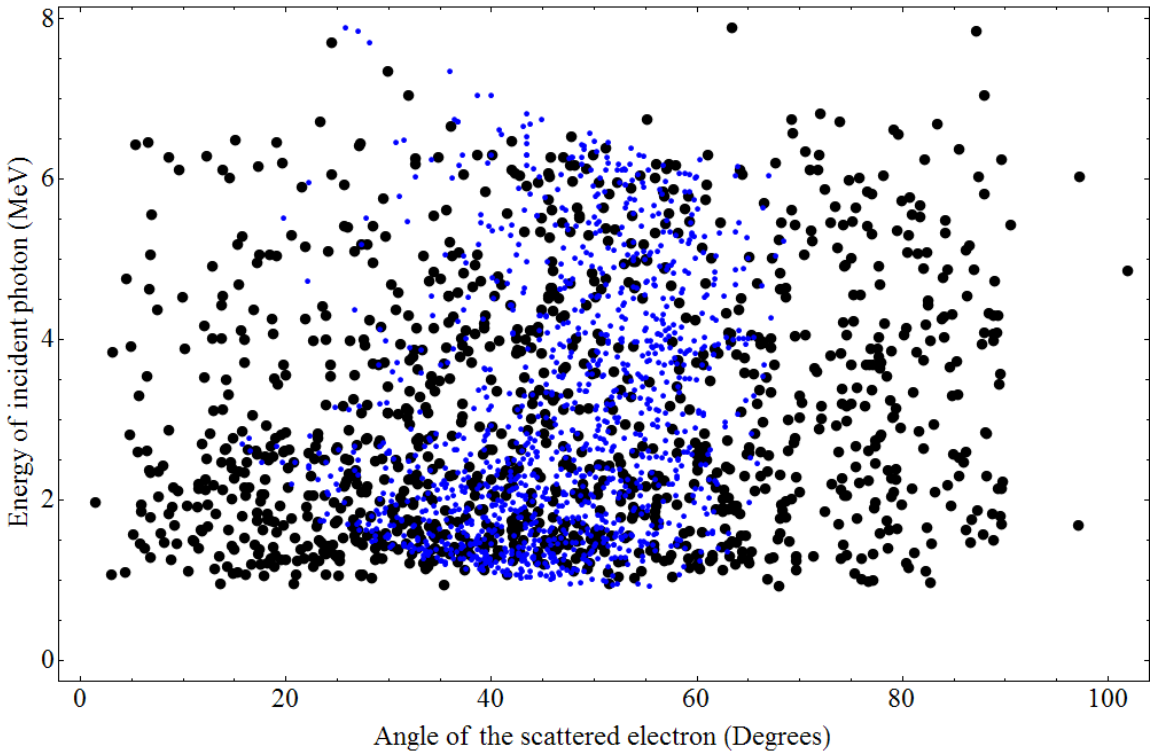

Figure 67 Scattering angle of the electron (x axis) compared with the energy of the incident photon (y axis). Superimposed are the scattering angle determined by the angle between the vectors of the scattered photon and the incident photon (black) and the scattering angle determined from Equation 12 (blue).

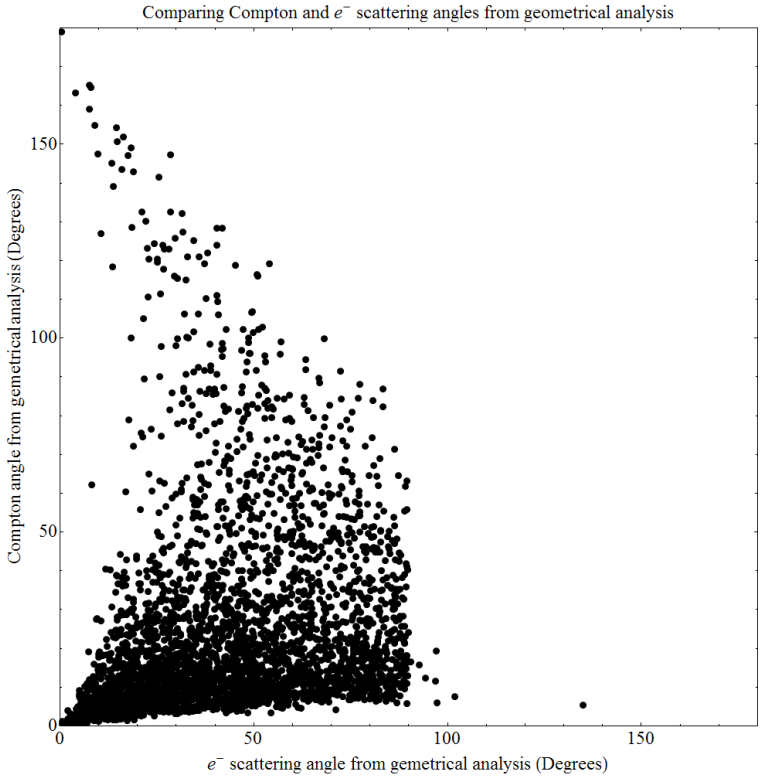

Figure 68 The scattered photon angle and the recoiled electron angle, calculated by using equations from page 109.

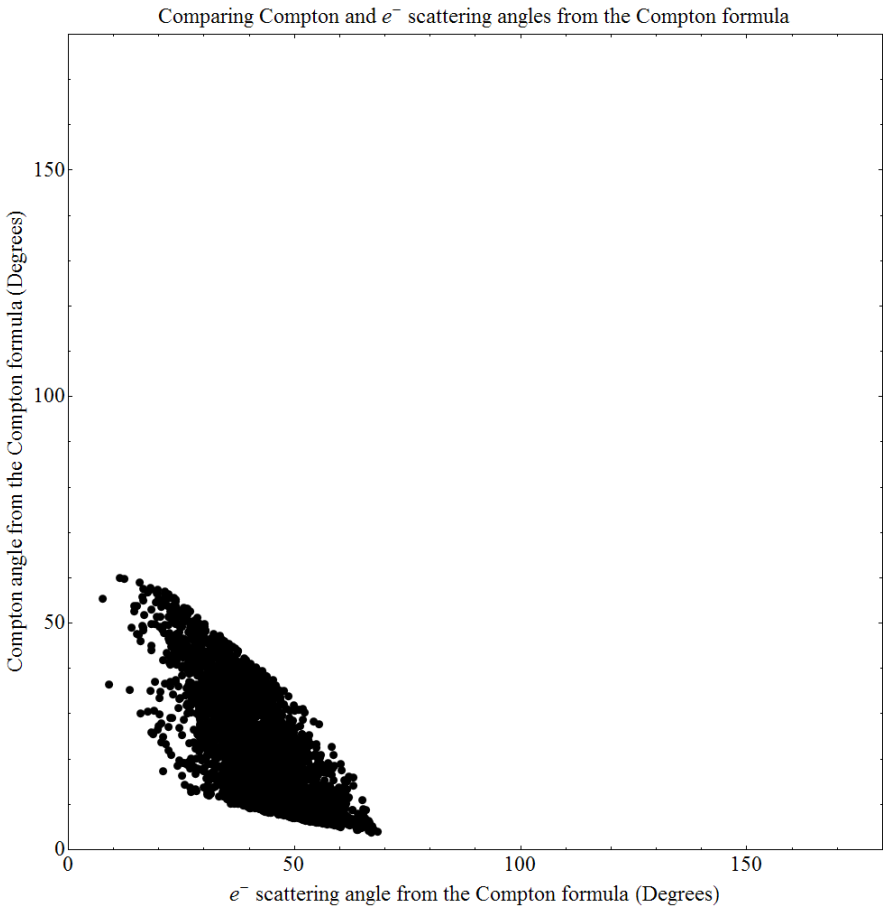

Figure 69 The scattered photon angle and the recoiled electron angle, calculated using Equation 8 and Equation 12.

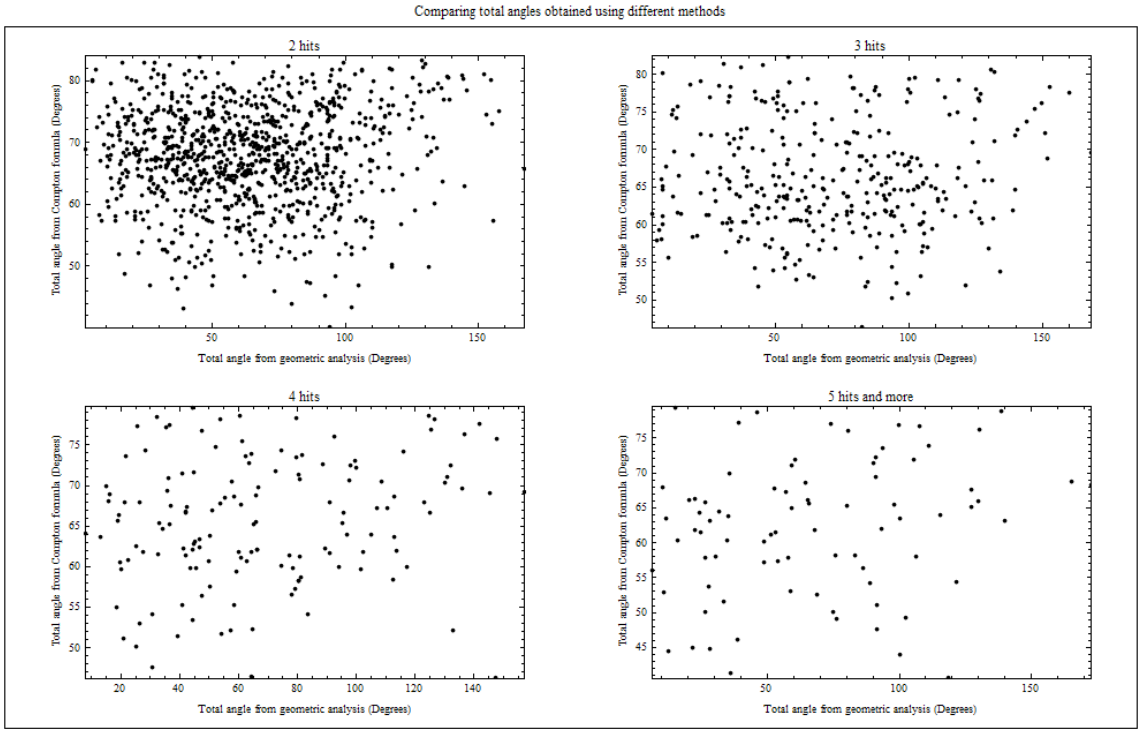

Figure 70 Total angle from adding the results of Equation 8 and Equation 12, compared with the total angle obtained from the vectors of the scattered photon and the recoiled electron. Results are separated by electron track length. Two electron hits in an event, three hits, four hits and then five or more hits from the top left, top right, bottom left and bottom right, respectively.

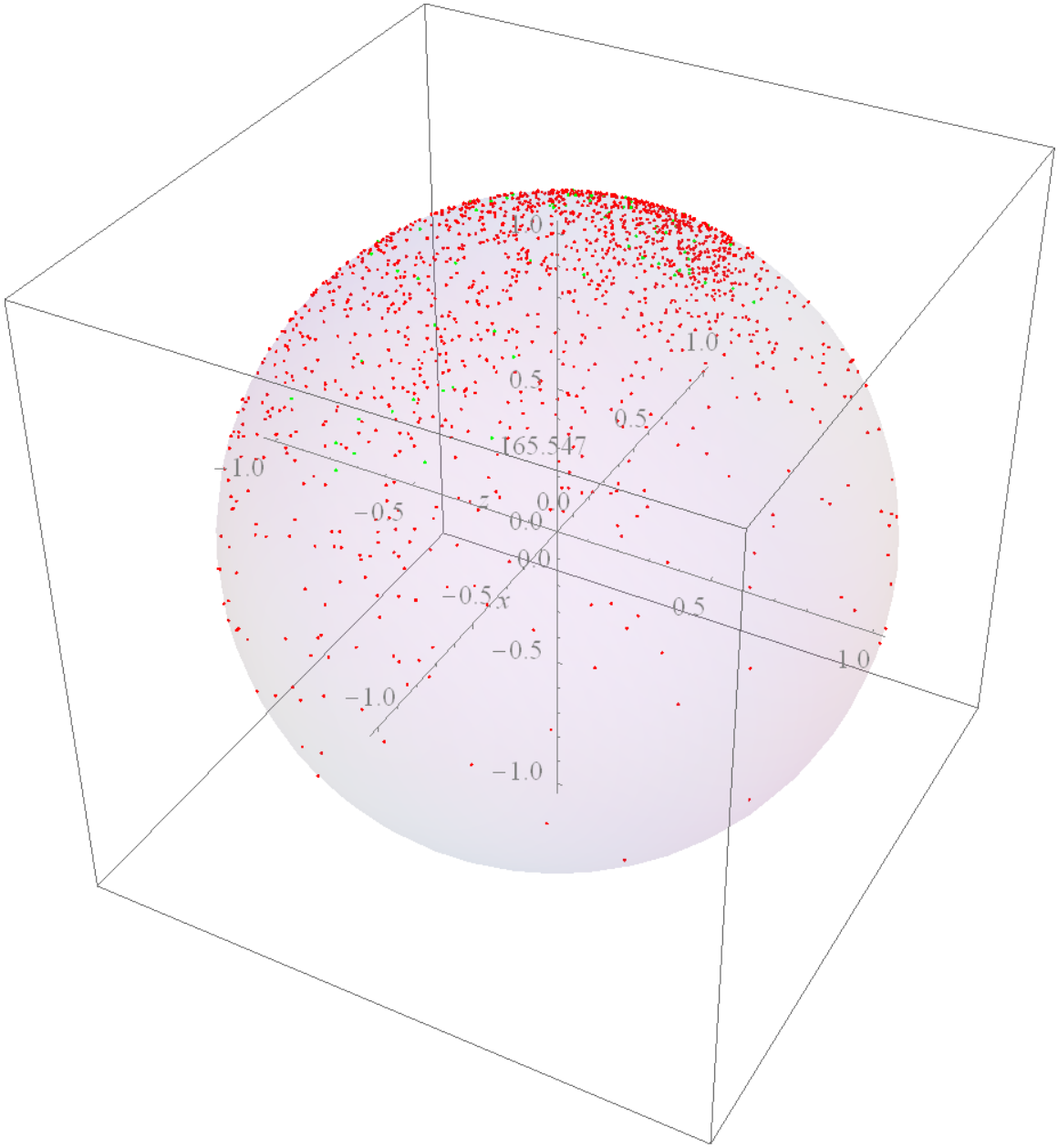

Figure 71 Sky map of incident photons expressed as points on a unit sphere. The reds are incident photons with energy < 6 MeV, Greens are between 6 MeV and 10 MeV, and the blue is above 10 MeV.

Chapter 9 Calibration comparison, pulsar timing, and Conclusions

The absence of correlation between the Compton angle determined by geometric considerations and the Compton angle determined by the Compton formula shown in Figure 64 was unexpected. To gain further insight to the telescope performance during flight, this result was compared using the ^{88}Y simulation data described in page 83. The analysis of this data was performed after the instrument was returned to UCR.

A. Comparing flight result with ^{88}Y calibration result

The radioisotope ^{88}Y emits two gamma-rays (0.9 and 1.8 MeV) in cascade but their directions are essentially uncorrelated. So it is possible that one photon may scatter in the silicon detector and the second photon can interact in the NaI array, giving rise to a coincidence event but not a true Compton scatter event. However, it is expected that of the ^{88}Y events, there should be sufficient Compton events to be identified.

The calibration events were not subject to filters described in page 95. All silicon and NaI bar pulse heights and positions were recorded and converted to energy. The energy spectrum for the NaI bars is shown in Figure 72. This shows the two peaks at the energies originating from the source, comparable to Figure 40. The electron energy histogram is shown in Figure 73, separated by its track hits. The peak energy increases with track length, showing longer tracks with higher kinetic energy. The silicon track histogram figure shows the expected energy deposit from tracking electrons, and the NaI bar energy histogram shows that the ^{88}Y source is clearly being detected.

Using the known position of the source, the electron hit location, and the NaI bar hit location, the true Compton angle can be determined. The deposit energies of the electrons in the silicon stack and the recorded energy in the NaI bar will give the energy of the incident photon. All the electron tracks should be downward. Using Equation 8, the energies will give the measured Compton angle. These values can be used to calculate the ARM (Angular Resolution Measure), which is defined as

$$\text{ARM} = \theta_{measure} - \theta_{true}$$

Only silicon hit positions and energies in the first tower were used, to match the flight conditions. Silicon layers with one and only one reading in both junction and ohmic side were converted to detector coordinates. All energy readings on the junction side were added to find the kinetic energy of the recoiled electron. Only events with NaI recordings were used in order to calculate Compton angles. A histogram of the ARM is shown in Figure 74. The peak at the center shows most events have minimal deviation from the true Compton angle. However, when comparing the Compton angles separately, Figure 75 shows little correlation between the measured and true Compton angle. This figure is similar to the result in Figure 64. The disassociation between the true Compton angle and the measured Compton angle in both the ^{88}Y simulation data and the flight data shows that the pulse height in the silicon stack is not related to the pulse height in the NaI calorimeter bars. The non-correlation between the silicon track and NaI is also evidenced by the many events with zero or off-scale NaI pulse heights.

The reason for the non-correlation is because the event coincidence time overlap window was too large and had too much time jitters. The slow triggers from the CsI-PD

arrays compared to the charged particle shield, silicon and NaI-PMT detectors required a wide (8 μs) delayed coincidence overlaps. Even without many CsI detector events due to their high energy threshold, the wide coincidence overlap window degraded the performance of charged particle shield for unwanted cosmic ray particles and, most likely, produced unreliable performance in the CAMAC ADC hardwired "reset" generator. This "reset" feature was needed to clear the ADCs of unwanted events. As a consequence, accounting for all the expected Compton events has proved very difficult, especially when the electron track events were unrelated to the recoiled NaI interactions. Also, as mentioned in page 99, that the NaI ADC modules were reset every 5.12 ms by accidental line of code that was not removed for the flight program. These two faults caused the non-correlation in the results.

B. Pulsar Timing Analysis

The Crab Nebula and Pulsar were within the telescope's field-of-view when the balloon initially exceeded 120,000 ft. at 16:24 UTC, the minimum altitude for optimum observations. After 22:21 UTC the zenith angle of the Crab exceeded 60^{o}. We have selected the *full* event data set from 16:30-21:00 UTC for preliminary analysis, without any event selection based on the direction of origin of these events. While this represents the worst possible case (i.e., lowest signal-to-noise ratio) for detecting pulsed emission from the Crab pulsar, we did this to demonstrate the methodology and expected telescope timing accuracy.

Each event time as recorded by the telescope's on-board double oven crystal oscillator/clock must be corrected to Barycenter Dynamical Time (TDB) before the event arrival times can be folded with the known Crab pulsar ephemeris parameters. The telescope event time is read from the on-board clock in hours, minutes and seconds to 0.1 μs precision. The on-board oscillator/clock was started just prior to the balloon flight with a 1-minute pulse from a Rb oscillator/clock which was part of our ground support equipment (GSE). The Rb oscillator/clock was used as matter of convenience and to provide redundancy. UTC (accurate to 300 ns) was provided by our GPS clock. The drift of the Rb oscillator/clock (~1.0×10^{-10} s/s) was monitored for almost 2 months by comparing 1 PPS (pulse per second) signals from both units, using a frequency counter in the time interval mode. When the telescope clock was started at 03:49:00 UTC on 06/02/2007 the Rb 1 PPS was delayed by 444.4 μs with respect to the GPS 1 PPS.

The 1 PPS from the on-board clock was downlinked during the balloon flight via a standard IRIG TM channel with ~1 ms risetime for comparison with the stationary GPS clock. The time difference could be measured with ~10 μs accuracy. Using the calculated line-of-sight delay, determined from the varying GPS position (latitude, longitude and altitude) of the balloon during the flight, and the fixed TM downlink delay (782.1 μs) the correction of the on-board telescope clock to UTC was found for each event. This correction is shown as a function of on-board time in Figure 76. The drift of the on-board clock was $+3.05 \times 10^{-9}$ s/s.

Another correction to the event time is the subtraction of the pulsar wave front travel time (Roemer Delay) from the Solar System Barycenter (SSB) to the balloon and

telescope. This time depends on the direction of the pulsar (RA, Dec) and the instantaneous direction and distance of the barycenter from the telescope. We used JPL's On-Line "HORIZONS" Ephemeris System to compute the direction (RA, Dec) and distance of the SSB using the balloon's GPS latitude, longitude and altitude every ½ hour during the exposure to the Crab pulsar. This propagation delay was approximately 491 s for our observation. The precise value needed to be subtracted from each event time. Since the HORIZONS Ephemeris provided apparent parameters for the SSB that take into account the light travel time from the SSB to the observer (telescope) of about 503 s, the rates of change of the SSB parameters, also provided by the HORIZON system, were used to recalculate its direction and distance, allowing for the ~12 s (503 s – 491 s) of motion of the SSB. This added about 254 μs to the Crab pulsar travel time from the SSB to the telescope. Interpolation between the 1/2-hour intervals provided corrections, accurate to ± 50 μs.

A third time correction is the conversion of all the telescope event times in UTC to TDB. This includes the conversion to International Atomic Time (TAI) with the addition of 33 leap seconds, the conversion to Terrestrial Dynamic Time (TDT) with the addition of 32.184000 s, and the conversion of TDT to TDB due to relativity effects. The largest contribution to this last conversion is the *Einstein delay* (Lorimer & Kramer, 2004) due to time dilation from the Earth's motion and gravitational redshift due to the other solar system bodies. This time adjustment depends on the Julian Day of the observations. Using the expression from the *2007 Astronomical Almanac* (Nautical Almanac Office, 2005) this varied from +0.00889 s to + 0.000874 s during our

observation. The last adjustment to consider is the *Shapiro delay* (Lyne & Graham-Smith, 2006) due to the gravitation potential of the Sun. The Crab Nebula/Pulsar was ~ 12.5^{o} from the Sun and the calculated correction was - 0.000037 s.

All TDB event times were converted to Modified Julian Date (MJD) so that the phase of the event arrival time could be determined. The data ($\nu, \dot{\nu}$ *and* t_o) from the Jodrell Bank Crab Pulsar Monthly Timing Ephemeris were used (Lyne, Pritchard, & Smith, 1993). The number of pulsar rotations (phase) was found from where the event time, *t*, and the epoch time of the main Crab pulse, t_o, are in units of MJD. Figure 77 shows the very preliminary phase histogram (modulo of rotations) for all the event times for the Crab pulsar observation. While there is some evidence of structure in this phase diagram, at MeV energies the known Crab pulsar light curve is relatively complex with a more prominent 2nd peak and a substantial interpulse contribution.

C. Conclusions

This thesis describes the first exposure of the TIGRE prototype instrument to the near space environment of a balloon flight. The silicon detectors, CsI and NaI calorimeters, and the ASIC chips were designed for optimal detection of Compton events in the gamma-ray spectrum. Each component was assembled and tested at UC Riverside. Preliminary simulation with an advanced TIGRE design for ULDBF showed that an angular resolution for a Crab-like source is 1.7° and an effective area of 80 cm^2 are possible. Using MEGAlib, the expected number of Compton events in 5 hours of conventional balloon flight time was 1.31 events/second, or 24,102. From a Crab-like

source, MEGAlib predicted 74 Compton events. TIGRE had its first balloon flight on 02 June, 2007. It was in float for over 27 hours.

The initial events of approximately 18,436 seconds (over 5 hours) in tracked mode were used for analysis. This mode clearly showed the operational electron tracking feature of TIGRE. The Pearson Correlation was used to determine the direction of the electron tracks. The method was tested by using data collected by placing a ^{90}Sr source beneath the telescope and correctly identified the upward direction of the electron tracks in most events. By applying a cutoff value to the Quality Factor, the correct DOM can be determined with a minimum of 78% accuracy. After applying this method and the criteria for searching Compton events to the flight data, the total number of Compton candidates was 1,560. The low Compton event yield was because much of the detector was not operational. The unused detectors were 5 out of 8 NaI bars, 3 stacks of Si electron track towers, and all of the CsI calorimeters. After turning off these components in the mass model in MEGAlib, the expected Compton events detected was reduced from 24,102 to 1,781 events, closely matching the actual performance within the statistical error.

Using the electron tracks, the Compton angle was determined by the angle between the reconstructed incident photon and the scattered photon. This Compton angle and the Compton angle determined using the Compton formula did not show the expected direct correlation. This revealed several flaws in the triggering electronics. The incompatibility of the ASIC chips on the CsI(T1) calorimeter and the timing settings of the NaI calorimeter made most of the coincidence pulse heights unreliable to determine

Compton events. Furthermore, it was discovered in the post-flight analysis that the NaI pulse height registers were unintentionally reset every 5.12 ms, along with the burst count registers. These flaws and the high charged particle background in space combined to leave many events without NaI coincidence and limited the analysis presented here to electron tracks. Presumably the tracks were due to Compton scatter events but the complete Compton event reconstruction could not confirm this. In the ^{88}Y calibration data, the electron tracks and NaI pulse heights showed no apparent correlation, much like the results from the flight events. This is due to the overly large overlap of the event coincidence time and the accidental inclusion of the reset code of the NaI ADC modules.

Updated circuit designs and new NaI bars would improve the likelihood of finding events. TIGRE was taken to Australia in March 2010 with its updated components for a second flight. Future projects include searching in the Australia data for Compton events.

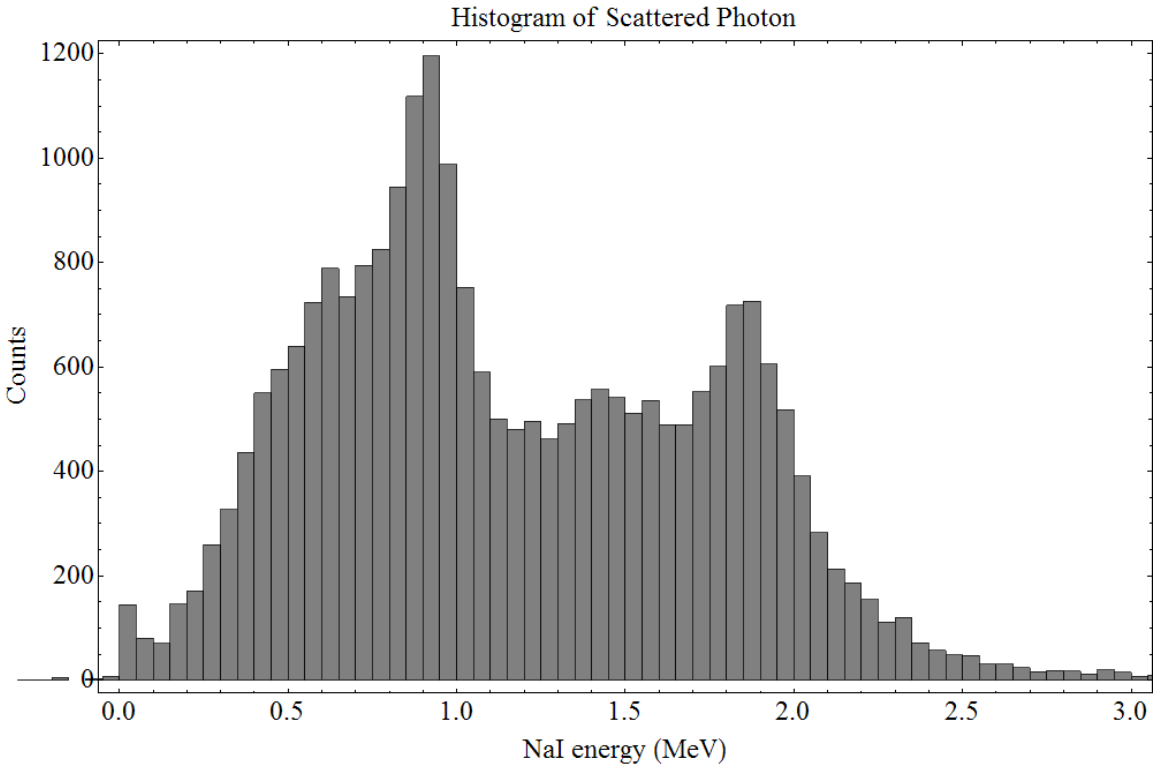

Figure 72 Histogram of the NaI bar energy readings from ^{88}Y source. The two ^{88}Y energies, 0.9 MeV and 1.836 MeV are clearly detected.

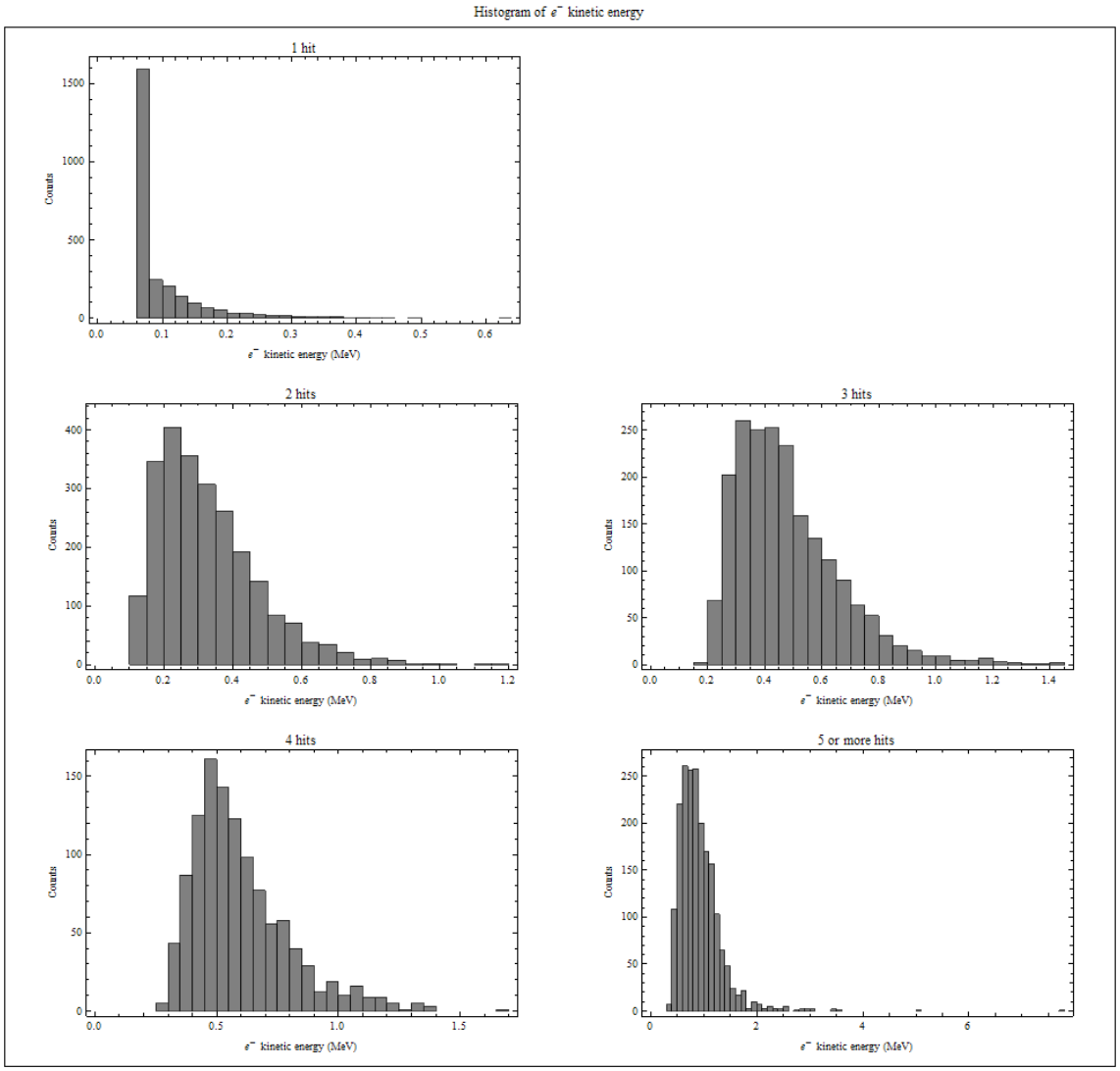

Figure 73 Recoiled electron energy, separated by number of track hits. The peak energy increases with track length.

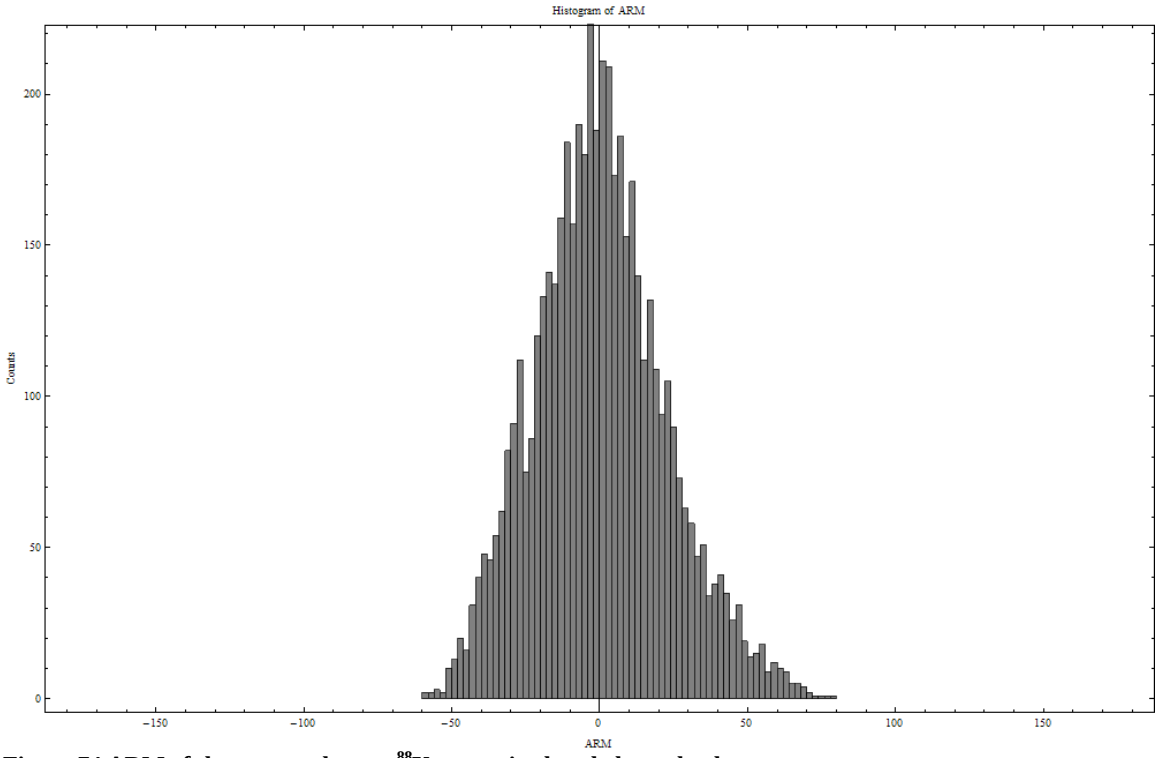

Figure 74 ARM of the events when an ^{88}Y source is placed above the detector.

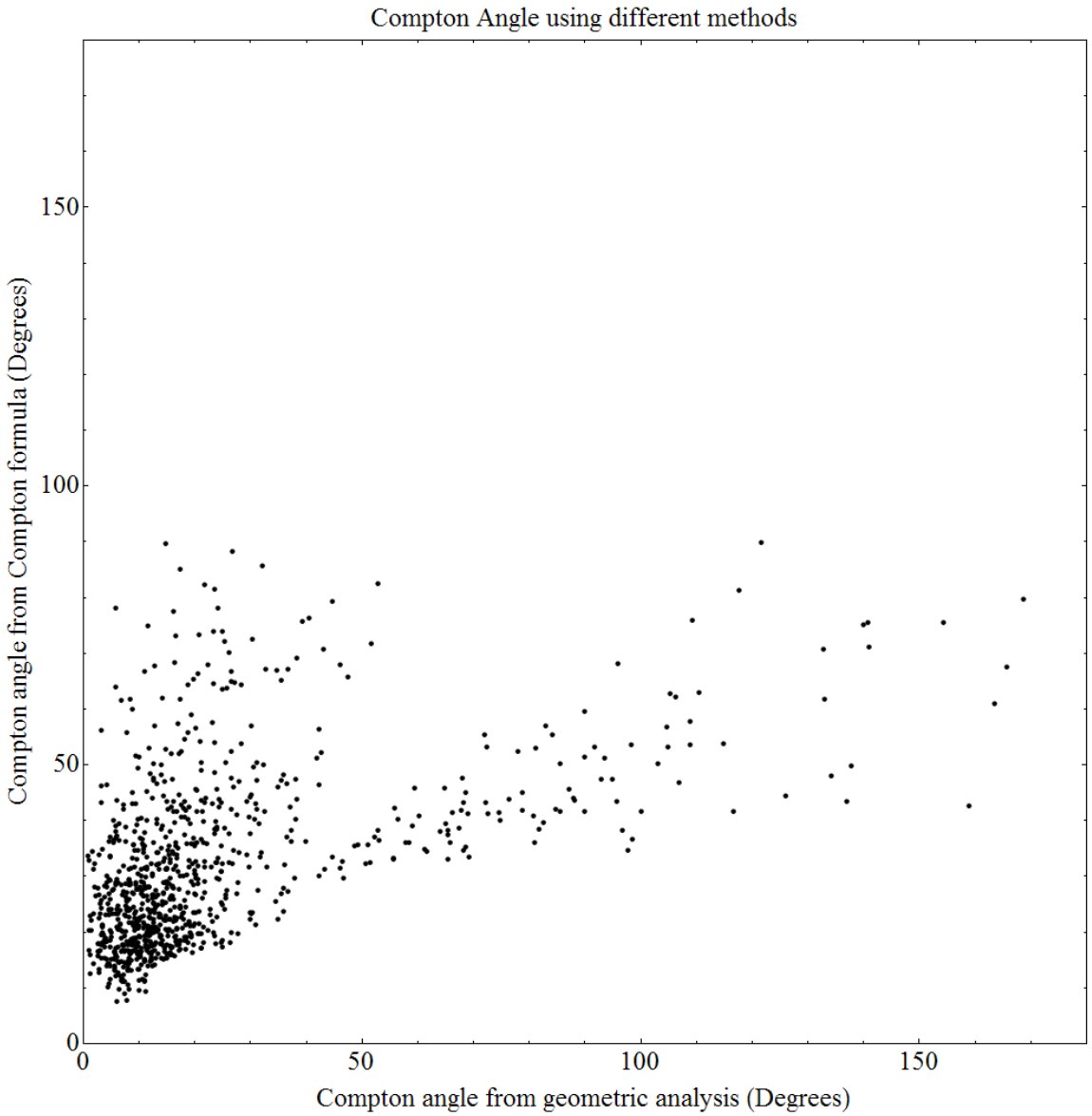

Figure 75 Scatter plot of the Compton angle determined from the known coordinates (x axis) and determined from the Compton formula (y axis). This closely resembles the flight result, Figure 64.

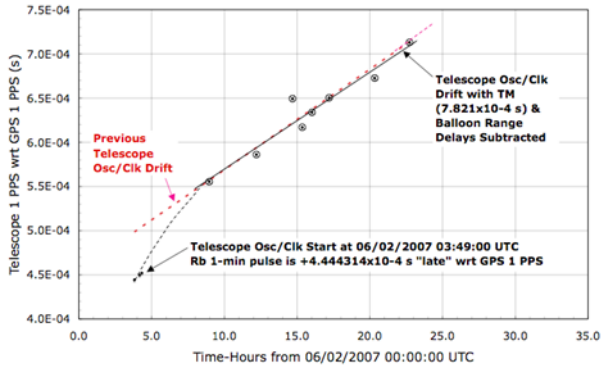

Figure 76 UTC Correction to telescope on-board clock for Crab pulsar observations.

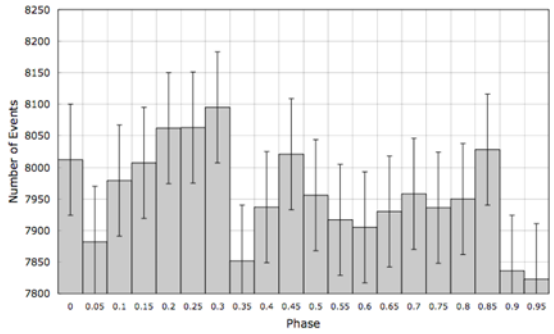

Figure 77 Preliminary Crab pulsar phase diagram for all telescope events during exposure. The error bars represent ± 1 standard deviation. The main pulsar pulse is expected at zero phase.

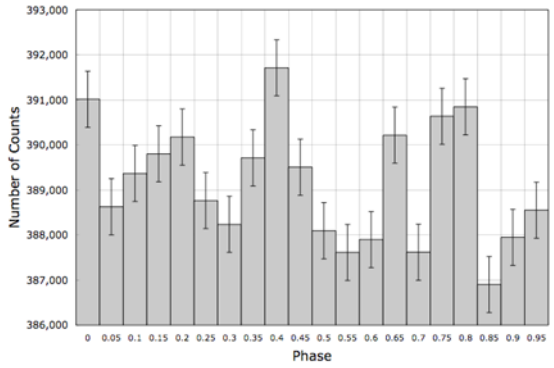

Figure 78 Preliminary Crab pulsar phase diagram for NaI scintillator events during exposure. The error bars represent ± 1 standard deviation. The absolute phase of the 1st pulse is undetermined.

Works Cited

Abdo, A. A., Ackermann, M., Atwood, W. B., Baldini, L., Ballet, J., Barbiellini, G., et al. (2008, November). The Fermi Gaama-Ray Space Telescope Discovers the Pulsar in the Young Galactic Supernova Remnant CTA1. *Science, 322*(5905), 1218-1221.

Acciari, V. A., Aliu, E., Arlen, T., Aune, T., Bautista, M., Beilicke, M., et al. (2010, May 20). The Discovery of γ-Ray Emission from the Blazar RGB J0710+591. *The Astrophysical Journal Letters, 715*(1), L49-L55.

Akyuz, A., Bhattacharya, D., Chuang, K. W., Dixon, D. D., O'Neill., T. J., Tumer, O. T., et al. (1997, August). Atmospheric gamma rays at geomagnetic latitudes of -29º and +43º. *Journal of Geophysical Research, 102*(A8), 17,359-17,364.

Akyuz, A., Bhattacharya, D., O'Neill, T. J., Samimi, J., & Zych, A. (2003). Enhanced performance of an electron tracking Compton gamma-ray telescope. *New Astronomy, 9*(2), 127-135.

Allison, J., Amako, K., Apostolakis, J., Araujo, H., Dubois, P. A., Asai, M., et al. (2006, February). Geant4 Developments and Applications. *IEEE Transactions on Nuclear Science, 53*(1), 270-278.

Aprile, E., Bolotnikov, A., Chen, D., & Mukherjee, R. (1993, March). A Monte Carlo analysis of the liquid xenon TPC as gamma-ray telescope. *Nuclear Instruments and Methods in Physics Research Section A: Accelerators, Spectrometers, Detectors and Associated Equipment, 327*(1), 216-221.

Barr, P., Bassani, L., Bazzano, A., Bianchin, V., Cadolle-Bel, M., Caballero, I., et al. (2011, March 7). ISBS Observer Manual.

Bassiani, L., Landi, R., Malizia, A., Fiocchi, M. T., Bazzano, A., Bird, A. J., et al. (2007, November 1). IGR J22517+2218=MG3 J225155+2217: A New Gamma-Ray Lighthouse in the Distant Universe. *The Astrophysics Journal, 669*(1), L1-L4.

Beckmann, V., Ricci, C., & Soldi, S. (2009). Fermi detected blazars seen by INTEGRAL. *2009 Fermi Symposium.* Washington, D.C.

Beckmann, V., Soldi, S., Ricci, C., Alfonso-Garzon, J., Courvoisier, T. J.-L., Domingo, A., et al. (2009, October 1). The second INTEGRAL AGN catelogue. *Astronomy & Astrophysics, 505*(1), 417-439.

Belanger, G., Goldwurm, A., Renaud, M., Terrier, R., Mella, F., Lund, N., et al. (2005, August). A Persistent High-Energy Flux from the Heart of the Milky Way: INTEGRAL's view of the Galactic Center. *The Astronomical Journal, 636*, 275-289.

Bhattacharya, D., O'Neill, T. J., Akyuz, A., Samimi, J., & Zych, A. D. (2004, February). Prototype TIGRE Compton γ-ray balloon-borne telescope. *New Astronomy Reviews*, 287-292.

Boggs, S. E., Amman, M. S., Jean, P., Amrose, S., Coburn, W., Lin, R. P., et al. (2003, August). Upcoming balloon flight of the nuclear Compton telescope. *Proceedings of the SPIE, 4851*, 1221-1227.

Collmar, W., Bennet, K., Bloemen, H., Blom, J. J., Hermsen, W., Lichti, G. G., et al. (1999). COMPTEL Observations of AGN at MeV-Energies. *Astrophysical Letters & Communications. 39*, pp. 57-60. Taormina/Sicily, Italy: Gordon and Breach.

Diehl, R., Halloin, H., Kretschmer, K., Lichti, G. G., Schonfelder, V., Strong, A. W., et al. (2006, January). Radioactive Al-26 from massive stars in the Galaxy. *nature, 439*, 45-47.

Diehl, R., Halloin, H., Kretschmer, K., Strong, A. W., Wang, W., Jean, P., et al. (2006, April). Al-26 in the inner Galaxy. *Astronomy & Astrophysics, 449*(3), 1025-1031.

Diehl, R., Knodlseder, J., Bennett, K., Bloemen, H., Dupraz, C., Hermsen, W., et al. (1995, May). Al-26 imaging details from COMPTEL. *Advances in Space Research, 15*(5), 123-126.

Evans, R. D. (1955). *The Atomic Nucleus.* New York: McGraw-Hill Book Company, Inc.

Fichtel, C. E., Bertsch, D. L., Chiang, J., Dingus, B. L., Esposito, J. A., Fierro, J. M., et al. (1994, October). The First Energetic Gamma-Ray Experiment Telescope (EGRET) Source Catalog. *The Astrophysical Journal Supplement Series, 94*, 551-581.

Gillessen, S., Eisenhauer, F., Trippe, S., Alexander, T., Genzel, R., Martins, F., et al. (2009, February). Monitoring Stellar Orbits Around the Massive Black Hole in the Galactic Center. *The Astrophysical Journal, 692*(2), 1075-1109.

Harding, A., & Muslimov, A. (2004, June). Pulsar Slot Gaps and Unidentified EGRET Sources. *Astrophysics and Space Science, 297*, 63-70.

Hartman, R. C., Bertsch, D. L., Bloom, S. D., Chien, A. W., Deines-Jones, P., Esposito, J. A., et al. (1999, July). The Third EGRET Catalog of High-Energy Gamma-Ray Sources. *The Astrophysical Journal Summplement Series, 123*(1), 79-202.

Herzo, D., Koga, R., Millard, W. A., Moon, S., Ryan, J., Wilson, R., et al. (1975, February). A large double scatter telescope for gamma rays and neutrons. *Nuclear Instruments and Methods, 123*(3), 583-597.

Jensen, P. L., Clausen, K., Cassi, C., Ravera, F., Janin, G., Winkler, C., et al. (2003, November). The INTEGRAL spacecraft - in-orbit performance. *Astronomy & Astrophysics, 411*(1), L7-L17.

Johnson, R. P., & Mukherjee, R. (2009, May). GeV telescopes: results and prospects for Fermi. *New Journal of Physics, 11*.

Kaluzienski, L., & Shrader, C. (1999, February). Appendix G to the NASA RESEARCH ANNOUNCEMENT for the COMPTON GAMMA RAY OBSERVATORY GUEST INVESTIGATOR PROGRAM. Washington, D.C.: National Aeronautics and Space Administration.

Kanbach, G., Andritschke, R., Bolser, P. F., Schopper, F., Schonfelder, V., & Zoglauer, A. (2003, March). Concept study for the next generation medium-energy gamma-ray astronomy mission - MEGA. *Proceedings of the SPIE, 4851*, 1209-1220.

Kramer, M., Bell, J. F., Manchester, R. N., Lyne, A. G., Camilo, F., Stairs, I. H., et al. (2003, July). The Parks Multibeam Pulsar Survey-III. Young pulsars and the discovery and timing of 200 pulsars. *Monthly Notices of the Royal Astronomical Society, 342*(4), 1299-1324.

Krivonos, R., Revnivtsev, M., Lutovinov, A., Sazonov, S., Churazov, E., & Sunyaev, R. (2007, November 4). INTEGRAL/IBIS all-sky survey in hard X-rays. *Astronomy & Astrophysics, 475*(2), 775-784.

Kroeger, R. A., Neil, J. W., Kinzer, R. L., Kurfess, J. D., Inderhees, S. E., Philips, B., et al. (1995, September). Spatial resolution and imaging of gamma rays with germanium strip detectors. *Proceedings of the SPIE, 2158*, 236-243.

Kurfess, J. D., Johnson, W. N., Kroeger, R. A., & Philips, B. F. (2000). Considerations for the next Compton telescope mission. *THE FIFTH COMPTON SYMPOSIUM. 510*, pp. 789-793. Porthmouth, New Hampshire: AIP Conference Proceedings.

Kuulkers, E., Shaw, S. E., Paizis, A., Chenevez, J., Brandt, S., Courvoisier, T. J.-L., et al. (2007, May). The INTEGRAL Galactic bulge monitoring program: the first 1.5 years. *Astronomy & Astrophysics, 466*(2), 595-618.

Longair, M. S. (1992). *High Energy Astrophysics - Volume 1 Particles, photons and their detection 2nd Edition* (Vol. 1). Cambridge, Great Briton: Cambridge University Press.

Lorimer, D. R., & Kramer, M. (2004). Pulsar timing. In D. R. Lorimer, & M. Kramer, *Handbook of Pulsar Astronomy* (pp. 200-212). Cambridge, United Kindom: Cambridge University Press.

Lyne, A. G., & Graham-Smith, F. (2006). Pulsar timing. In A. G. Lyne, & F. Graham-Smith, *Pulsar Astronomy, 3rd Edition* (pp. 50-61). Cambridge, UK: Cambridge University Press.

Lyne, A. G., Pritchard, R. S., & Smith, F. G. (1993, December). 23 years of Crab pulsar rotational history. *Monthy Notices of the Royal Astronomical Society, 265*(4), 1003-1012.

Mahoney, W. A., Ling, J. C., Wheaton, W. A., & Jacobson, A. S. (1984, November). HEAO 3 discovery of Al-26 in the interstellar medium. *The Astronomical Journal, 286*, 578-585.

McNaron-Brown, K., Johnson, W. N., Jung, G. V., Kinzer, R. L., Kurfess, J. D., Strickman, M. S., et al. (1995, October 1). OSSE Observations of Blazars. *The Astrophysical Journal, 451*, 575-584.

Nautical Almanac Office, U. S. (2005). *The Astronomical Almanac 2007.* Washington: U.S. Government Printing Office.

O'Neill, T. J., Bhattacharya, D., Blair, S., Case, G., Tumer, O. T., White, R. S., et al. (1995, August). The TIGRE Desktop Prototype Results for 511 and 900 KeV Gamma Rays. *IEEE Transactions on Nuclear Science, 42*(4), 933-939.

O'Neill, T. J., Bhattacharya, D., Posen, M., Zych, A. D., Samimi, J., & Akyuz, A. (2003, April). Developement of the TIGRE Compton Telescope for Intermediate-Energy Gamma-Ray Astronomy. *IEEE Transactions on Nuclear Science, 50*(2), 251-257.

Pacheco, L. E. (n.d.). *Scientific Balloon Flight Facility - Fort Sumner, New Mexico*. Retrieved May 5, 2010, from StratoCat: http://stratocat.com.ar/bases/26e.htm

Peterson, L. E., Schwartz, D. A., & Ling, J. C. (1973, December). Spectrum of Atmospheric Gama Rays to 10 MeV at λ=40º. *Journal of Geophysical REsearch, 78*(34), 7942-7958.

Purcell, W. R., Cheng, L. -X., Dixon, D. D., Kinzer, R. L., Kurfess, J. D., Leventhal, M., et al. (1997, December 20). OSSE Mapping of Galactic 511 keV Positron Annihilation Line Emission. *The Astrophysical Journal, 491*, 725-748.

Rester, A. C., Coldwell, R. L., Dunnam, F. E., Eichhorn, G., Trombka, J. I., Starr, R., et al. (1989, July 15). Gamma-ray Observations of SN 1987A from Antarctica. *The Astrophysical Journal, 342*, L71-L73.

Revnivtsev, M. G., Churazov, E. M., Sazonov, S. Y., Sunyaev, R. A., Lutovinov, A. A., Gilfanov, M. R., et al. (2004, October). Hard X-ray view of the past activity of Sgr A* in a natural Compton mirror. *Astronomy & Astrophysics, 425*(3), L49-L52.

Sanchez-Fernandez, C., Roques, J. P., & Diehl, R. (2011, March 7). SPI Observer Manual.

Schonfelder, V., Diehl, R., Lichti, G. G., Steinle, H., Swanenburg, B. N., Deerenburg, A. J., et al. (1984, February). The imaging Compton telescope Comptel on the gamma ray observatory. *IEEE Transactions on Nuclear Science, 31*(1), 766-770.

Schonfelder, V., Hirner, A., & Schneider, K. (1973). A Telescope for Soft Gamma Ray Astronomy. *Nuclear Instruments and Methods, 107*(2), 385-394.

Tumer, O. T., Akyuz, A., Bhattacharya, D., Blair, S. C., Case, G. L., Dixon, D. D., et al. (1995, August). The TIGRE Instrument for 0.3-100 MeV Gamma-Ray Astronomy. *IEEE Transactions on Nuclear Science, 42*(4), 907-916.

van der Meulen, R. D., Bloemen, H., Bennett, K., Hermsen, W., Kuiper, L., Much, R. P., et al. (1998, February). COMPTEL γ-ray study of the Crab Nebula. *Astronomy & Astrophysics, 330*(1), 321-326.

Wang, W., Lang, M. G., Diehl, R., Halloin, H., Jean, P., Knodlseder, J., et al. (2009, March). Spectral and intensity variations of Galactic Al-26 emission. *Astronomy & Astrophysics, 496*(IV), 713 - 724.

Weidenspointner, G., Skinner, G., Jean, P., Knodlseder, J., von Ballmoos, P., Giovanni, B., et al. (2008, January). An asymmetric distribution of positrons in the Galactic disk revealed by γ-rays. *nature, 451*, 159-162.

Zoglauer, A. C. (2006, January). First Light for the Next Generation of Compton and Pair Telescopes. *First Light for the Next Generation of Compton and Pair Telescopes - Development of New TEchniques for the Data Analysis of Combined Compton and Pair Telescopes and their Application to the MEGA Prototype*. Garching, Germany.

Zych, A. D., Dayton, B., Tumer, O. T., & White, R. S. (1983). High Sensitivity High Resolution Double Scatter 1-30 MeV Gamma Ray Telescope. *International Cosmic Ray Conference* (pp. 343-346). Bangalore, India: Bombay, Tata Institute of Fundemental Research.